Ph.D. DISSERTATION

CERENKOV-LIKE RADIATION IN METALLIC METAMATERIAL

금속 메타물질에서의 체렌코프 유사 방사

BY
ANIRBAN BERA

AUGUST 2014

DEPARTMENT OF ELECTRICAL ENGINEERING AND COMPUTER SCIENCE

SEOUL NATIONAL UNIVERSITY

CERENKOV-LIKE RADIATION IN METALLIC METAMATERIAL

Supervised by

Professor Gun-Sik Park

Submitting a doctoral thesis of Electrical Engineering

August 2014

Department of Electrical Engineering and Computer Science

Seoul National University

Anirban Bera

Confirming the doctoral thesis written by

Anirban Bera

August 2014

Chair Nam, Sangwook (Seal)

Vice Chair Park, Gun-Sik (Seal)

Examiner Park, Namkyoo (Seal)

Examiner Kim, Yong Hyup (Seal)

Examiner Jeong, Young-Uk (Seal)

공학박사 학위논문

CERENKOV-LIKE RADIATION IN METALLIC METAMATERIAL

금속 메타물질에서의 체렌코프 유사 방사

2014 년 8 월

서울대학교 대학원

전기·컴퓨터 공학부

베라 아닐반

Abstract

Cerenkov radiation is extensively used in particle detectors, particle counters, particle accelerator, and generation of electromagnetic radiation at frequencies up to terahertz (THz) range. A dielectric is widely used as a supporting medium to obtain Cerenkov radiation from a beam of convection electrons (moving electron bunch). However, selection of a suitable material for this purpose is limited due to its thermal issues, electron beam energy threshold, and dielectric breakdown at high RF fields. A metallic metamaterial, a periodic cut-through slit perforated on a metal film, shows a positive dielectric response, which could be a promising alternative to dielectrics for generation of Cerenkov radiation.

The work in this thesis is motivated to analyze the response of the metallic metamaterial when it is in close proximity of a moving electron bunch. Theoretical study, carried out here, reveals that Cerenkov-like radiation is generated inside the metamaterial if a convection electron bunch is present near to its surface. It has also been found that the characteristics of the radiation, corresponding to the parameters such as the radiation angle and the electron energy threshold, inside a metallic metamaterial, are similar to those of an anisotropic dielectric. However, the finite thickness of the metamaterial slab enforces the generated Cerenkov-like radiation to be resonantly excited in the structure at the frequencies where the guided-mode and the beam-mode phase velocities are synchronous. The edge coupling of radiation, as in an ordinary dielectric, is not applicable to metallic metamaterial due to “almost” zero group velocity of radiation in axial direction.

A study on “metallic metamaterial slab-symmetric wakefield accelerator” has also been done and it has been observed that the amplitude of the longitudinal wake potential is higher than that of a dielectric slab-symmetric structure. Also, it has been observed that the transverse wake potential is lower in case of the metamaterial slab-symmetric structure than that of the dielectric slab-symmetric structure. Moreover, due to all-metal structure, the metallic metamaterial structure has several advantages over the dielectric as the former has better heat dissipation capability and lower probability to static charge accumulation on the surface. Hence, the proposed metamaterial slab-symmetric structure is a better choice than dielectric slab-symmetric structure for wakefield accelerator applications.

Furthermore, in order to out coupling of the Cerenkov-like radiation generated in such a metamaterial slab via the so-called “Brillouin-Zone folding”, a method that would result in the surface coupling of radiation in contrast to the ordinary edge coupling has been proposed. In the proposed method, an additional periodicity is introduced which resulted into some of the guided modes supported by the metamaterial slab to become folded, when viewed in the structure dispersion diagram. It was also found theoretically that the intensity of the surface-coupled radiation by this mechanism exhibits an order of a magnitude enhancement compared to that of an ordinary Smith-Purcell radiation.

Keywords: (6단어이내): Cerenkov-like radiation, metallic metamaterial, Brillouin-zone folding, Wakefield accelerator.

Student ID: 2009-31256

Contents

Abstract.....**I**

List of figures.....**V**

List of Tables.....**XI**

List of symbols.....**XII**

Chapter 1: Introduction.....**1**

1.1 Cerenkov Radiation.....2

1.2 Issues in Cerenkov Radiation.....5

1.3 Motivation and Goal.....7

1.4 Organization of the Thesis.....8

Chapter 2: Metamaterial: A Brief Review.....**10**

2.1 Introduction.....11

2.2 Electric and Magnetic Responses of Metamaterial.....13

2.2.1 Electric Response.....13

2.2.2 Magnetic Response.....14

2.3 Negative Refractive Index Material.....15

2.4 Positive Refractive Index Material.....18

2.5 Selection of Metamaterial For Interaction With Electron Beam.....19

Chapter 3: Metallic Metamaterial.....**22**

3.1 Introduction.....23

3.2 Dispersion Relation.....24

3.3 Graphical Mode Solution of Dispersion Relation.....28

3.4 Numerical Simulation of Dispersion Relation.....30

3.5 Dispersion Relation of Metallic Metamaterial With Finite Transverse Width.....32

3.6 Numerical Simulation of Dispersion Relation of Metallic Metamaterial With Finite Transverse Width.....35

3.7 Anisotropic Dielectric Behavior of Metallic Metamaterial ……..…….....36

3.8 Effect of Introduction of Side-Wall Boundaries in Metallic Metamaterial……...…...41

Chapter 4: Cerenkov-like Radiation in Metallic Metamaterial……...**47**

4.1 Introduction……48

4.2 Response of Metallic Metamaterial to Convection Electron.....49

4.3 Potential Use of Metamaterial in a Wakefield Accelarator……..……...58

4.3.1 Introduction…….....58

4.3.2 Metallic Metamaterial Wakefield Accelerator.....59

Chapter 5: Out-Coupling of Cerenkov-like Radiation via Brillouin-Zone folding …...**64**

5.1 Introduction……65

5.2 Brillouin-Zone Folding Mechanism……..…….....66

5.3 Brillouin-Zone Folding of Metallic Metamaterial……..…68

5.4 Out-coupling of Cerenkov-like Radiation via Brillouin-Zone Folding……....…72

5.5 Metallic Metamaterial as an Interaction Structure of a High-Frequency Electromagnetic Wave Generator……..…..……...…..……...…..…....80

Chapter 6 Conclusion and Future Work……..……**84**

6.1 Introduction……..……..…...85

6.2 Summary of the Thesis……..…….....…….....85

6.3 Scope for Future Work……...……....…..…87

Bibliography……...…….…….....**88**

List of Publications……..……...….**98**

Korean Abstract……...……...…**101**

Acknowledgment……...……...…**103**

List of Figures

Figure 1.1.1: Schematic diagram of Cerenkov radiation: particle moving with velocity βc and radiated wave-front moving with velocity c/n inside the medium at an angle θ with respect to the particle.....2

Figure 1.1.2: Cerenkov radiation in, (a) right handed material (emitting particle and energy of emitted radiation move in same direction), (b) left-handed medium (emitting particle and emitted radiation move in opposite direction)……..5

Figure 1.2.1: Cross-sectional view of beam-driven cylindrical dielectric-lined waveguide (color map illustrates longitudinal wakefield)…….…….6

Figure 2.1.1: Classification of materials based on their dielectric and magnetic properties. The wavy lines represent propagating waves, and the axes set in quadrants 1 and 3 show the right and left-handed nature of *E, H* and *k* vectors. The waves in quadrants 2 and 4 decay evanescently inside the materials, which is depicted schematically. *S* is the Poynting vector…….12

Figure 2.2.1: Schematic view of periodic wires (with radius *r*) arranged in a simple cubic lattice (with lattice constant *d*)……14

Figure 2.2.2: Schematic view of split ring resonators, with outer radius *r* and *s* is the separation between the two rings. A magnetic field penetrating the resonator induces a current ($\vec{j}$) and a magnetic moment ($\vec{m}$)…….……..15

Figure 2.3.1: Negative index metamaterial formed by three-dimensional array of SRRs and wires……....16

Figure 2.3.2: Schematic view of fishnet structure of negative index material in the visible region (yellow light) consisting of a dielectric layer (green color) between two metal layers (gray color)……..……16

Figure 2.3.3: Pendry model of perfect lens, made from negative index flat slab material focusing all the light rays from a point source and amplifying to evanescent waves…….….18

Figure 2.4.1: Unit cell structure of the high-index metamaterial where a thin 'I'-shaped metallic patch is symmetrically embedded in a dielectric material (*E, H* and *k* denote the electric field, magnetic field and propagation direction of the incident terahertz wave)…….…….19

Figure 2.5.1: SRR (dark gray ring) and rod (dark strip) structure with electric field (arrows) parallel to the surface, on a dielectric slab (gray structure)……..20

Figure 2.5.2: Complementary SRR (gray region) and its electric field pattern (arrows, perpendicular to the surface) on dielectric slab (white region)…….…...21

Figure 2.5.3: Simulated model of electric field pattern (arrows) of Metallic metamaterial (gray structure)……..……21

Figure 3.1.1: Schematic of the metal film (black regions) and vacuum part (white regions), (A) with periodic slits (*d*, *a*, *L* are the periodicity, width of the slit and thickness of the metal film, respectively) and. (B) its equivalent effective dielectric slab model……..…….…….24

Figure 3.2.1: Schematic of different regions of metal slit, without any external source, extended in the *x*-*y* plane (with period much less than the incident wavelength) are: (i) above the metal film, (ii) inside slit and (iii) below of the metal film…….…….….25

Figure 3.3.1: Graphical mode solution of equations (3.3.1) and (3.3.2), taking k_x as the parameter……..……..29

Figure 3.3.2: Dispersion relation (analytical solution) of first three guided modes supported by metal slit for $n = d/a = 4$……..29

Figure 3.4.1: Simulated FDTD model of a single period structure with periodic boundary conditions applied on left and right boundaries…….…..30

Figure 3.4.2: Electric field contour (E_x) inside slit for, (a) first guided mode, (b) second guided mode and (c) third guided mode…….…….….31

Figure 3.4.3: Dispersion characteristics of first three guided modes of metal slit with period *d* and slit width *a*..…….…..31

Figure 3.5.1: Three-dimensional model of a metallic metamaterial structure (origin of coordinate system is considered at center of one slit and *I*, *II* and *III* refers to regions above the structure, inside the slit and below the structure, respectively)……..……..32

Figure 3.6.1: Schematic view of unit cell of metamaterial structure (planes bounded by dotted lines are the boundaries of the solution volume, and planes are perfect absorbing boundaries except two periodic boundaries along *y*-*z* plane).…..35

Figure 3.6.2: Effect of structure transverse width on dispersion characteristics for first eigen mode (overlapping of curves represents that dispersion is independent of transverse width of the structure)…….……..…..36

Figure 3.7.1: Variation of return loss with normalized frequency (d/λ) for polarization of the metal slit (red lines), effective anisotropic (green line) and isotropic (black dashed line) dielectric slab, keeping period and width of slit constant (Table-3.7.1)……..……..39

Figure 3.7.2: Variation of return loss with normalized frequency (d/λ) for polarization-2, of the metal slit (red lines), effective anisotropic (green line) and isotropic (dotted line) dielectric, for fixed *d* and *a*……..39

Figure 3.8.1: Three-dimensional model of a metallic metamaterial structure with side wall……..42

Figure 3.8.2: Schematic view of unit cell of metamaterial structure with side wall...…..43

Figure 3.8.3: Eigen frequency vs transverse width of structure with side wall (dotted line) and without side wall (solid line)……..…….…..43

Figure 3.8.4: Variation of electric field (E_x) without side wall of metal slit, (a) along *y*, (b) along *x*, and (c) along *z*, of the structure and shaded regions indicate the regions inside the slit……..…….….44

Figure 3.8.5: Variation of electric field (E_x) with side wall of metal slit, (a) along *y* (b) along *x* and (c) along *z*, shaded regions indicate the regions inside the slit……...…….45

Figure 3.8.6 Comparison between simulated (solid line) and analytical (broken line) eigen modes with frequency, taking transverse widthas the parameter (solid line for simulated result and broken line for analytical result)…….…….....46

Figure 4.1.1: Schematic view of cut-through metal slits (metallic metamaterial) with convection electron bunch…….……..48

Figure 4.2.1: Model to study the interaction between metallic metamaterial and electron. (The planes, bounded by dotted lines represent the perfect absorbing boundaries of solution volume and, are far from structure surface)…….....50

Figure 4.2.2: Contour plot of E_x taken on *z*-*x* plane at $y = 0$, corresponding to velocity $0.5c$, and the radiation angle obtained is 26.56° (The red color indicates the radiated wave-front inside structure…….…….…..50

Figure 4.2.3: Comparison between radiation angles and effective dielectric media taking beam energy as the parameter (The threshold energy for Cerenkov radiation in an isotropic dielectric with refractive index 4 is 16.8keV and no energy threshold for metallic metamaterial and anisotropic dielectric)……..…..52

Figure 4.2.4: Contour plot of E_x corresponding to electron bunch energy 80keV in, (a) isotropic dielectric (refractive index 4), (b) metamaterial structure(d/a = 4) and (c) anisotropic dielectric(refractive index 4), along x (black arrows on each figure denote the moving bunch locations and all three structures radiations are observed by the electron bunch itself)…….…….…..53

Figure 4.2.5: Contour plot of E_x (for electron bunch energy 10keV) in, (a) isotropic dielectric (refractive index 4), (b) metamaterial structure (d/a = 4), and (c) anisotropic dielectric (refractive index 4), along x direction and very high in other directions……54

Figure 4.2.6: Guided-mode dispersion characteristics of metallic metamaterial with a typical beam-mode dispersion line $\beta(= v/c) = 0.5$, the shaded and white regions indicating the non-radiating and radiating regimes respectively…56

Figure 4.2.7: Inside-slit and far-field (magnified 25 times) FFT spectrum of the E_x field of metallic metamaterial with normalized frequency…….…..56

Figure 4.2.8: Effect of slab thickness on excited mode frequency keeping other parameters constant……...……57

Figure 4.3.1: Schemetic of slab-symmetric dielectric waveguide and electron bunch passes through along the axis (black parts are the metallic coating on dielectric slab)…….60

Figure 4.3.2: Schemetic of slab-symmetric metallic metamaterial waveguide and electron bunch when electron bunch passes through the axis of structure…….60

Figure 4.3.3: Contour of axial wake field (E_x), on x-z plane, induced by electron bunch in (a) dielectric slab-symetric and (b) metallic metamaterial slab-symmetric waveguide…….61

Figure 4.3.4: Comparison of (a) longitudanal, (b) transverse (along 'y') wake potentials and (c) transverse (along 'z') wake potentials, for dielectric slab-symmetric and metamaterial slab-symmetic structures……63

Figure 5.2.1: Schematic view of one-dimensional lattice with lattice basis vector $\vec{m}$….66

Figure 5.2.2: Schematic view of reciprocal lattice and first Brillouin-zone of a one-dimensional lattice with lattice vector $\vec{m}$. ($\vec{A}$ is the basis vector of reciprocal lattice)……..……...….67

Figure 5.2.3: Schematic view of one-dimensional super-lattice……...……68

Figure 5.3.1: (a) Two-dimensional view (on *z-x* plane) of the metamaterial structure (structure-I), (b) equivalent one-dimensional lattice, and (c) corresponding reciprocal lattice……..69

Figure 5.3.2: Dispersion diagram modes supported by the structure-I. Dashed lines indicate the dispersion and solid line indicates the vacuum light line…..…69

Figure 5.3.3: (a) array of cut through slit with periodicity *D* (*=4d*) (structure-II), perforated on a perfect metal, (b) equivalent one-dimensional lattice, (c) corresponding reciprocal lattice and first Brillouin-zone…….70

Figure 5.3.4: Detail of superlattice based structure (a) structure-I, (b) structure-II and (c) superlattice formed by superimposing structure-II on structure-I……...….71

Figure 5.3.5: (a) First Brillouin-zone of structure-I, (b) first Brillouin-zone of structure-II, (c) two overlapping Brillouin-zones of superlattice…….…71

Figure 5.3.6: Dispersion diagram of modes supported by structure-I (dashed lines), folded mode (due to introduction of additional periodicity) (solid thick lines), vacuum light line (dotted line) and zone folding symmetry (vertical solid line)……...……..72

Figure 5.4.1: (a) Metallic metamaterial structure consisting of a one-dimensional array of periodic cut-through slits perforated on a metallic slab (structure-A) and, (b) the proposed metamaterial structure obtained by periodically modifying the thickness of structure-A so as to provide additional periodicity (structure-B) in proximity to a moving electron bunch…….…73

Figure 5.4.2: Guided-mode dispersion characteristics of structure-A, along with a typical beam-mode dispersion line ($\beta = 0.5$), the shaded and non-shaded regions indicating the non-radiating and radiating regimes, respectively. The first four lower dispersion intersecting points are represented by 1, 2, 3 and 4, respectively…….75

Figure 5.4.3: Guided mode dispersion and folded bands. The folded bands are shown in solid lines, with the vertical dotted line indicating zone-folding symmetry and with the points indicated by the arrows on the folded dispersion curve representing the points at which the momentums corresponding to points 2, 3 and 4, respectively, are shifted due to band folding…….…..75

Figure5.4.4: Inside-slit and far-field (magnified 25 times) FFT spectrum of the E_x of structure-B……...76

Figure 5.4.5: E_x field pattern at the typical angular frequency ($\omega = 2\pi c/d$) of 0.12 for structure-B showing fields radiated from the top and bottom surfaces…….76

Figure 5.4.6: Metamaterial structure with additional period (a) *D* = 3*d* and (b) *D*= 2*d*..78

Figure 5.4.7: Guided mode dispersion and folded bands for structure with additional period $D = 3d$. The folded bands are shown in solid lines, with the vertical dotted line indicating zone-folding symmetry and with the points indicated by the arrows on the folded dispersion curve representing the points at which the momentums corresponding to points 2, 3 and 4, respectively, are shifted due to band-folding……..78

Figure 5.4.8(a): Guided mode dispersion and folded bands for structure with additional period $D = 2d$. The folded bands are shown in solid lines, with the vertical dotted line indicating zone-folding symmetry and with the points indicated by the arrows on the folded dispersion curve representing the point at which the momentums corresponding to point 4, is shifted due to band-folding…79

Figure 5.4.8(b): Inside-slit and far-field (magnified 25 times) FFT spectrum of the E_x field of metamaterial structure with additional period $D = 2d$. No discernible peaks in far-field spectrum indicate that there is no out-coupling from structure…..……..…79

Figure 5.5.1: (a)Schematic of reflection metal grating along with moving electron bunch and (b) the variation of the radiation intensity of the reflection metal grating with the grating groove depth at an angular frequency $(\omega = 2\pi c/d)$ of 0.12……..……82

Figure 5.5.2: Angular dependence of the far-field radiation of structure-B compared to that of the reflection grating (magnified 5 times) at an angular frequency $(\omega = 2\pi c/d)$ of 0.12, the measurement angle being the angle between the direction of the moving electron bunch and that of the radiation……..……83

List of Tables

Table 3.7.1: Three different structures with their respective material properties and direction of electric field (blue arrows) of incident waves. The sketch of structures are not in scale, however the dimensions of all structure are identical in all the three directions……..…….……38

Table 3.7.2: Electric field (E_x) contour at inside the dielectric slab (bounded by thin black line) and metal slit and outside the structure. Normal incidence and two types of polarizations are considered. The origin of the coordinate system is at the center of corresponding structures and electric field contours are shown on x-z plane (y=0)…….40

List of Symbols

c : Light velocity in free space.

n : Refractive index of medium.

θ : Cerenkov angle.

β : Velocity ratio(c/v).

d : Period of slit.

a : Width of slit.

L: Thickness of metal film.

w : Transverse width of metallic metamaterial structure excluding the side-wall.

λ : Wave length.

ω : Angular frequency.

H_y : 'y' component of magnetic field.

E_x : 'x' component of electric field.

r_p : Reflection coefficient.

α_p : Wave momentum along 'z'.

p : Diffraction order

G_p : Quasi parallel momentum along the metal surface (along 'x').

k_y : Wave number along 'y' inside slit.

t_p : Transmission coefficient.

f : Metal filling factor of metallic metamaterial.

ε : Isotropic electric permittivity.

ε_x : Permittivity in 'x'.

ε_y : Permittivity in 'y'.

ε_z : Permittivity in 'z'.

ε_o : Permittivity of an uni-axial crystal along ordinary axis.

ε_e : Permittivity of an uni-axial crystal along extraordinary axis.

μ : Isotropic magnetic permeability.

μ_x : Permeability in 'x'.

μ_y : Permeability in 'y'.

μ_z : Permeability in 'z'.

A_m and B_m are constants.

ω_p: Plasma frequency.

ω_o: Resonant frequency.

γ : Damping factor related to material losses.

n_e: Density of bound electrons.

m_e: Mass of the electron.

e: Charge of electron.

CHAPTER 1

Introduction

1.1 Cerenkov Radiation

1.2 Issues in Cerenkov Radiation

1.3 Motivation and Goal

1.4 Organization of the Thesis

1.1 Cerenkov Radiation

Cerenkov radiation [1], is an electromagnetic radiation, emitted when a charged particle, namely, an electron, passes through a dielectric medium at higher velocity than the phase velocity of light in that medium. Such a radiation possesses a unique angular and frequency spectrum [2]. The molecule of the medium is polarized by the moving charge particle and turn back quickly to their ground state, emitting radiation in the process. In free space, electron cannot travel faster than *c*, the speed of light in free space. However, light (which is an electromagnetic wave) can also propagate through both anisotropic and isotropic medium with a reduced velocity equal to *c/n*; where *n* is the refractive index of that medium. When a charged particle moves through a medium at a velocity higher than the velocity of light in that medium, a pour of photons is triggered inside the medium. These photons are in phase with each other and interfere constructively to form a coherent electromagnetic radiation, termed as Cerenkov radiation. The energy of this radiated electromagnetic wave (Cerenkov radiation) propagates only in the forward direction, forming a forward-pointing conical wave-front. The mechanism of Cerenkov radiation is shown in the figure 1.1.1.

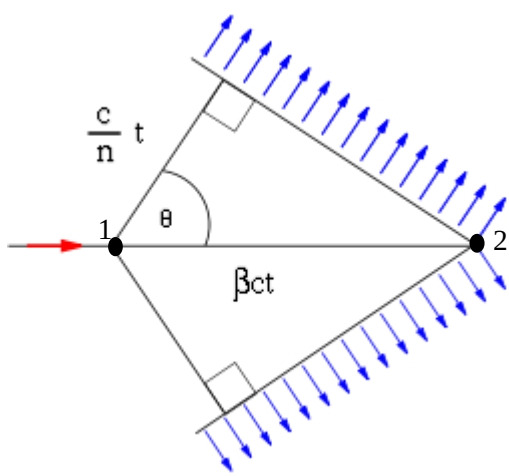

Figure 1.1.1: Schematic diagram of Cerenkov radiation: particle moving with velocity βc and radiated wave-front moving with velocity c/n inside the medium at an angle θ with respect to the particle. (Courtesy: Wikipedia)

In this figure (figure 1.1.1), the red arrow represents movement of the particle with velocity v_p such that $\frac{c}{n} < v_p < c$, where c is speed of light in vacuum, and n is the refractive index of the medium. The initial location of the superluminal particle at some initial moment (t=0) is represented by '1' and '2' represents the location of particle at some later time t. The distance travelled by the particle in time t can be given as:

$$x_p = v_p t = \beta c t \tag{1.1.1}$$

whereas the emitted electromagnetic waves are constricted to travel the distance as:

$$x_{em} = v_{em} t = \frac{c}{n} t \tag{1.1.2}$$

From (1.1.1) and (1.1.2), one can get the angle between wave-front and particle as:

$$cos\theta = \frac{1}{n\beta} \tag{1.1.3}$$

with $\beta = v_p/c$, the ratio between the velocity of the particle and the velocity of light. The emitted wave-fronts (blue arrows) travel at speed of $v_{em} = c/n$. Cerenkov radiation remain qualitatively unchanged even in the dispersive material [3-5], however, in simultaneously negative permittivity and permeability, commonly known as a negative-index material, the Cerenkov radiation travels in the opposite direction to the particle velocity [6-11]. Another possibility of Cerenkov radiation exists near a periodic structure, where simple Bragg scattering of light can give rise to radiation without any velocity threshold. This was first confirmed by Smith and Purcell [12] in early experiments with electrons traveling near the surface of a metallic grating and further this effect has been extended to near the surface of dielectric structures [13-14]. Cerenkov radiation has since been studied in one-dimensionally periodic multilayer stacks [15-16], and photonic crystal [17]. Cerenkov radiation is also used to map photonic band structure of 2D photonic crystals [18-19].

Cerenkov radiation is extensively used in particle detectors and counters. In addition to that Cerenkov radiation is also used to generate electromagnetic radiation at frequencies up to THz range [20]. Hollow dielectric tube coated on the outer surface with metal has been explored for converting electron beam energy into radiation since late 1940s [21]. There are several

theoretical and experimental works on particle accelerator (dielectric wakefield accelerator) [22-25] for particle acceleration and on Cerenkov free-electron laser (CFEL) [26] for generation of electromagnetic radiation at microwave or THz frequency region [27-28]. In 1988, Garate *et al.* operated first CFEL at far-infrared wavelengths (375−1000μm) and produced 10−200kW pulses in a self-amplified configuration [29]. Recently, A.M. Cook *et al.* [20] demonstrated that when a sufficiently short (rms bunch length σ less than a radiation wavelength λ) driving beam containing N electrons passes inside a hollow cylindrical dielectric tube coated on the outer surface with metal (dielectric-lined waveguide), tens of megawatts of peak power at frequencies well above 1THz is generated due to coherent Cerenkov radiation (CCR) [28], [30-32].

Victor Veselago [33] first time examined the feasibility of medium with simultaneously negative permeability and negative permittivity and he concluded that inside such media the electric field intensity *E*, magnetic field intensity *H* and the wave vector *k*, form a left handed triplet [33]. Left handed properties of such materials result in a reverse Doppler shift and Cerenkov radiation. One phenomena of interest is, unlike the traditional, positive refractive index materials, in left-handed metamaterials (LHMs) with simultaneously negative permittivity and permeability, reversed Cerenkov radiation allowing the back-ward emitted wave [34] (figure 1.1.2) easily separable from the emitting particles and is useful for particle identification and counting. Many researchers have referred to Vesalago's statement about the reversal of Cerenkov radiation both theoretically and experimentally. Yu. O. Averkov and V. M. Yakovenko [6] derived the mathematical solution for Cerenkov radiation in left-handed media in order to demonstrate existence of backward radiation. The first experimental demonstration of the reverse Cerenkov radiation using a beam of charged particles with metamaterials was carried out in a waveguide by S. Antipov et al. [35]. In this experiment they have observed the transmission peak in the left-handed band which is an indirect observation of the wakefield generation. Later backward Cerenkov radiation was observed in the left-handed band with the slotted waveguide surrounded with the LHMs [11]. In this experiment [11], they have used a dipole array (slotted waveguide) which has proven equivalence with the moving charged particle.

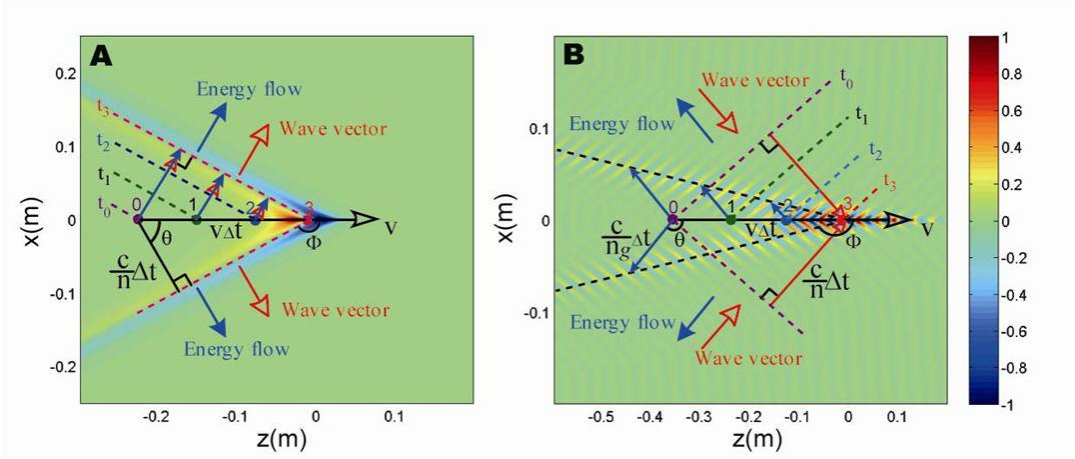

Figure 1.1.2: Cerenkov radiation in, (a) right handed material (emitting particle and energy of emitted radiation move in same direction), (b) left-handed medium (emitting particle and emitted radiation move in opposite direction) [34]

1.2 Issues in Cerenkov Radiation

Modern electron accelerators are used to generate radiation in the THz spectral region, typically, 100GHz to 3THz [36]. Dielectric-lined waveguide structures [20] (hollow dielectric tube coated on outer surface by metal) (figure 1.2.1) are widely used to generate electromagnetic radiation from a relativistic electron beam. The CCR wakefields [28],[30-32],[37-39] is generated when a relativistic electron bunch travels along the vacuum channel in the tube. The generated radiations are confined to a discrete set of modes arise due to waveguide boundaries [40]. However, as the frequency increases, dimension of the tube decreases and therefore it is very difficult to achieve practically (hollow tube) at THz frequencies.

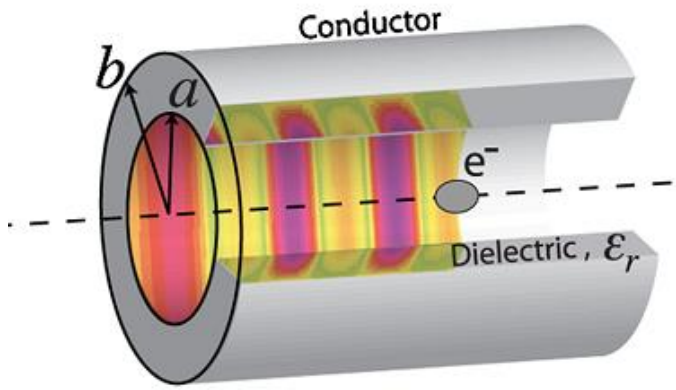

Figure 1.2.1: Cross-sectional view of beam-driven cylindrical dielectric-lined waveguide (color map illustrates longitudinal wakefield) [20].

In case of Cerenkov radiation, dielectric is used as a supporting medium and the radiation properties such as radiation angle and threshold energy of convection electron are determined by the dielectric properties. Therefore, selection of supporting medium is very much important for particular application. However, the choice of the appropriate supporting material for Cerenkov radiation is limited due to thermal issues [41], electron beam energy threshold [2] and dielectric breakdown at high RF field [41]. In addition to these, in the case of Wake field accelerators, electron bunch induced static field on dielectric diminishes the brightness of the accelerating bunches. As the frequency increases, supporting structure dimension decreases and therefore, large charge may not be accelerated as the structure does not store a large amount of energy per unit length. The transverse wakefield, which diminishes bunch brightness in cylindrical dielectric waveguide will be reduced in case of slab-symmetric wakefield accelerator [40-43] which needs very wide transverse dimension of the slab [42].

All negative index (Left-handed) metamaterials, in general are formed by the metals and dielectrics. So, their usages as supporting material for Cerenkov radiation are also limited due to dielectric breakdown strength at high-voltage and thermal issues [7]. Therefore, to overcome the above mentioned limitations, an alternative fashion is needed to tune the dielectric properties of the supporting materials. As metals are more robust against the dielectric breakdown and the thermal issues, they would be preferable over dielectric for this purpose.

1.3 Motivation and Goal

In addition to simultaneously negative permeability and negative permittivity metamaterials, there is another class of metamaterials which has both positive permeability and permittivity. A metal film with a periodic arrangement of cut-through slits exhibits dielectric properties when the wavelength of incident electromagnetic wave is much greater than the period of the slit [44-46]. The effective refractive index of this type of metamaterial is frequency independent, positive, entirely controlled by the geometry of the metal films, and can be made arbitrarily large [46]. Because of all metal structure, this kind of structure is free from dielectric breakdown at higher voltages and due to higher thermal conductivity, this structure is capable of dissipating heat efficiently. Thus, due to these advantages, the metallic metamaterial structure could be a promising alternative to dielectric as a supporting medium for Cerenkov radiation. However, it needs to study the response of this metallic metamaterial to convection electron.

Next, in case of wakefield accelerator, slab-symmetric dielectric structure provides better bunch brightness than cylindrical hollow dielectric structure. However, the slab-symmetric structure has several disadvantages, namely, low RF breakdown, poor thermal management and accumulation of static charge on dielectric surface, etc. Therefore, the potential of use of metallic metamaterial structure in wakefield accelerator needs to be thoroughly investigated.

Furthermore, the finite thickness of the metallic metamaterial slab enforces the generated Cerenkov-like radiation such that it is resonantly excited in the structure at frequencies where the guided mode and the beam mode phase velocities are synchronous. While the Cerenkov radiation generated in ordinary dielectric slabs is usually coupled out from the edges of the structure [11-12], and this types of edge coupling may not be applicable to the metallic metamaterial. Therefore, to use this structure as an interaction structure of an electromagnetic radiation source, an efficient mechanism of out-coupling of the Cerenkov-like radiation is supposed to be established.

The aim of this dissertation is to study the response of the metallic metamaterial when it is in close proximity to convection electron. Next, study the possibility of use of this metallic metamaterial as a supporting structure of a wakefield accelerators. Also, to find out the

difficulties in coupling out the radiation from structure and to develop suitable methods for coupling out the Cerenkov-like radiation from this structure.

1.4 Organization of Thesis

The dissertation is divided into 6 chapters. Overview of the Cerenkov radiation and related issues, objective and motivation behind this dissertation is presented in Chapter 1. Chapter 2 briefs overview of the metamaterial including origin of negative electrical permittivity, negative magnetic permeability and description of simultaneous negative material. Detail properties of metallic metamaterial including dispersion and transmission of electromagnetic waves will be explained in Chapter 3. The dispersion of the electromagnetic wave inside metallic metamaterial is calculated analytically and solved numerically. Initially one-dimensional structure has been considered for dispersion calculation (both analytically and numerically), and then three-dimensional structure has been considered and both results have been compared. Reflection spectrums of the metallic metamaterial and equivalent isotropic dielectric and anisotropic dielectric have also been calculated for TM polarized incident wave and compared. It has been found from the reflection spectrum that the behavior of the metallic metamaterial is similar to the anisotropic dielectrics and shown in Chapter 3. Chapter 4 focuses on the Cerenkov-like radiation in metallic metamaterial. It has been found that this metamaterial supports energy threshold free Cerenkov radiation and radiation angles, ($tan\theta = \beta = v_{beam}/c$) in the metamaterial is similar to that of an effective anisotropic medium. It has also been shown in this chapter that, the finite thickness of the metamaterial slab enforces the generated Cerenkov-like radiation such that it is resonantly excited in the structure at frequencies where the guided-mode and the beam-mode phase velocities become synchronous. In addition, the potential use of the metallic metamaterial in wakefield accelerator has also been discussed. The electromagnetic radiation generated by Cerenkov-like radiation in metallic metamaterial is confined inside the metamaterial structure and not coupled out from the structure. However, to use this metamaterial structure as an electromagnetic radiation source, the generated electromagnetic radiation has to couple out. In Chapter 5, the out-coupling mechanism of the generated electromagnetic radiation via Brillouin-zone-folding has been demonstrated. It has also been demonstrated that the electromagnetic radiation intensity of this metamaterial is much higher than that of the Smith-Purcell radiation intensity from a

metallic reflection grating. Finally, in Chapter 6, Summary of thesis along with future work has been presented.

CHAPTER 2

Metamaterial: A Brief Review

2.1 Introduction

2.2 Electric and Magnetic Responses of Metamaterial

2.2.1 Electric response

2.2.2 Magnetic response

2.3 Negative Refractive Index Metamaterial

2.4 Positive Refractive Index Metamaterial

2.5 Selection of Metamaterial for Interaction with Electron Beam

2.1 Introduction

All the materials can be categorized in four groups according to their electromagnetic properties as shown in figure 2.1.1. The first quadrant (Region I) represents the right handed materials which include most of the dielectric materials having both positive permittivity and permeability. Region II embraced the materials whose have negative permittivity up to certain frequencies (below the plasma frequency) but positive permeability. All metals, ferroelectric materials, and doped semiconductors are in this group. Region IV is consists of some ferrite materials with negative permeability and positive permittivity. However, magnetic responses of these materials quickly fade away above microwave frequencies. In addition to those three groups of material, there are another group of materials fall in Region III having very interesting properties, that is, both negative permittivity and permeability. However, there is no existence of such materials in nature but artificially composed and known as metamaterials. Meta(beyond)materials [33] are artificially engineered material whose properties do not exist in nature and this type of materials can exhibit the properties of simultaneous negative permeability and permittivity.

The electric permittivity (ε) and the magnetic permeability (μ) of any material depict the macroscopic response of that homogeneous material medium to the applied electric and magnetic fields. These are macroscopic parameters of any material which can be find out by calculating the time-averaged and spatially-averaged responses to the external field, averaged over sufficiently long times and sufficiently large spatial volumes. The electromagnetic field of the incident radiation does not resolve the meso-structures, but responds to the macroscopic resonances of the inhomogeneous materials where the inhomogeneities are on length-scales much smaller than a wavelength of the radiation but can be large compared with atomic or molecular length-scales. With this idea, a new class of material can be created. This new class of material (Metamaterial) can be characterized by macroscopic parameters such as ε and μ that define their response to applied electromagnetic fields, much like the homogeneous materials. Metamaterials are different from other structured photonic material i.e. photonic band-gap material [47],[48]. In case of photonic band-gap materials, the periodicity of the structure is of the order of the wavelength, and hence homogenization in this sense cannot be carried out. On the other hand, in the metamaterials the periodicity is far less than the

wavelength and all the properties mainly depend on the single cell (meta-atom) resonances.

Both the ε and μ of all causal materials are dispersive and in general complex functions of frequency because the polarizations in such media do not respond instantaneously to the applied fields but depend on the history of the applied fields. Near the resonance of the material oscillation, the response is in-phase and anti-phase with respect to the applied field at the frequencies below and above the resonance frequency, respectively. It can be possible to drive the negative real parts of the effective ε or μ if the resonance is sharp enough.

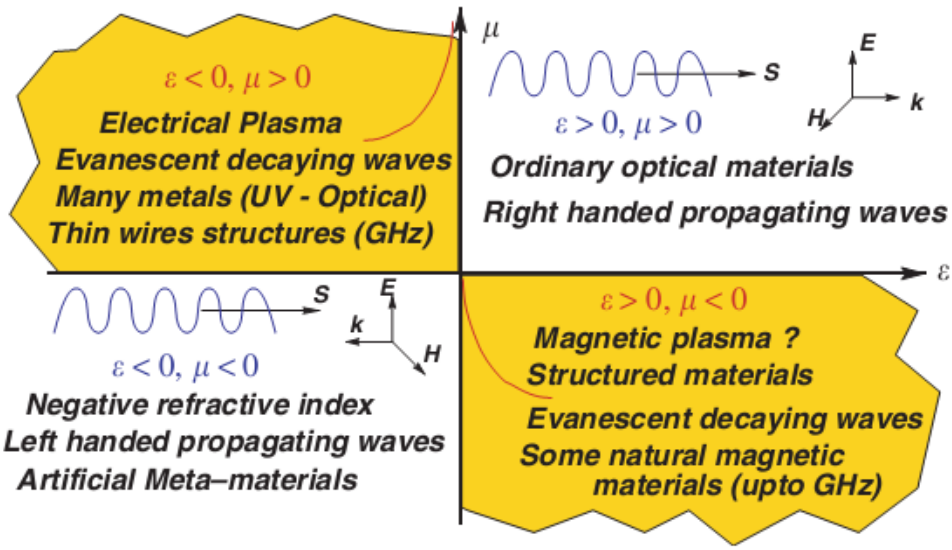

Figure 2.1.1: Classification of materials based on their dielectric and magnetic properties. The wavy lines represent propagating waves, and the axes set in quadrants 1 and 3 show the right and left-handed nature of *E, H* and *k* vectors. The waves in quadrants 2 and 4 decay evanescently inside the materials, which is depicted schematically. *S* is the Poynting vector [49].

2.2 Electric and Magnetic Responses of Metamaterial

2.2.1 Electric Response

Material properties are derived from oscillation of electric or magnetic charges under influence of external electromagnetic field [50]. In classical electromagnetics, Drude-Lorentz model [5] is the most suitable method to describe the material properties of any material. Due to the symmetry of EM waves, the frequency-dependent permittivity and permeability can be given as [51]:

$$\varepsilon_r(\omega) = 1 - \frac{\omega_{p,e}^2}{\omega^2 - \omega_{o,e}^2 + i\gamma_e\omega} \tag{2.2.1.1}$$

$$\mu_r(\omega) = 1 - \frac{\omega_{p,e}^2}{\omega^2 - \omega_{o,m}^2 + i\gamma_m\omega} \tag{2.2.1.2}$$

Where ω_p ($\omega_p^2 = \frac{n_e e^2}{\epsilon_o m_e}$) is the plasma frequency, ω_o is the resonant frequency, γ is the damping factor related to material losses, n_e is the total density of bound electrons (here it is assumed that all the electrons are bound with the same strength) and m_e is the mass of the electron. The subscripts e represents electric response. The plasma frequency for many metals lies in the ultraviolet frequency range and γ is small compared with ω_p. However, at lower frequency where $\omega \sim \gamma$, the dissipation dominates all phenomena and it can be hardly claimed that the dielectric constant is an almost real and negative number. Therefore to obtain the real and negative permittivity at the microwave frequency range, the plasma frequency has to reduce up to the microwave frequency range.

In 1996, Pendry et al. [52] have proposed one three-dimensional lattice of very thin metallic wires with wire radius r and periodicity $d << \lambda$ (wave length of incident radiation) and the applied electric field is considered to be parallel to the wires, as schematically shown in figure.2.2.1. In such structure, the effective electron density is apparently reduced and effective mass of the electrons are increased. The effective electron number density is reduced because

the radiation cannot sense the individual wire structure but only the average charge density and the effective electron mass is increased because of the self-inductance of the wire structure and it is not easy to change the currents flowing in these wires. The difficulty to change the current in the wire appears as if the charge carriers, namely the electrons, have acquired a tremendously large mass.

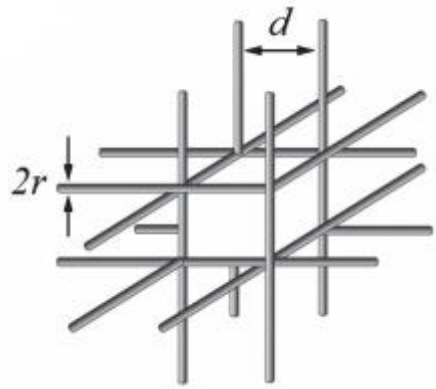

Figure 2.2.1: Schematic view of periodic wires (with radius *r*) arranged in a simple cubic lattice (with lattice constant *d*) [52].

2.2.2 Magnetic Response

The magnetic activity in most materials tends to tail off at high frequencies of even a few GHz. Therefore, it is indeed a challenge to obtain magnetic activities at those frequencies. Split ring resonators (SRRs) (figure 2.2.2) are one of the basic structures to get artificial magnetism. The SRR is composed of two concentric split rings with the openings at the opposite directions and it can be considered as a L-C equivalent circuit having resonance frequency $\omega_o = \sqrt{L/C}$, where *L* and *C* denoting the geometric inductance and capacitance of the SRR [53] structure, respectively. Within a certain frequency range centered at ω_o, a strong circulating current is induced on SRR when the magnetic flux threads through it. An effective magnetic moment is generated due to the strong induced current on SRR and the induced magnetic moment is either in phase or out of phase with respect to the external magnetic field. If the strength of the magnetic response is sufficiently strong, effective relative magnetic permeability μ_{eff} with a negative value can be achieved.

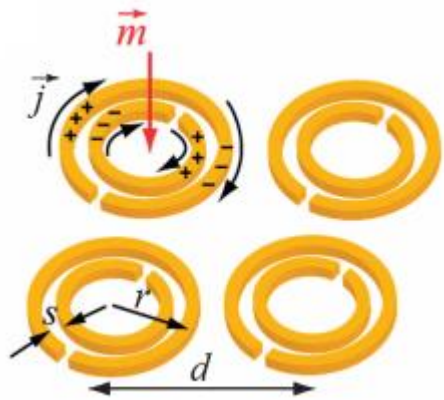

Figure 2.2.2: Schematic view of split ring resonators, with outer radius *r* and *s* is the separation between the two rings. A magnetic field penetrating the resonator induces a current ($\vec{j}$) and a magnetic moment ($\vec{m}$) [49].

2.3 Negative Refractive Index Metamaterial

In 2000, Smith [54] and his colleagues experimentally demonstrated for the first time that the metamaterials with a negative effective refractive index can be achieved in microwave frequency domain. They achieved metamaterials with a negative effective refractive index by overlapping two sets of meta-structures having both negative ε_{eff} and μ_{eff} in same frequency range [52-54]. The metamaterial with negative refractive index is a structure that consists of copper SRR and wire (figure 2.3.1). Then, in very next year, negative index of refraction is also verified by other group of researchers [55]. A considerable interest has been sparked in the field of electric metamaterials and the magnetic metamaterials, and consequently NIMs have been advanced from microwave frequencies to the visible region [56-58] within few years from the first experimental demonstration. The negative index at optical frequency is achieved by scaling down the structure size and taking cautious designs. However, it is shown in published literature [59] that to achieve magnetic resonance at optical frequencies, the size of SRRs has to be smaller than 100 nanometers, and the gaps should be less than 10 nanometers. This is very challenging to achieve and therefore, researchers were looking for other alternative to the combine structure of SRR and wires. Fishnet structure [60-62] is the most successful alternative to SRR and wire structure to achieve negative refractive index at optical frequency range. The Fishnet structure (figure 2.3.2) consists of layers of metal meshes

separated by dielectric spacers. In Fishnet structure, the paired strips that oriented to the electric field direction provide negative ε_{eff} and other paired stripes that are parallel to magnetic field provide negative μ_{eff}. This type of negative index material offers two important advantages: (1) the incident EM waves are normal to the fishnet sample surface for producing negative refractive index and (2) simplicity in designing and fabrication the fishnet structure. So far by using this Fishnet structure metamaterial, negative index of refraction is achieved at optical (Yellow light) frequency range [63].

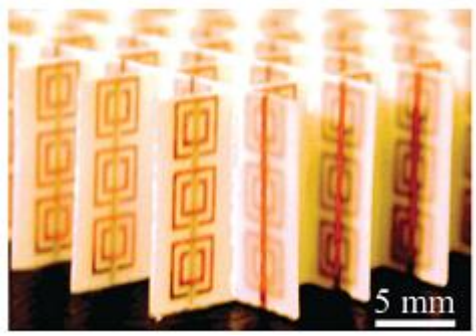

Figure 2.3.1: Negative index metamaterial formed by three-dimensional array of SRRs and wires [64].

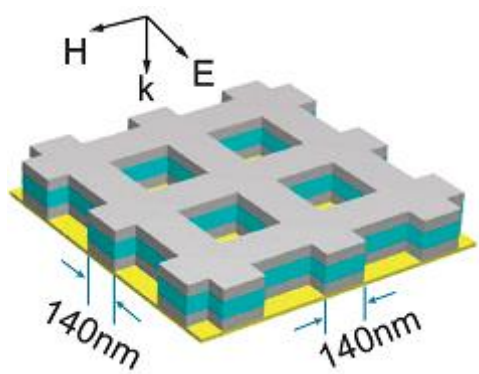

Figure 2.3.2: Schematic view of fishnet structure of negative index material in the visible region (yellow light) consisting of a dielectric layer (green color) between two metal layers (gray color) [63].

There are a lot of potential applications of metamaterial such as magnetic resonance imaging, novel microwave circuits and antennas at microwave frequency range [62-66]. In addition, Pendry has proposed a very unique application of negative index material, namely, perfect lens [67-68] (figure 2.3.3). In conventional optical systems, one cannot resolve two points separated by a distance less than $\lambda/2n$, where n is the refractive index of the ambient medium. The information of the object's fine features is carried by the evanescent wave which decays exponentially in space before reaching the image plane. However, a flat slab of negative index material can work as a perfect lens to recover all the lost information [67]. The concept of perfect lens has been experimentally demonstrated at microwave, mid-infrared and optical frequencies with different designs [68-73]. In another experiment [69], a silver thin film is used to enhance the evanescent wave and sub-diffraction-limited imaging with one-sixth of the illumination wavelength is accomplished. Another, perhaps, most exciting application of metamaterial is optical cloaking [74-78]. The cloaking, based on transformation optics is accomplished by manipulating the paths traversed by light through a novel optical material. Metamaterials direct and control the propagation and transmission of specified parts of the light spectrum and demonstrate the potential to render an object seemingly invisible. Moreover, modulation and switching of the electromagnetic wave is possible by the tunable metamaterial. Hou-Tong Chen et al [79] have demonstrated that the modulation of THz transmission is possible using a tunable metamaterial. They have fabricated an array of gold electric resonator elements (the metamaterial) on a semiconductor substrate and inter-connected all the resonant elements through conducting wires. A Schottky diode has been formed by the metamaterial array and the substrate. The substrate charge carrier density near the split gap has been controlled by the applied potential between the split ring resonator and the ohmic contact made on the substrate. Using this arrangement, the real ε of the structure can be changed with applied potential and thus the THz transmission can be modulated. In addition, the properties of metamaterial can be controlled by optical pumping [80-82].

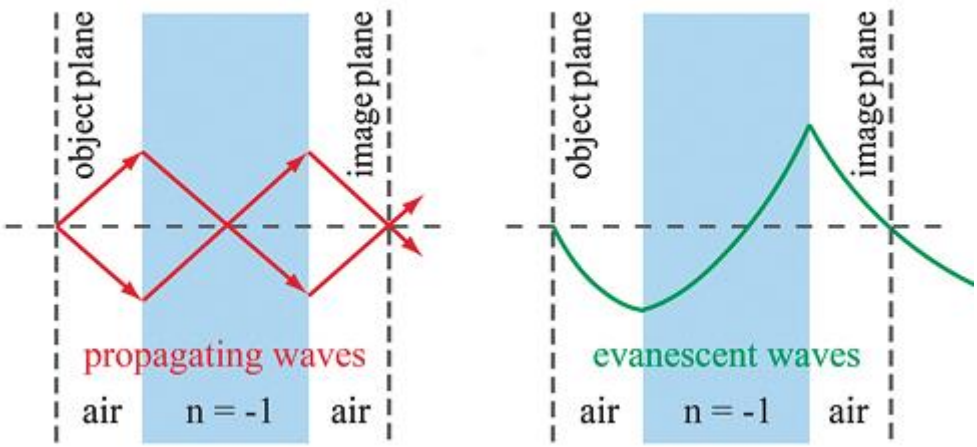

Figure 2.3.3: Pendry model of perfect lens, made from negative index flat slab material focusing all the light rays from a point source and amplifying to evanescent waves [64].

2.4 Positive Refractive Index Metamaterial

Metamaterials with negative index of refraction has been discussed in the preceding sections. Here, metamaterials with high positive index of refraction will be discussed to complete the spectrum of achievable refractive index. The wide spectrum of achievable refractive index material provides more design flexibility for transformation optics [75-77]. One-dimensional array of sub wavelength slits perforated on a perfect metal film offers frequency independent high refractive index as long as the period of slits is well less than the wavelength of incident waves [44],[46]. The refractive index of this system is entirely controlled by the geometrical parameters of the structure. In addition, a broadband, high-refractive-index, three-dimensional metamaterial structure was theoretically investigated and this structure consists of a cubic array of isolated perfect electric conductor (PEC) objects and have either an octahedral (O_h) or a pyritohedral (T_h) symmetry point group[45]. However, the proposed structure is not easy to be implemented. In 2011, Muhan Choi et al. [83] have demonstrated that a broadband, extremely high index of refraction can be realized from large-area, free-standing, flexible terahertz metamaterials composed of strongly coupled unit cells. They have used a thin 'I'-shaped metallic structure (figure 2.4.1) which can provide a pathway

to effectively reduce the diamagnetic effect, as a thin 'I'-shaped patch has a small area subtended by the current loops. In this structure, the effective permittivity is increased drastically through strong capacitive coupling and reduced diamagnetic response and they reported a peak refractive index of 38.6 along with a low-frequency quasi-static value of over 20 for single layer of such structure.

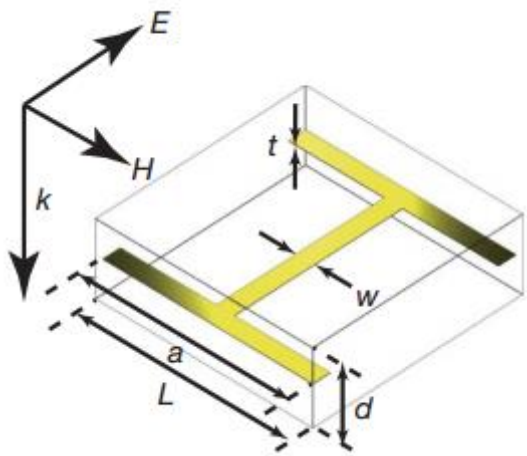

Figure 2.4.1: Unit cell structure of the high-index metamaterial where a thin 'I'-shaped metallic patch is symmetrically embedded in a dielectric material (*E*, *H* and *k* denote the electric field, magnetic field and propagation direction of the incident terahertz wave) [83].

2.5 Selection of Metamaterial for Interaction with Electron Beam

The metamaterials discussed preceding sections are typically consist of dielectrics and conductors or only conductors shaped in various geometries to couple the electric and magnetic field components of an incoming electromagnetic wave. The SRR and rod, typically, consists of dielectric and conductor, is a very common negative index metamaterial and it is resonant when the electric field of an electromagnetic wave is parallel to its surface (figure 2.5.1). In this structure, a split ring resonator and strip are formed on two faces of a dielectric slab respectively. The electron beam which passes through the top of this structure will interact with the electric field. This kind of metamaterial has been used in the previous experiment [84]. However, due to dielectric content, this metamaterial structure also has some limitations

in view of heat dissipation and voltage breakdown. The complementary SRR (CSRR), a complementary structure to SRR, will resonant when it is excited by a wave with an electric field normal to the surface (figure 2.5.2). Although, this CSRR structure can be made by pure metal, however, this structure is not preferable for use to interact with electron. Since the electron beam has to passes through the small gaps between two rings to interact with the electric field supported by this structure and this is very difficult to achieve as the gaps are considerably less and discrete. The another metamaterial, a periodic cut-through slit perforated on a metal film(metallic metamaterial), which is a pure metallic structure and shows dielectric like response to an electromagnetic wave with electric field in the direction parallel to the surface of the metamaterial (figure 2.5.3). The metallic metamaterial, being a pure metallic structure is preferable for interaction with electron beam due to its better heat dissipation capability and very high breakdown strength and therefore, in this thesis, this type of metamaterial is considered for interaction with electron beam and discussed in successive sections or chapters.

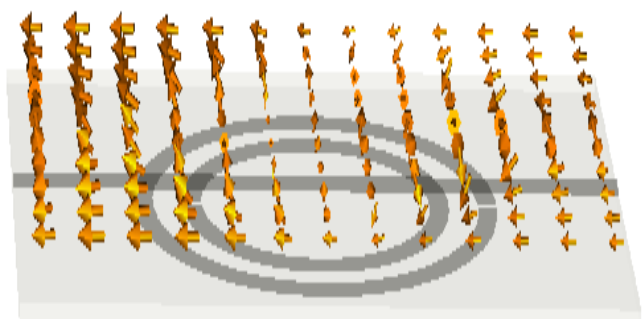

Figure 2.5.1: SRR (dark gray ring) and rod (dark strip) structure with electric field (arrows) parallel to the surface, on a dielectric slab (gray structure).

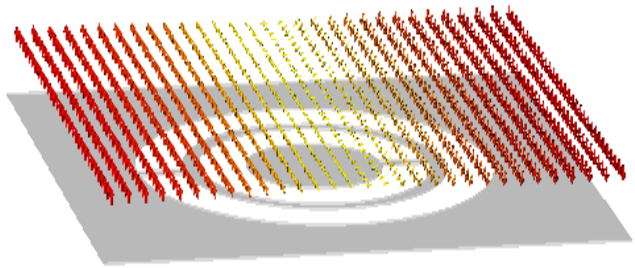

Figure 2.5.2: Complementary SRR (gray region) and its electric field pattern (arrows, perpendicular to the surface) on dielectric slab (white region).

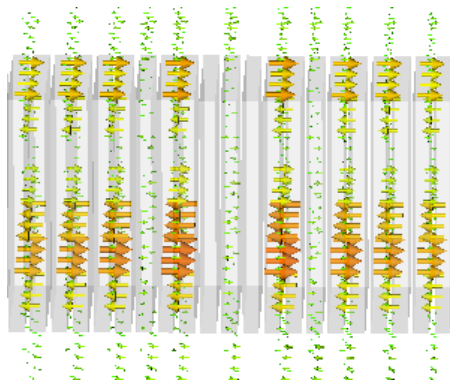

Figure 2.5.3: Simulated model of electric field pattern (arrows) of Metallic metamaterial (gray structure).

CHAPTER 3

Metallic Metamaterial

3.1 Introduction

3.2 Dispersion Relation

3.3 Graphical Mode Solution of Dispersion Relation

3.4 Numerical Simulation of Dispersion Relation

3.5 Dispersion Relation of a Metallic Metamaterial with Finite Transverse Width

3.6 Numerical Simulation of Dispersion Relation of Metallic Metamaterial with Finite Transverse Width

3.7 Anisotropic Dielectric Behavior of Metallic Metamaterial

3.8 Effect of Introduction of Side-Wall Boundaries in Metallic Metamaterial

3.1 Introduction

During last two decades, exploration of sub-wavelength structures has been drawn a great interest to create artificial materials with unusual effective electromagnetic responses. High-impedance surfaces used as a substrate of antenna [85-87], negative refractive index metamaterials [53-54],[88-89] effective surface plasmon behavior [90] on perfect metal surface with grating [91], effective bulk plasmon behavior in thin-wire structure[92-97], perfect metal film with a periodic arrangement of cut-through slits [98],[44],[46] etc., are the prominent examples of sub-wavelength structures. JT Shen et al [46] demonstrated that a frequency independent and arbitrarily high refractive index can be achieved with a metal film perforated with periodic cut-through slit (figure 3.1.1) when the periodicity (d) is in sub-wavelength limit in the length scale. The effective refractive index of this system is entirely controlled by structure geometry and such a capability is potentially important for miniaturization of optical or electromagnetic devices and for improving resolution in imaging. Existence of sub wavelength propagation modes inside structure is the key to create the desired effective refractive index behavior.

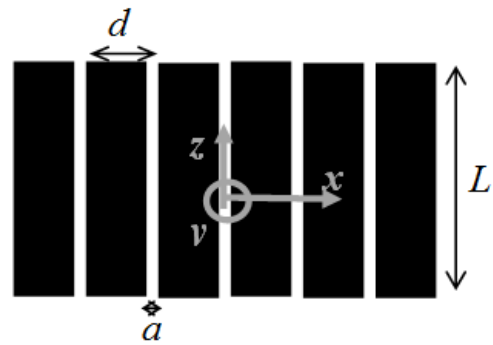

(A)

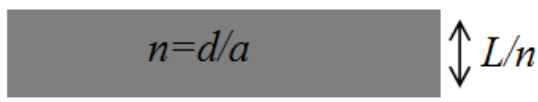

(B)

Figure 3.1.1: Schematic of the metal film (black regions) and vacuum part (white regions), (A) with periodic slits (*d*, *a*, *L* are the periodicity, width of the slit and thickness of the metal film, respectively) and. (B) its equivalent effective dielectric slab model [46].

3.2 Dispersion Relation

Due to existence of TEM mode and with the electric field along *x* direction inside the slit of width *a*, the structure permits perfect transmission of light through sub wavelength slit arrays (figure 3.2.1) [99-102]. Here, a TM polarization [103] of wave, namely, electric fields without *y*-direction component, a structure with infinitely extend transverse width (in '*y*') and without any external source are considered to derive the dispersion relation.

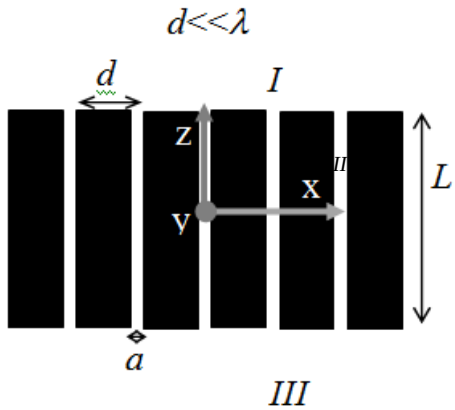

Figure 3.2.1: Schematic of different regions of metal slit, without any external source, extended in the *x-y* plane (with period much less than the incident wavelength) are: (i) above the metal film, (ii) inside slit and (iii) below of the metal film.

For the sake of simplicity, the origin of the coordinate system is considered at the center of one slit. The propagating magnetic and electric field expressions at the region above of the metal slit (region I) can be written as:

$$H_y^I = \sum_{p=-\infty}^{\infty} r_p \exp\left\{i\alpha_p\left(-Z-\frac{L}{2}\right)\right\}\exp(iG_p x) \tag{3.2.1}$$

$$E_x^I = \sum_{p=-\infty}^{\infty} \frac{\alpha_p}{\omega} r_p \exp\left\{i\alpha_p\left(-Z-\frac{L}{2}\right)\right\}\exp(iG_p x) \tag{3.2.2}$$

where first part of each equations represents the propagation along '*z*' and second part represents the propagating along '*x*' on metal slit surface. If the RF quantities vary as: $\exp j(\omega t - \alpha_p z)$, then $\frac{\partial}{\partial t} = j\omega$, $\frac{\partial}{\partial z} = -j\alpha_p$ and from Maxwell's equation $\nabla \times \vec{E} = \frac{\partial \vec{B}}{\partial t}$, we get $\vec{E} = \frac{\omega}{\alpha_p}\vec{B}$. Where r_p is the reflection coefficient, $\alpha_p = \sqrt{k^2 - G_p^2}$ is the momentum along '*z*' and $G_p = k_x + 2\pi/p$ is the parallel quasi-momentum along the metal surface (along *x*).

Unlike in region *I*, in region *II*, i.e. inside each slit, a standing wave is formed due to reflection at the end of the slit and the magnetic and electric field inside slit can be written as

$$H_y^{II} = A_m cos\frac{\omega}{c}z + B_m sin\frac{\omega}{c}z \tag{3.2.3}$$

$$E_x^{II} = -\frac{\omega/c}{i\omega}\left(A_m sin\frac{\omega}{c}z - B_m cos\frac{\omega}{c}z\right) \tag{3.2.4}$$

Similar to region *I*, in region *III* fields are propagating in nature at region and the magnetic and electric field expressions can be written as:

$$H_y^{III} = \sum_{p=-\infty}^{\infty} t_p \exp\left\{i\alpha_p\left(z-\frac{L}{2}\right)\right\}\exp(iG_p x) \qquad (3.2.5)$$

$$E_x^{III} = \sum_{p=-\infty}^{\infty} \frac{\alpha_p}{\omega} t_p \exp\left\{i\alpha_p\left(z-\frac{L}{2}\right)\right\}\exp(iG_p x) \qquad (3.2.6)$$

where t_p is transmission coefficient.

Both the magnetic and the electric field are continuous at the interface of two medium when there is no charge and surface current on structure surface. The boundary conditions [104] can be written as follows

$$H_y^{II}\left(z=\frac{L}{2}\right) = H_y^{III}\left(z=\frac{L}{2}\right) \qquad (A)$$

$$E_x^{II}\left(z=\frac{L}{2}\right) = E_x^{III}\left(z=\frac{L}{2}\right) \qquad (B)$$

From boundary condition (A) and for even mode B_m =0 (because '*sine*' is an odd function)

$$A_m \cos\left(\frac{\omega L}{2c}\right) = \sum_{p=-\infty}^{\infty} t_p \exp(iG_p x) \qquad (3.2.7)$$

$$A_m = \frac{\sum_{p=-\infty}^{\infty} t_p \exp(iG_p X)}{\cos\left(\frac{\omega L}{2c}\right)} \qquad (3.2.8)$$

Integrating both sides about m^{th} slit and dividing it with slit width (*a)* to obtain the average magnetic field, one gets

$$\frac{1}{a}\int_{md-a/2}^{md+a/2} A_m dx = \frac{1}{a}\int_{md-a/2}^{md+a/2} \frac{\sum_{p=-\infty}^{\infty} t_p \exp(iG_p x)}{\cos\left(\frac{\omega L}{2c}\right)} dx \qquad (3.2.9)$$

$$\frac{1}{a}A_m a = \frac{1}{a\cos\left(\frac{\omega L}{2c}\right)}\sum_p t_p \left[\exp\left\{iG_p\left(md+\frac{a}{2}\right)\right\} - \exp\left\{iG_p\left(md-\frac{a}{2}\right)\right\}\right. \qquad (3.2.10)$$

$$\frac{1}{a}A_m a = \frac{1}{aG_p\cos\left(\frac{\omega L}{2c}\right)}\sum_p t_p \left[\exp\{iG_p md\}\right]]\left[\exp\{iG_p a/2\} - \exp\{iG_p a/2\}\right] \qquad (3.2.11)$$

$$A_m = \frac{\sum_p t_p}{\cos\left(\frac{\omega L}{2c}\right)}\exp(iG_p md)\, sinc(G_p a/2) \qquad (3.2.12)$$

Now from boundary condition (B) and for even modes

$$\sum_{p=-\infty}^{\infty} \frac{\alpha_p}{\omega} t_p \exp\left(iG_p x\right) = \frac{\omega/c}{i\omega} A_m \sin\left(\frac{\omega L}{2c}\right) \tag{3.2.13}$$

$$A_m = -\frac{i}{k_z} \frac{\sum \alpha_p t_p \exp(iG_p x)}{\sin\left(\frac{\omega L}{2c}\right)} \tag{3.2.14}$$

Multiplying equation (3.2.14) both sides by $\exp(-iG_p^{'}x)$ and taking average over a period (electric field averaging over a period) one gets

$$\frac{1}{d}\int_{md-d/2}^{md+d/2} A_m \exp(-iG_p^{/} x)dx = \frac{1}{d}\int_{md-d/2}^{md+d/2} \left(\frac{i}{\omega/c}\right) \frac{\sum_{p=-\infty}^{\infty} \alpha_p t_p \exp\{i\left(G_p - G_p^{/}\right)\}}{\sin\left(\frac{\omega L}{2c}\right)} \tag{3.2.15}$$

Since the fields exit only inside the slit, the integration limit can be changed into *md* ± *a/2*

$$\frac{1}{a}\int_{md-a/2}^{md+a/2} A_m \exp(-iG_p^{/} x)dx = \frac{1}{a}\int_{md-a/2}^{md+a/2} \left(\frac{i}{\omega/c}\right) \frac{\sum_{p=-\infty}^{\infty} \alpha_p t_p \exp\{i\left(G_p - G_p^{/}\right)\}}{\sin\left(\frac{\omega L}{2c}\right)} \tag{3.2.16}$$

If $G_p = G_p^{'}$, then equation (3.2.16) reduces to

$$\frac{1}{a}\int_{md-a/2}^{md+a/2} A_m \exp\left(-iG_p x\right) dx = \frac{1}{a}\int_{ma-a/2}^{ma+a/2} \left(\frac{i}{\omega/c}\right) \frac{\sum_{p=-\infty}^{\infty} \alpha_p t_p}{\sin\left(\frac{\omega L}{2c}\right)} \tag{3.2.17}$$

$$\frac{1}{a} A_m \left[\frac{\exp\left\{iG_p\left(md+\frac{a}{2}\right)\right\} - \exp\left\{iG_p\left(md-\frac{a}{2}\right)\right\}}{-iG_p}\right] = \frac{d}{a}\left(\frac{-i}{\omega/c}\right) \frac{\sum t_p \alpha_p}{\sin\left(\frac{\omega L}{2c}\right)} \tag{3.2.18}$$

$$A_m \left[\frac{\exp(-iG_p)\{exp\left(-\frac{iG_p a}{2}\right) - \exp\left(iG_p \frac{a}{2}\right)\}}{-\frac{2iG_p a}{2}}\right] = \frac{d}{a}\left(\frac{-i}{\omega/c}\right) \frac{\sum t_p \alpha_p}{\sin\left(\frac{\omega L}{2c}\right)} \tag{3.2.19}$$

$$t_p = \left(-\frac{\omega/c}{i}\right) \frac{f}{\alpha_p} \sin\left(\frac{\omega L}{2c}\right) g_p \exp(-iG_p md) A_m \tag{3.2.20}$$

where $g_p = sinc\left(\frac{G_p a}{2}\right)$

Substituting the value of t_p into equation (3.2.13), one can obtain

$$A_m = \frac{(-\frac{\omega/c}{i})\frac{f}{\alpha_p}\sin(\frac{\omega L}{2c})g_p \exp(-iG_p md)A_m}{\cos(\frac{\omega L}{2c})}\exp(iG_p md)g_p \qquad (3.2.21)$$

where $f = a/d$ and $\emptyset = \sum f g_p^2 \frac{\omega/c}{\alpha_p}$

Then, solving equation (3.2.21) through (3.2.20), the dispersion relation for even modes can be written as

$$\frac{1}{i\emptyset} = \tan(\frac{\omega L}{2c}) \qquad (3.2.22)$$

Similarly, the dispersion relation for odd mode can be obtained as:

$$\frac{i}{\emptyset} = -\cot(\frac{\omega L}{2c}) \qquad (3.2.23)$$

3.3 Graphical Mode Solution of Dispersion Relation

Solving the simultaneous equations (3.2.22) (even modes) and (3.2.23) (odd modes) for the values of k_x and ω is difficult, because the equations are transcendental. But it is easy to find an approximate solution using a graphical technique [105]. This also provides valuable physical insight. To get graphical solution, the equation (3.2.22) is divided into two equations

$$f_1 = \frac{1}{i\emptyset(k_x,\omega)} \qquad (3.3.1)$$

$$f_2 = tan(\frac{\omega L}{2c}) \qquad (3.3.2)$$

The idea is to plot these equations on the same abscissa (ω) (in unit $2\pi c/d$). The equation (3.3.1) is plotted by blue lines in figure 3.3.1 and equation (3.3.2) is plotted for different k_x (in unit of $2\pi/d$) (black lines). Each intersection of the curves corresponds to a mode. The coordinates of theses point give us the values of k_x and ω. Dispersion relation has been solved using MATLAB [107] and first three modes are shown in figure 3.3.2.

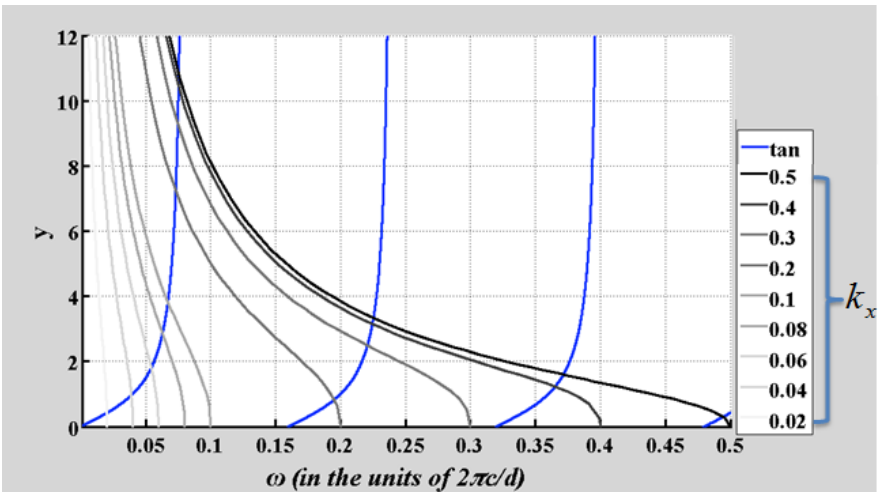

Figure 3.3.1: Graphical mode solution of equations (3.3.1) (black and gray lines) and (3.3.2) (blue lines), taking k_x as the parameter

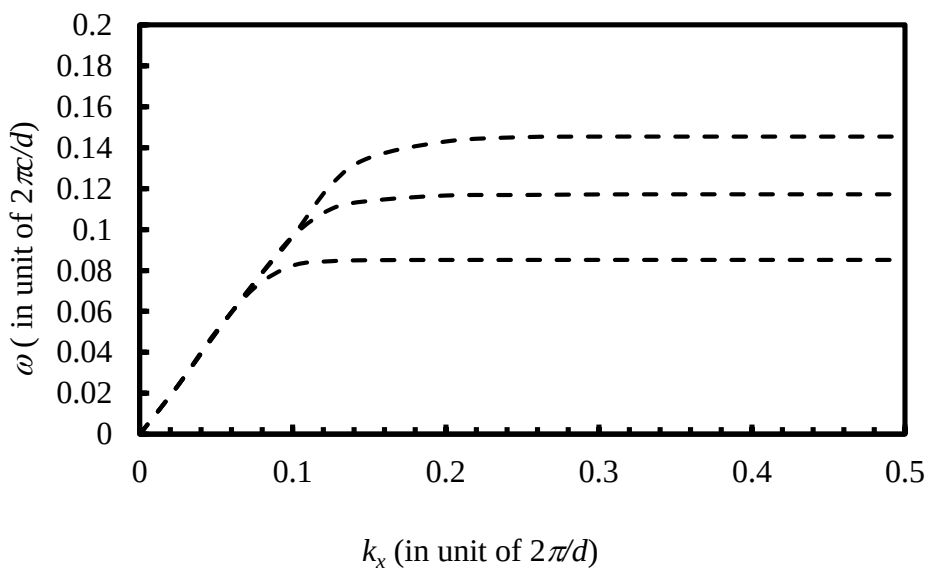

Figure 3.3.2: Dispersion relation (analytical solution) of first three guided modes supported by metal slit for $n = d/a = 4$.

3.4 Numerical Simulation of Dispersion Relation

The guided mode dispersion relation of the metal slit structure has also been solved using finite-difference frequency-domain (FDTD) method. In this calculation, the wave equation for H_z in the case of transverse-magnetic (TM) polarization has been solved. The computational domain consists of a single period of structure and periodic boundary condition has been applied on left and right boundaries as shown in figure 3.4.1. Others boundaries are set as perfect absorbing boundaries (PAB). In this simulation, a FDTD code CST [106] has been used. The structure with period d and thickness L is modeled in this FDTD code as a thick film of perfect electric conductor (PEC) with periodic cut-through slit on it (figure 3.4.1).

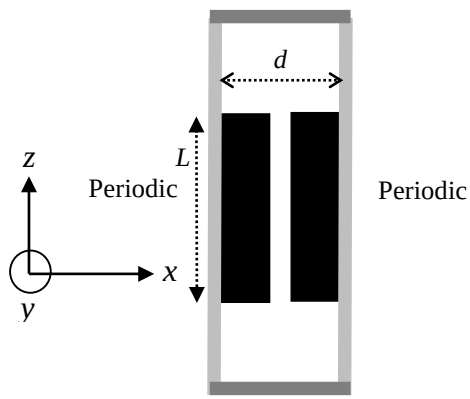

Figure 3.4.1: Simulated FDTD model of a single period structure with periodic boundary conditions applied on left and right boundaries.

The slits in the metallic film, irrespective of their narrow dimensions always support a propagating state which gives rise to a series of effective dielectric slab modes [98]. These modes follow the light line in vacuum at low frequency. The E_x-field distribution of the fundamental effective dielectric slab mode and the next two higher-order effective dielectric slab mode are shown in figure 3.4.2 where the maximum E_x-field are within the slits for all modes.

The dispersion of guided modes of the structure is shown in the figure 3.4.3 where at large momentum (k_x), the frequencies approach a series of limiting values. These frequencies are

determined by structure parameters. Figure 3.4.3 shows the comparison of dispersion of guided modes obtained from analytical calculation and those from numerical simulation and a close agreement is found.

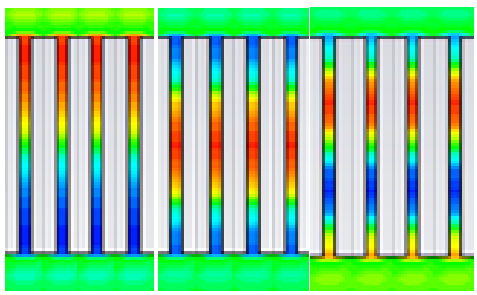

(a) (b) (c)

Figure 3.4.2: Electric field contour (E_x) inside slit for, (a) first guided mode, (b) second guided mode and (c) third guided mode.

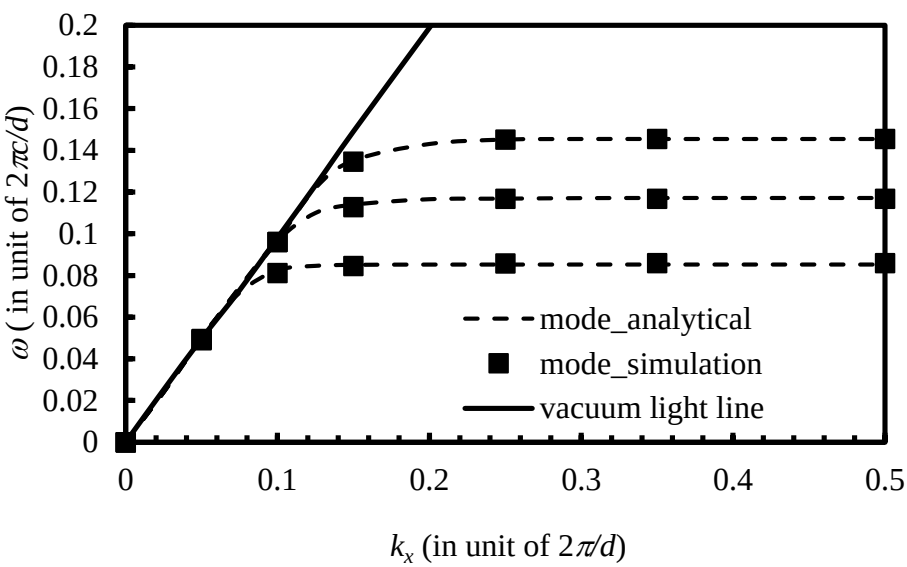

Figure 3.4.3: Dispersion characteristics of first three guided modes of metal slit with period d and slit width a.

3.5 Dispersion Relation of Metallic Metamaterial with Finite Transverse Width

So far the considered metallic metamaterial structure is a one-dimensional structure with infinite dimension in transverse direction (in *y*) and vacuum (ε_r =1) is the ambient dielectric medium in slits region. This kind of structure is very much difficult to realize due to its infinite transverse dimension. In practical structures, there should be finite dimension in all three directions as shown in figure 3.5.1. Therefore, the effect of finite transverse dimension of the considered structure on its dispersion has to be studied. For this purpose, the dispersion relation of metallic metamaterial structure having finite transverse dimension is derived as follows.

Similarly, TM polarization [103] of wave, namely, electric fields without *y*-direction component and three different regions, (i) above the metal film, (ii) inside slit and (iii) below the metal film are considered.

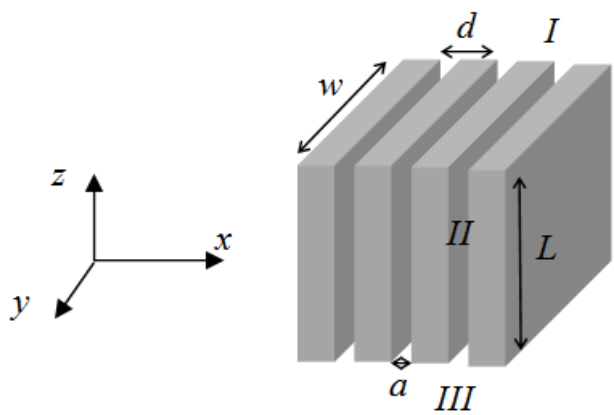

Figure 3.5.1: Three-dimensional model of a metallic metamaterial structure (origin of coordinate system is considered at center of one slit and *I*, *II* and *III* refers to the regions above the structure, inside the slit and below the structure, respectively).

The electric and magnetic field expression in three different regions are written as

$$E_x^I = \sum_{p=-\infty}^{\infty} \frac{\propto_p}{\omega} r_p \exp\{\left(i\alpha_p \left(-z - \frac{L}{2}\right)\right\} \exp(iG_p x) \quad (3.5.1)$$

$$H_y^I = \sum_{p=-\infty}^{\infty} r_p \exp\left\{i \propto_p \left(-Z - \frac{L}{2}\right)\right\} \exp(iG_p x) \quad (3.5.2)$$

$$E_x^{II} = -\frac{\omega/c}{i\omega}(A_m sin\frac{\omega}{c}z - B_m cos\frac{\omega}{c}z) sink_y y \quad (3.5.3)$$

$$H_y^{II} = (A_m cos\frac{\omega}{c}z + B_m sin\frac{\omega}{c}z) sink_y y \quad (3.5.4)$$

$$E_x^{III} = \sum_{p=-\infty}^{\infty} \frac{\alpha_p}{\omega} t_p \exp\left\{i\alpha_p \left(z - \frac{L}{2}\right)\right\} \exp(iG_p x) \quad (3.5.5)$$

$$H_y^{III} = \sum_{p=-\infty}^{\infty} t_p \exp\left\{i\alpha_p \left(z - \frac{L}{2}\right)\right\} \exp(iG_p x) \quad (3.5.6)$$

where, superscript *I*,*II*,*III* represent the regions *I*,*II* and *III* respectively and subscript *x*,*y* and *z* represent the *x*, *y* and *z* components of electric (*E*) and magnetic (*H*) fields. k_y is the propagation constant along *y* direction inside slit.

Similar to one-dimensional assumption, both the magnetic and the electric field are continuous at the interface of two mediums when there is no charge and surface current on structure surface. The boundary conditions [104] can be written as follows

$$E_x^{II}\left(z = \frac{L}{2}\right) = E_x^{III}(z = \frac{L}{2}) \quad (A1)$$

$$H_y^{II}\left(z = \frac{L}{2}\right) = H_y^{III}(z = \frac{L}{2}) \quad (B1)$$

From equation (3.3.3), (3.3.4), (3.3.5), (3.3.6), boundary conditions (A1) and (B1) and for even mode B_m =0 (because '*sine*' is an odd function), the following equations are obtained.

$$A_m = \frac{\sum_{p=-\infty}^{\infty} t_p \exp(iG_p X)}{\cos(\frac{\omega L}{2c})\sin(k_y y)} \quad (3.3.7)$$

$$A_m = -\frac{i}{k_z} \frac{\sum \alpha_p t_p \exp(iG_p X)}{\sin(\frac{\omega L}{2c})\sin(k_y y)} \quad (3.3.8)$$

Integrating and dividing both sides by slit width about m^{th} slit to average the magnetic field as in the previous case, one obtains

$$\frac{1}{a}\int_{md-a/2}^{md+a/2} A_m dx = \frac{1}{a}\int_{md-a/2}^{md+a/2} \frac{\sum_{p=-\infty}^{\infty} t_p \exp(iG_p x)}{\cos(\frac{\omega L}{2c})\sin(k_y y)} dx \quad (3.3.9)$$

Solving for A_m, the following equation is obtained

$$A_m = \frac{\sum_p t_p}{\cos(\frac{\omega L}{2c})\sin(k_y y)} \exp\left(iG_p md\right) sinc(G_p a/2) \quad (3.3.10)$$

Using similar process as in the case of one-dimension, the following equation is obtained.

$$t_p = \left(-\frac{\omega/c}{i}\right)\frac{f}{\alpha_p}\sin(\frac{\omega L}{2c}) g_p \exp(-iG_p md)\sin(k_y y) A_m \quad (3.3.11)$$

The even eigen mode dispersion is obtained by substituting equation (3.3.11) into (3.3.10) and rearranging. The even eigen mode dispersion is given by the following expression.

$$\frac{1}{i\emptyset} = \tan(\frac{\omega L}{2c}) \quad (3.3.12)$$

In similar manner the dispersion relation of odd eigen modes can be derived and it is given by the following expression.

$$\frac{i}{\emptyset} = -\cot(\frac{\omega L}{2c}) \quad (3.3.13)$$

It may be noted that same dispersion relations are obtained for the two-dimensional and the three-dimensional structures.

3.6 Numerical Simulation of Dispersion Relation Metallic Metamaterial with Finite Transverse Width

The dispersion relation of metallic metamaterial with finite transverse width is also calculated numerically for different transverse dimensions (w). A unit cell of this metamaterial structure is modeled in a FDTD code [106] as a thick film of a perfect electric conductor (PEC) with cut-through slit on it (figure 3.6.1). In this model, periodic boundary condition is applied in x direction and other boundary is set as perfectly absorbing boundary (PAB). The dispersion relations of eigen modes of this structure is shown in figure 3.6.2 for different width (w) of the structure. The boundaries in y and z are taken as far from the structure to minimize the boundary effects. From figure 3.6.2 it is observed that the eigen mode dispersion of metamaterial structure is independent of the transverse width of this structure and this result supports the analytical formulation of the dispersion relation.

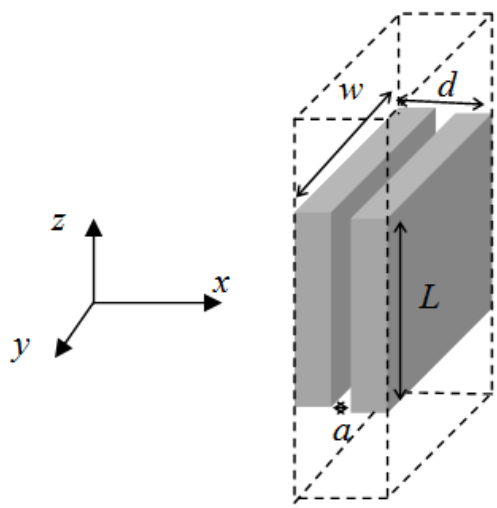

Figure 3.6.1: Schematic view of unit cell of metamaterial structure (planes bounded by dotted lines are the boundaries of the solution volume, and planes are perfect absorbing boundaries except two periodic boundaries along y-z plane).

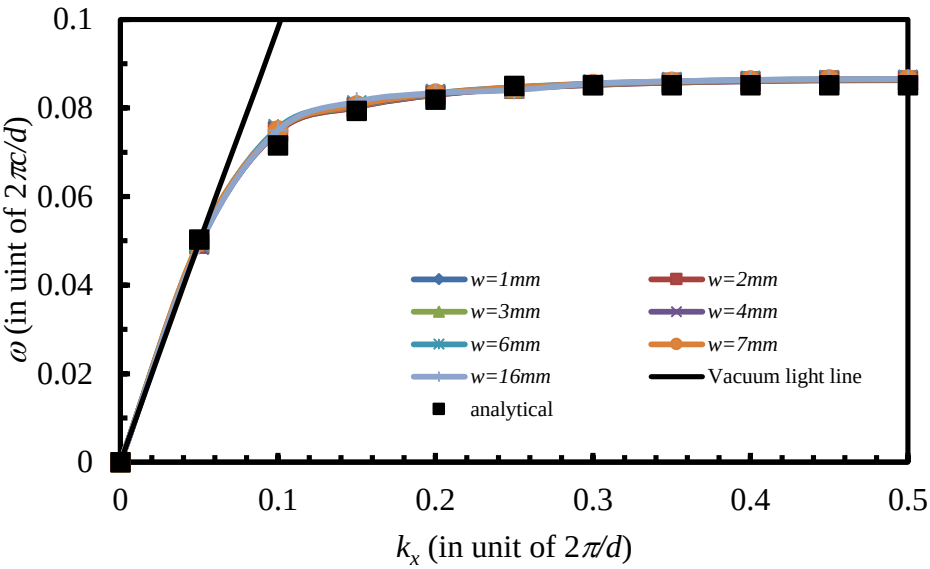

Figure 3.6.2: Effect of structure transverse width on dispersion characteristics for first eigen mode (overlapping of curves represents that dispersion is independent of transverse width of the structure).

3.7 Anisotropic Dielectric Behavior of Metallic Metamaterial

In case of an array of cut-through slit perforated on metal film, the system can be accurately described using a simple, isotropic, nonmagnetic (μ=1) model when the slit width a is sufficiently narrow compared to the sub wavelength period d [44]. However, this isotropic model starts deviating from exact isotropic model when $d/a \leq 4$ [44], and it behaves rather like an anisotropic dielectric. To verify the similarity of metal slit structure with anisotropic dielectric, reflection coefficient of an isotropic dielectric, an anisotropic dielectric and metal slit is studied for normally incident electromagnetic wave. Two types of polarization of the incident waves with electric field in x (polarization 1) and in y (polarization 2) direction are considered in this study. The structure parameter and polarization of incident waves on the structure is shown in table 3.7.1. The structure sketches are not in scale though thicknesses of all the structures are same. The structure thickness is L for all structures. For anisotropic dielectric the electrical permittivity in y and z direction is set to a very high value to simulate

the anisotropic behavior of the dielectric. Magnetic permeability of both anisotropic and isotropic dielectric is set as 1 (same as nonmagnetic material) for all three directions. In case of metal slit, the magnetic permeability and electrical permittivity of slit is set equal to those of the free space.

The reflection spectrum of metal slit (metallic metamaterial), isotropic dielectric and anisotropic dielectric, for normally incident wave with electric field in x direction, is shown in figure 3.7.1. This spectrum is calculated using the FDTD [106] simulation. The reflection coefficient becomes minimum (corresponds to maximum transmission) when $kL = m\pi$, as expected from the Fabry-Perot [108] resonance condition in the slit. Here, k is the wave vector along propagation direction, L is thickness of slab and m is an integer. It is observed from figure 3.7.1 that for higher d/λ the reflection spectrum of metal slit is deviated from that of the anisotropic and isotropic dielectric. As frequency increases (e.g. d/λ increases), the effective medium assumption gradually fails resulting the deviation in reflection spectrum. However, at lower frequency, the effective medium assumption is well valid because of lower d/λ and, therefore reflection spectrum of metal slit is remarkably matched with that of anisotropic dielectric and anisotropic dielectric.

In contrary, in the case of incident wave with electric field in y direction, the reflection spectrum of metal slit and anisotropic dielectric are different from that of the isotropic dielectric. However, the reflection spectrum of metal slit and anisotropic dielectric are similar (figure 3.7.2).

The anisotropic dielectric like behavior of the metal slit structure is also confirmed by the electric field distribution inside the three structures for normal incident waves of two different polarizations. As shown in table 2, inside isotropic dielectric, the electric field is present for both polarizations of incident wave at the frequencies where reflection coefficients are minimum. However, in the case of metal slit and anisotropic dielectric, the electric field is present inside the structures only for incident wave of polarization 1. For polarization 2, no electric field is present inside the anisotropic dielectric and metal slit. From these observations, it can be argued that the metal slit can be regard as effective anisotropic dielectric.

Table 3.7.1: Three different structures with their respective material properties and direction of electric field (blue arrows) of incident waves. The sketch of structures are not in scale, however the dimensions of all structure are identical in all the three directions.

Structures	Polarization #1 (‖ polarization) (incident *E* field in '*x*')	Polarization #2 (⊥ polarization) (incident *E* field in '*y*')
Isotropic dielectric (ε =16→ *n*=4)	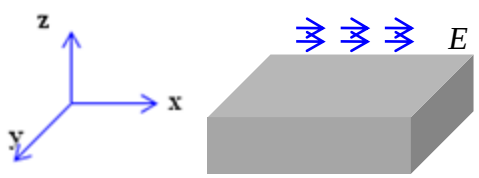	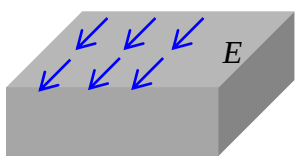
Anisotropic dielectric (ε_x =4, ε_y =999, ε_z =999)	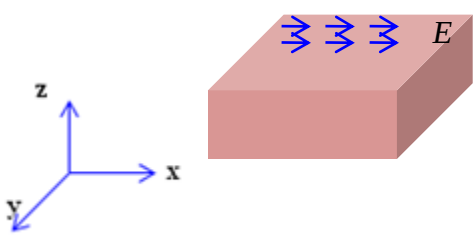	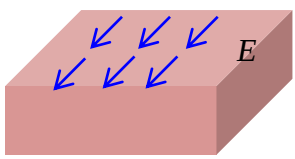
Metal (PEC) slit (*d*/*a* =4)	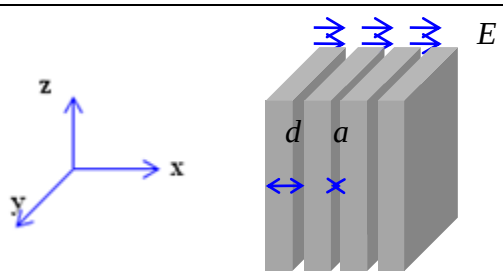	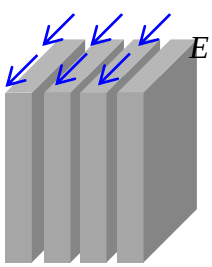

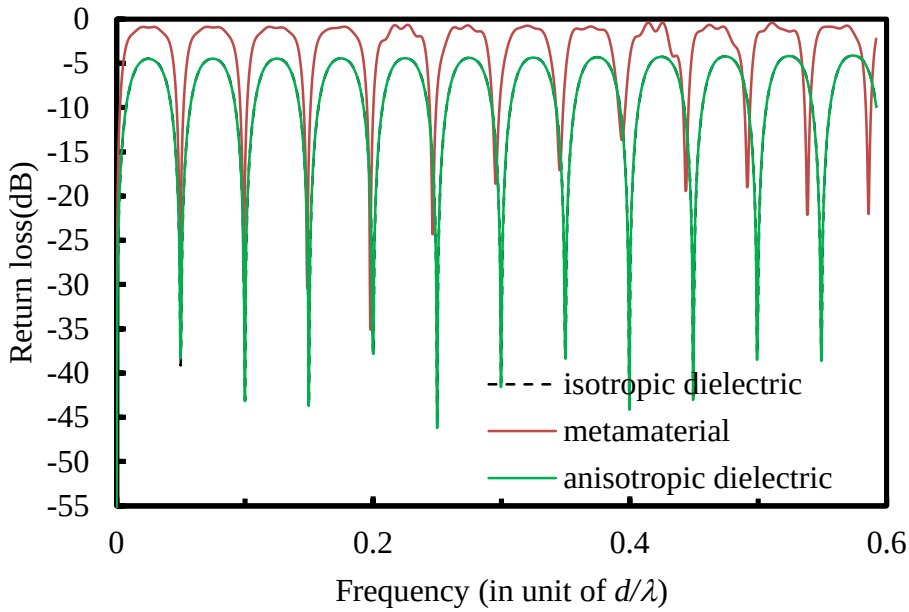

Figure 3.7.1: Variation of return loss with normalized frequency (d/λ) for polarization of the metal slit (red lines), effective anisotropic (green line) and isotropic (black dashed line) dielectric slab, keeping period and width of slit constant (Table-3.7.1)

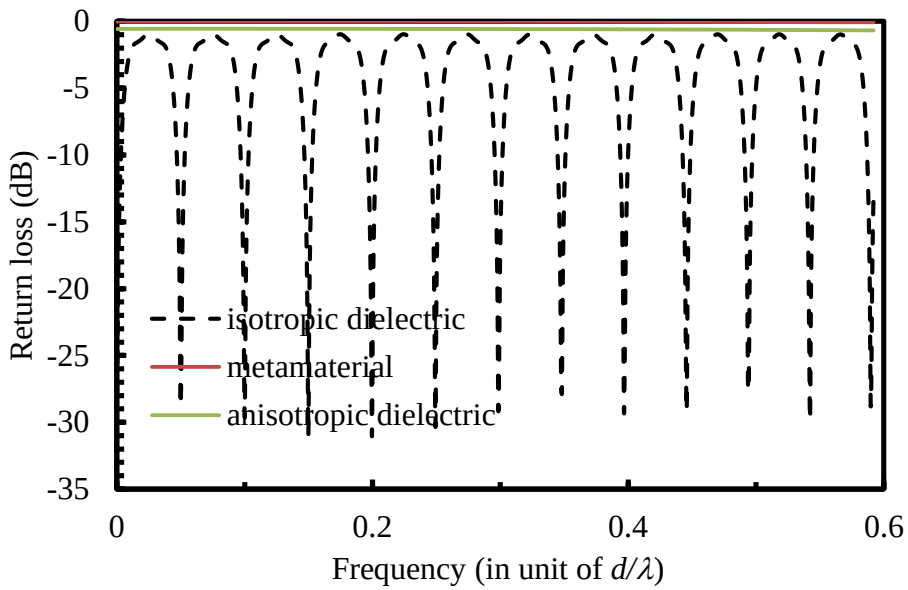

Figure 3.7.2: Variation of return loss with normalized frequency (d/λ) for polarization-2, of the metal slit (red lines), effective anisotropic (green line) and isotropic (dotted line) dielectric, for fixed d and a.

Table 3.7.2: Electric field (E_x) contour at inside the dielectric slab (bounded by thin black line) and metal slit and outside the structure. Normal incidence and two types of polarizations are considered. The origin of the coordinate system is at the center of corresponding structures and electric field contours are shown on x-z plane (y=0).

Structure	Polarization 1 (‖ polarization) (incident E field along 'x')	Polarization 2 (⊥ polarization) (incident E field along 'y')
Isotropic dielectric (ε =16→ n=4)	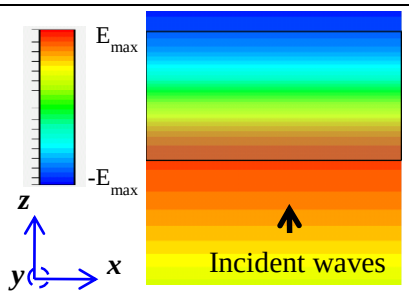	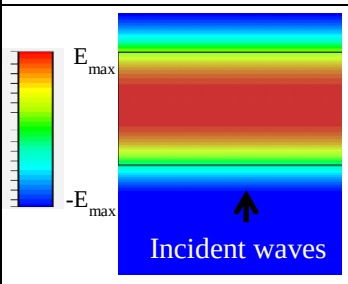
Anisotropic dielectric (ε_x =4, ε_y =999, ε_z =999)	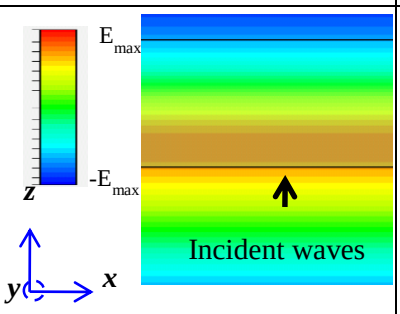	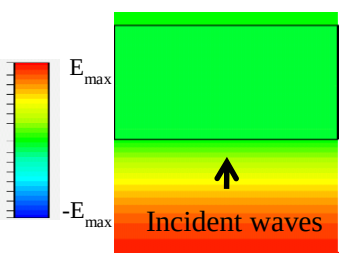
Metal slit (d/a =4)	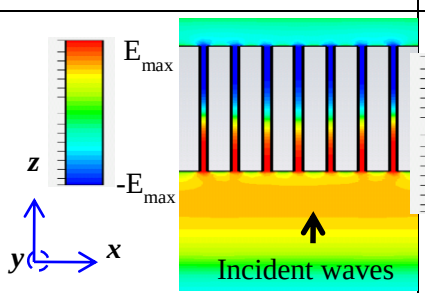	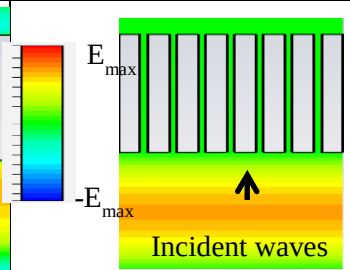

3.8 Effect of Introduction of Side-Wall Boundaries in Metallic Metamaterial

The metallic metamaterial structure, mentioned above is a two dimensional metal slit structure with infinite transverse (y) dimension and vacuum (ε_r=1) is the ambient dielectric medium in the slits region. This structure is simmilar to an array of free-standing fringes. However, realization of this type of structure is very difficult. For practical realization of this structure, a suporting structure, which can support the fringes and maintain the periodicity of the fringes is required. The metal slit with metallic extrusion at one end (termed as metal slit with side wall) is very simple to realize (figure 3.8.1), however, introduction of sides wall may effect the dispersion of guided modes. Therefore, it is required to study the eigen modes suported by this structure. The dispersion of this structure is calculated numerically as well as using FDTD code [27]. A unit cell of this structre is modelded as a thick film of a perfect electric conductor (PEC) with cut-through slit on it (figure 3.8.2). In this model, periodic boundary condition is applied in x direction and other boundary is set as perfectly absorbing boundary (PAB). The boundaries in y and z are taken as far from structure to minimize the boundary effects. The eigen mode dispersion of two structures (with and without side wall) for different transverse width (w) of structure is shown in figure 3.8.3. It can be seen from the figure 3.8.3 that the first eigen mode frequency of the structure with side wall is similar with that of structure without side wall only when the width of the former structure is more than 2λ. The wavelength λ corresponds to the eigen mode frequency for structure without side wall. The variation of eigen mode frequencies of both structure with transverse width of structure can be explained by a simple analytical expression of resonance frequency $f = \lfloor (u/a)^2 + (o/w)^2 + (q/L)^2 \rfloor^{1/2}$, where, u, o, and q are the number of half-wavelength variation inside the slit along x, y and z directions, respectively. Before calculating the resonance frequency for both cases, the electric field (E_x) inside the slit is analyzed for both structures. Figures 3.8.4(a)-3.8.4(c) show the field (E_x) variation along transverse width (along y), height (along z) and in axial direction (along x) of the metal slit structure without the side wall, respectively. In these plots, the shaded region indicates the region inside the slits. It is also cleared from these figures that electric field (E_x) has no variation along x and y directions, however, a half wavelength variation is observed along z direction. In case of metamaterial

with side wall, there is $\lambda/4$ variation of E_x in the y, no variation in x direction, (figure 3.8.5(a) and figure 3.8.5(b)), and there is a $\lambda/2$ variation of E_x in the z direction (figure 3.8.5(c)). This phenomena occurs because the electric field will have to satisfy the boundary conditions at the metal surface introduced at the end of the slit, i.e. the E_x field will have to be zero. It may be noted that in the metamaterial without side wall, the electric field E_x will not be zero at the end of the slit. Figure 3.8.5 shows the of variation of first eigen mode frequency of a metal slit structure with side wall, calculated from numerical simulation and simple analytical formula.

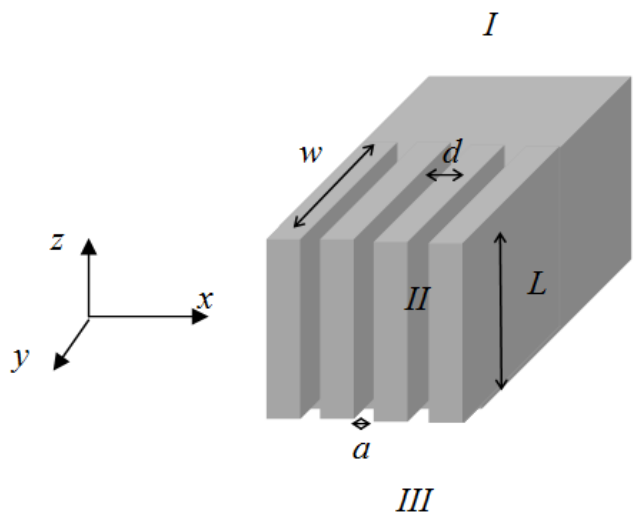

Figure 3.8.1: Three-dimensional model of a metallic metamaterial structure with side wall.

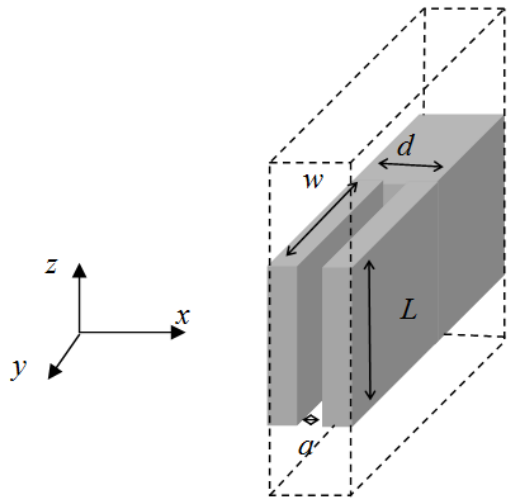

Figure 3.8.2: Schematic view of unit cell of metamaterial structure with side wall.

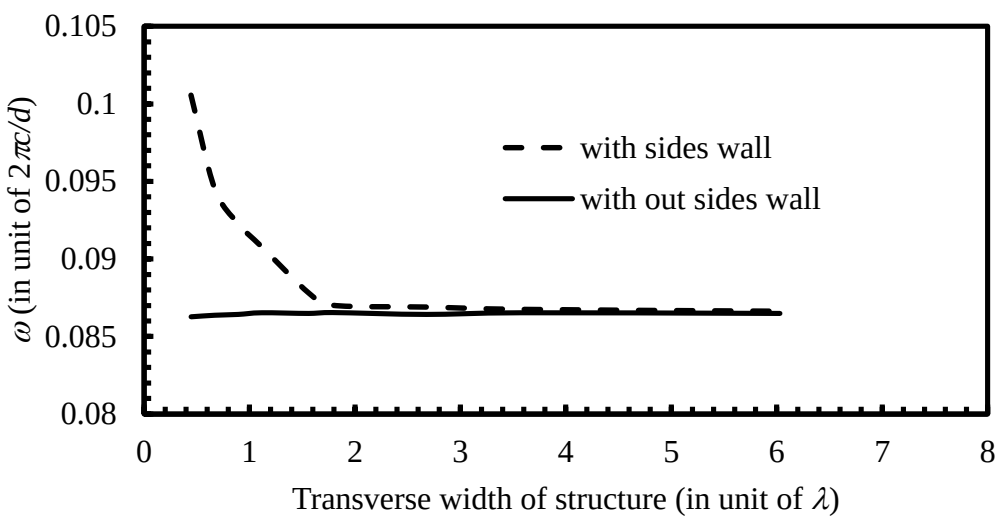

Figure 3.8.3: Eigen frequency vs transverse width of structure with side wall (dotted line) and without side wall (solid line).

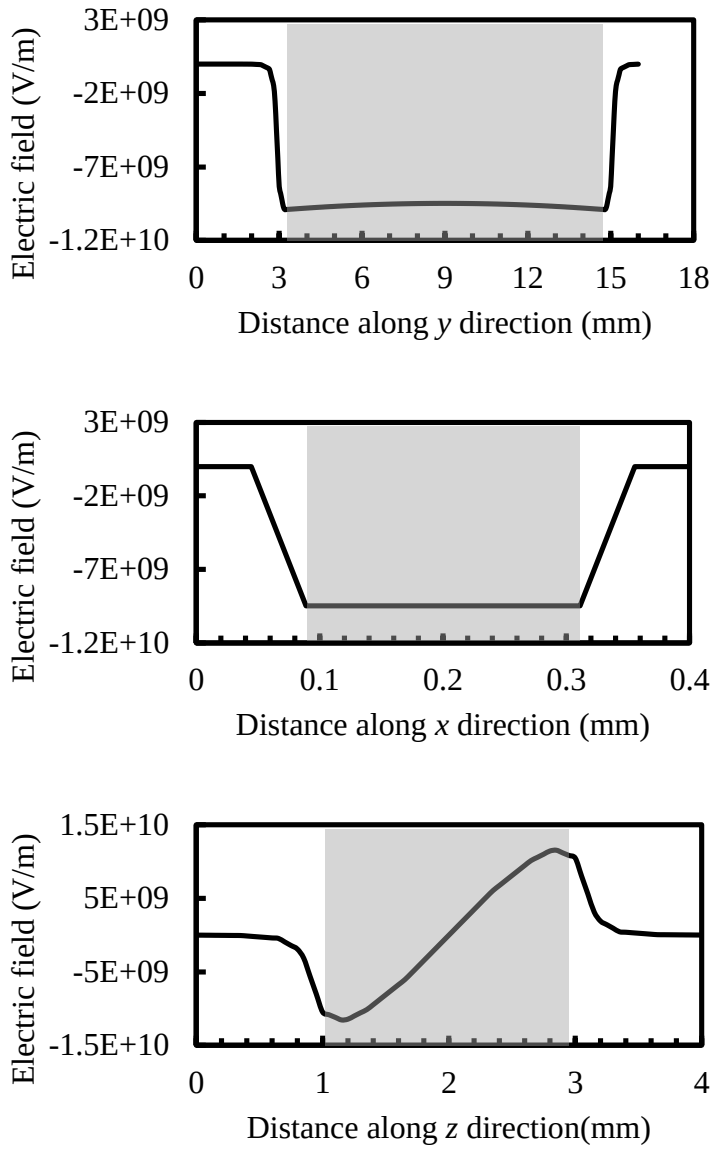

Figure 3.8.4: Variation of electric field (E_x) without side wall of metal slit, (a) along *y*, (b) along *x*, and (c) along *z*, of the structure and shaded regions indicate the regions inside the slit.

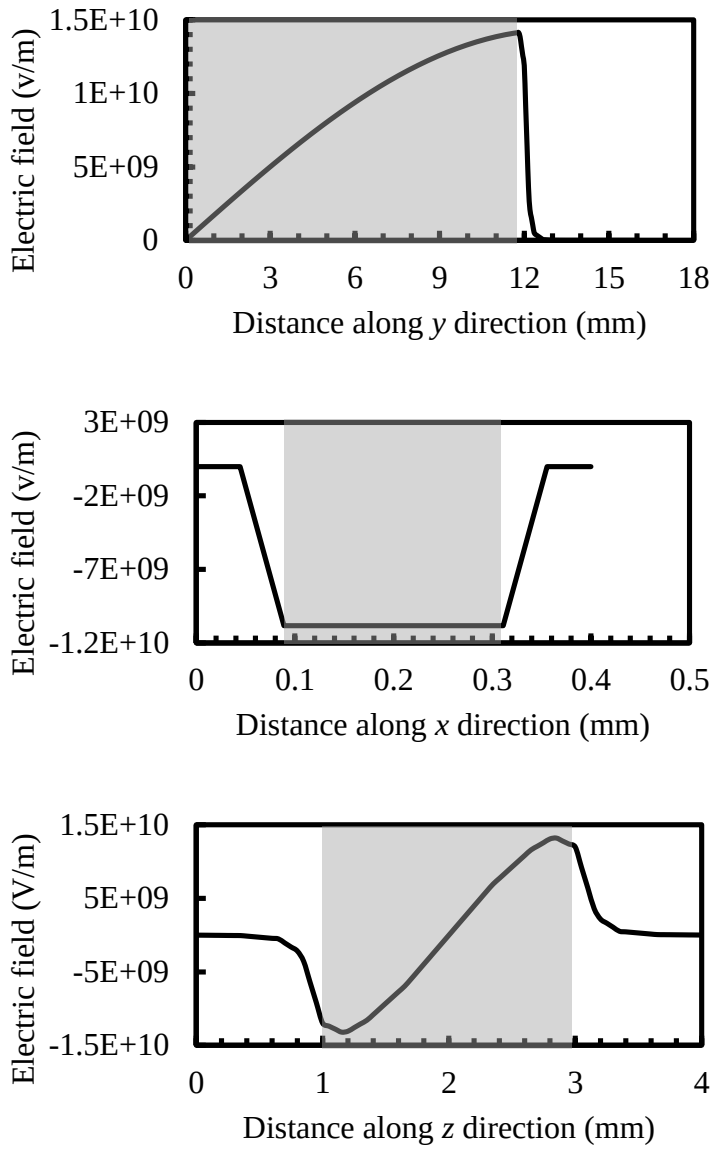

Figure 3.8.5: Variation of electric field (E_x) with side wall of metal slit, (a) along *y* (b) along *x* and (c) along *z*, shaded regions indicate the regions inside the slit.

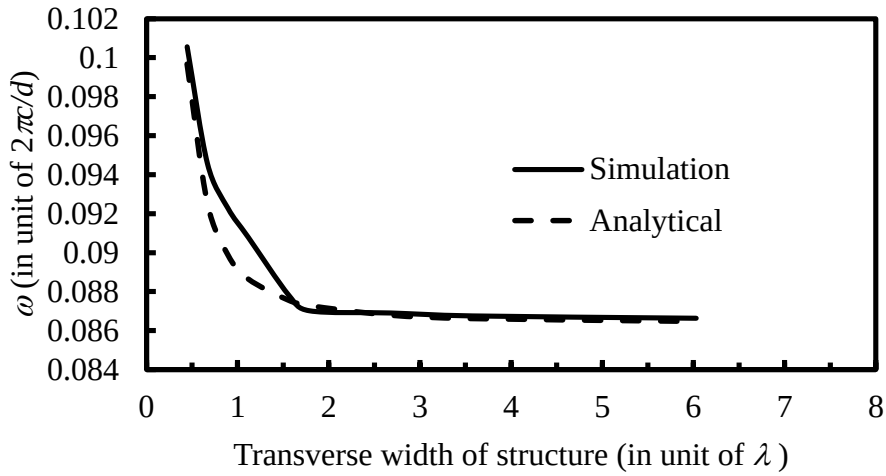

Figure 3.8.6: Comparison between simulated (solid line) and analytical (broken line) eigen modes with frequency, taking transverse widthas the parameter (solid line for simulated result and broken line for analytical result).

CHAPTER 4

Cerenkov-like Radiation in Metallic Metamaterial

4.1 Introduction

4.2 Response of Metallic Metamaterial to Convection Electron

4.3 Potential Use of Metamaterial in a Wake-Field Accelerator

4.3.1 Introduction

4.3.2 Metallic Metamaterial Wakefield Accelerator

4.1 Introduction

Cerenkov radiation (CR) [1], an electromagnetic (EM) radiation, is occurred when a charged particle passes through a medium at a velocity larger than the speed of light in that medium. This radiation is usually generated in free-electron-lasers (FELs) and wakefield accelerators [2],[21],[109-111]. However the selection of appropriate material to support Cerenkov radiation is limited due to thermal issues [111] and dielectric breakdown [47]. In addition, there is a requirement of threshold energy of moving electron to generate CR and this threshold energy [2] is decided by the refractive index of supporting dielectric material. Therefore, some alternate strategies are needed to tune the dielectric properties of the supporting materials. Metallic metamaterials are preferred over their dielectric counterparts from the standpoint of thermal and breakdown issues. A class of metallic metamaterials consisting of a one-dimensional array of periodic cut-through sub wavelength slits perforated on a metallic slab (figure 4.1.1), is known to exhibit a positive dielectric response [46],[44-45],[98]; study carried out here has demonstrated their potential as a promising platform to generate CR. In addition, such metamaterials allow the generation of CR without a kinetic energy threshold which is not observed in ordinary dielectrics.

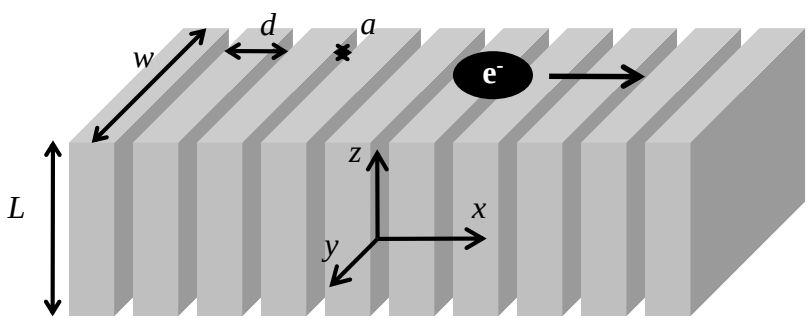

Figure 4.1.1: Schematic view of cut-through metal slits (metallic metamaterial) with convection electron bunch.

4.2 Response of Metallic Metamaterial to Convection Electron

The particle-in-cell (PIC) code [106] is used to analyze a metallic metamaterial structure (figure 4.1.1) in close proximity to a moving electron bunch in x direction. The typical structure dimensions are: $d/a = 4, L/d = 10$ and $w/d = 40$, where d and a are the axial sub wavelength periodicity and the width of the slits, respectively. h and w are the thickness and the width of the metal slab, respectively. Using the parameters, and corresponding to the value of the simulated refractive index of the equivalent dielectric of the metallic metamaterial, one can get $n = 4$ [46]. The boundaries of the sample is set as perfect absorbing boundary and a Gaussian electron bunch is modeled to pass above the structure with a pulse width of σ/d =1/4. The simulation model is shown in figure 4.2.1. The electron bunch accompanies EM fields inside slits as it travels down the structure, as depicted in figure 4.2.2, which forms a Cerenkov-like radiation cone. However, its exact dependence on electron's energy does not follow the one for normal isotropic dielectric medium, $\cos\theta = 1/n(\omega)\beta$, [2] where θ is the angle formed by the particle velocity $\vec{v}$ and the wave vector of the CR. $n(\omega)$ is the refractive index corresponding to the frequency, ω. However, propagation of radiated field occurs only in the vertical direction inside each slit with the velocity of light (c) and the electron bunch passes above the structure with the velocity βc. The radiation angle in metallic metamaterials follow the relation, $\tan\theta = v_{beam}/c = \beta$, similar to an effective anisotropic dielectric medium [112] as shown in figure 4.2.2.

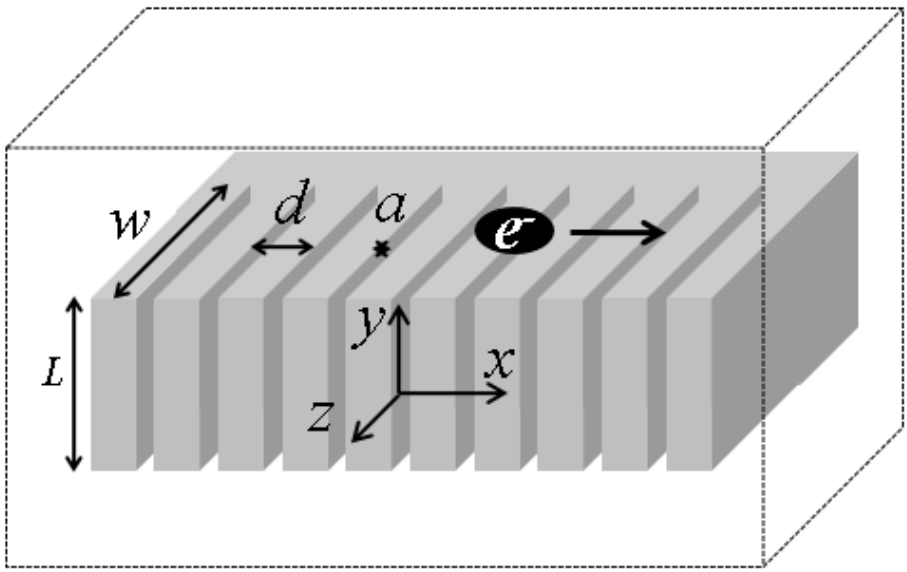

Figure 4.2.1: Model to study the interaction between metallic metamaterial and electron. (The planes, bounded by dotted lines represent the perfect absorbing boundaries of solution volume and, are far from structure surface)

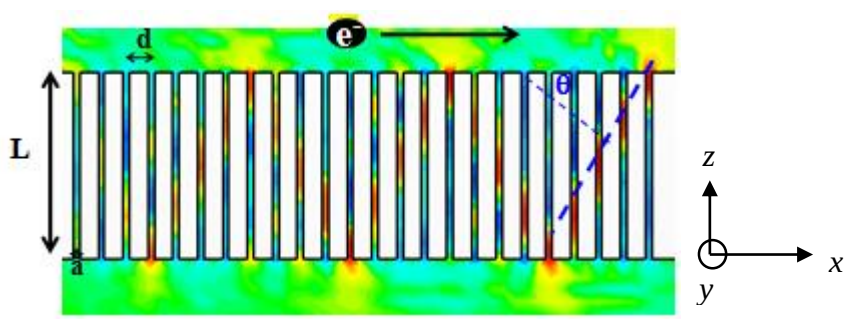

Figure 4.2.2: Contour plot of E_x taken on z-x plane at $y = 0$, corresponding to velocity $0.5c$, and the radiation angle obtained is 26.56° (The red color indicates the radiated wave-front inside structure.

Therefore, in contrast to the isotropic dielectric case, there is no velocity threshold in metallic metamaterials and its effective anisotropic dielectric medium [112] for CR. These phenomenon can be explained from the well-known kinematic relation for CR in anisotropic dielectric medium, $cos\theta = 1/n_j(\omega, \vec{k}/k)$, where $n_j(\omega, \vec{k}/k)$ denotes the refractive index for ordinary and extraordinary-waves [2],[21]. If a wave travels inside a uniaxial crystal with angle θ with respect to the ordinary axis, it gives an index ellipse of form [103]

$$\frac{\mu}{n^2(\theta)} = \frac{cos^2\theta}{\varepsilon_o} + \frac{sin^2\theta}{\varepsilon_e} \tag{4.2.1}$$

With uni-axial assumption

$$\varepsilon_x = \frac{d}{a} = \varepsilon_e \tag{4.2.2}$$

$$\varepsilon_y = \infty = \varepsilon_o \tag{4.2.3}$$

$$\mu_z = a/d \tag{4.2.4}$$

$$\mu_x = \mu_y = \mu = \text{isotropic permeability} \tag{4.2.5}$$

One can obtain from (4.2.1) through (4.2.2) to (4.2.5) as:

$$n_e(\theta) = \frac{1}{sin\theta} \tag{4.2.6}$$

The kinematic relation for CR in anisotropic dielectric medium is

$$cos\theta = \frac{1}{n_j(\omega, \vec{k}/k)\beta} \tag{4.2.7}$$

Substituting the value of refractive index *n* from equation (4.2.6) into equation (4.2.7) then the kinametics relation for CR in anisotropic dielectric is obtained as

$$tan\theta = \beta \tag{4.2.8}$$

The energy of the electron bunch is varied to verify the well-known dependence of CR on particle's velocity, such as, the angle of radiation cone. No radiation is generated for the

electron energy less than 16.8 keV when the refractive index of isotropic dielectric is equal to 4 as shown in figure 4.2.3. However, in contrast, there is no energy threshold for the metallic metamaterial structure.

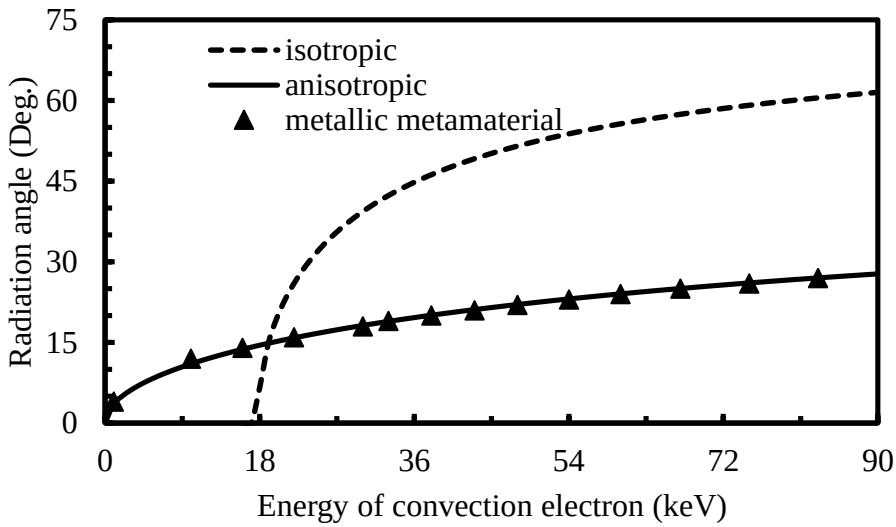

Figure 4.2.3: Comparison between radiation angles and effective dielectric media taking beam energy as the parameter (The threshold energy for Cerenkov radiation in an isotropic dielectric with refractive index 4 is 16.8keV and no energy threshold for metallic metamaterial and anisotropic dielectric).

Moreover, the threshold free CR in metallic metamaterial with the radiated electric field inside the metal slit structure for different energy of electron has also been numerically analyzed. The radiated electric field contour obtained inside the metamaterial has been compared with those electric fields obtained inside of both anisotropic and isotropic dielectrics. In this study, the refractive index of isotropic dielectric is set as 4 in all directions. The value of refractive index of anisotropic dielectric is set to 4 along the electron moving direction whereas in other directions it is set to very high value to simulate anisotropic behavior. The dimensions of anisotropic dielectric, metallic metamaterial and isotropic dielectric are same in all three directions.

The threshold energy to generate Cerenkov wakes in an isotropic dielectric with refractive index 4 is 16.8keV and therefore the convection electron with energy more than 16.8keV

generates CR inside an isotropic dielectric (figure. 4.2.4(a)). CR is also generated in metamaterial and anisotropic dielectric by convection electron with energy more than 16.8keV (figure 4.2.4(b) and figure 4.2.4(c)), however, the angle of radiation is different from that in case of isotropic dielectric. When the electron energy is lower than the threshold, Cerenkov radiation will not be observed in the isotropic dielectric (figure 4.2.5(a)). However, in metallic metamaterial and anisotropic dielectrics Cerenkov-like radiation can still be observed even with electrons having less than the threshold energy, say 10keV (figure 4.2.5(b) and figure 4.2.5(c)).

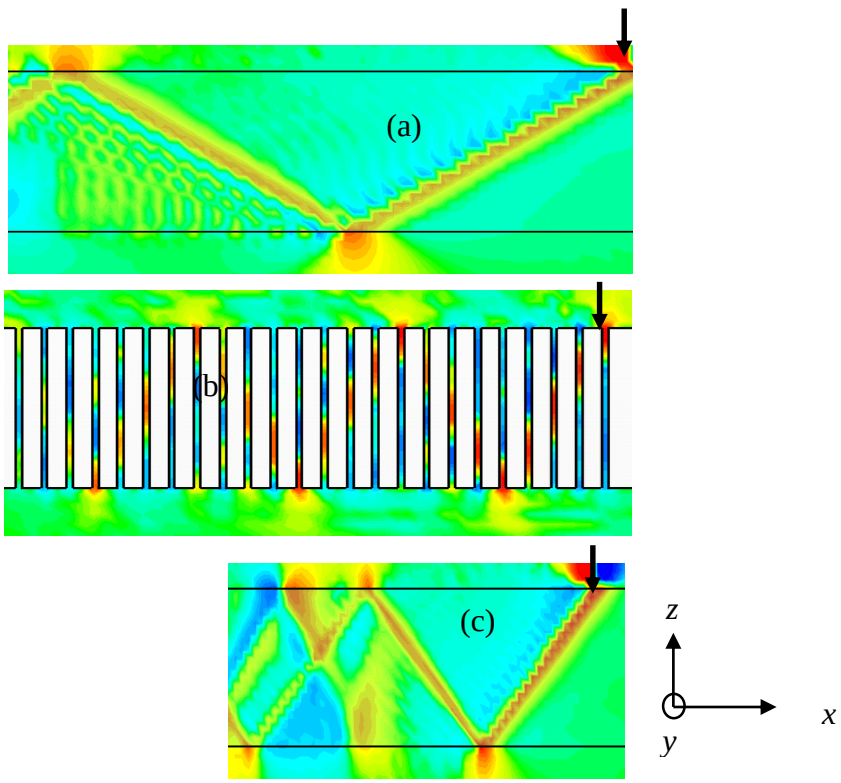

Figure4.2.4: Contour plot of E_x corresponding to electron bunch energy 80keV in, (a) isotropic dielectric (refractive index 4), (b) metamaterial structure(d/a = 4) and (c) anisotropic dielectric(refractive index 4), along x (black arrows on each figure denote the moving bunch locations and all three structures radiations are observed by the electron bunch itself).

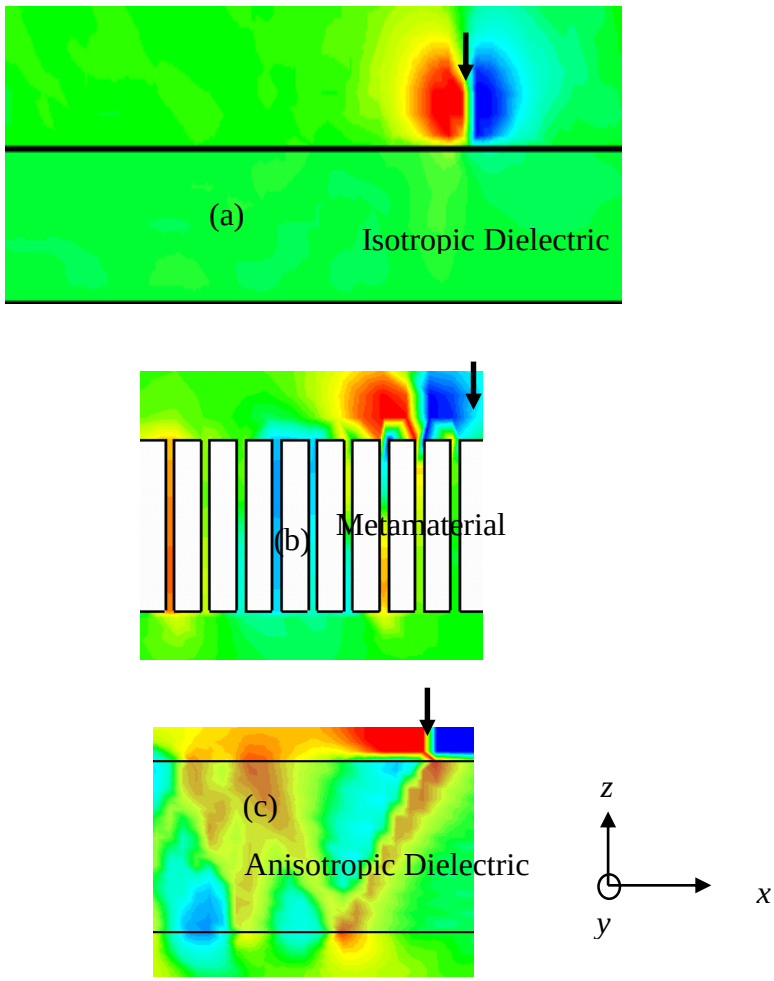

Figure 4.2.5: Contour plot of E_x (for electron bunch energy 10keV) in, (a) isotropic dielectric (refractive index 4), (b) metamaterial structure (d/a = 4), and (c) anisotropic dielectric (refractive index 4), along x direction and very high in other directions.

As mentioned above, when an electron bunch passes near the surface of the metamaterial slab (figure 4.1.1), CR is generated, as can be appreciated by an anisotropic description of the metamaterial [44]. However, the finite thickness of the metamaterial slab enforces the generated CR such that it is resonantly excited in the structure at frequencies where the guided-mode and the beam-mode phase velocities become synchronous.

In order to appreciate the excitation of the guided modes by generated Cerenkov-like radiation, a metamaterial structure is modeled and analyzed using a numerical code for the guided-mode dispersion characteristics. The structure (figure 4.1.1) response is analyzed in

close proximity to a moving electron bunch in *x* direction with typical energy corresponding to normalized velocity of $\beta(v/c) = 0.5$. The behavior of the metamaterial structure with respect to the dispersion characteristics would correspond to the guided modes lying in the shaded region bounded by $\pm c$-light-line, referring to the non-radiating regime (figure 4.2.6). At these points of intersection between the electron beam-mode dispersion line and the guided-mode dispersion characteristics [9] (figure 4.2.6), the fast Fourier transform (FFT) spectrum of metamaterial slab shows (figure 4.2.7), the amplitude peaks of the axial component of the electric field (E_x) inside the slits. However, there were no such peaks typically beyond a limiting normalized frequency $\omega(= 2\pi c/d) = 0.32$. The absence of the peaks can be attributed to the Smith-Purcell diffraction radiation [16] from the metamaterial slab. In contrast, such a FFT response of metamaterial slab far from and transverse to the structure and the electron bunch exhibits no such discernible peaks below the limiting frequency (figure 4.2.7). Moreover, the behavior of this metamaterial structure, below this limiting frequency with respect to the absence of energy radiating out of the structure, may also be correlated with the simulated electric field pattern that shows the confinement of the field on both the up and down surfaces of the metamaterial slab (figure 4.2.4(b)). In addition, there would be no power flow along the metal slab surface along *x* owing to the flatness of the guided-mode dispersion plot, which corresponds to the near-zero group velocity ($\partial\omega/\partial k_x \to 0$), k_x being the wave-vector (wave momentum) along *x* at the points of intersection between the guided-mode and the beam-mode dispersion plots (figure 4.2.6).

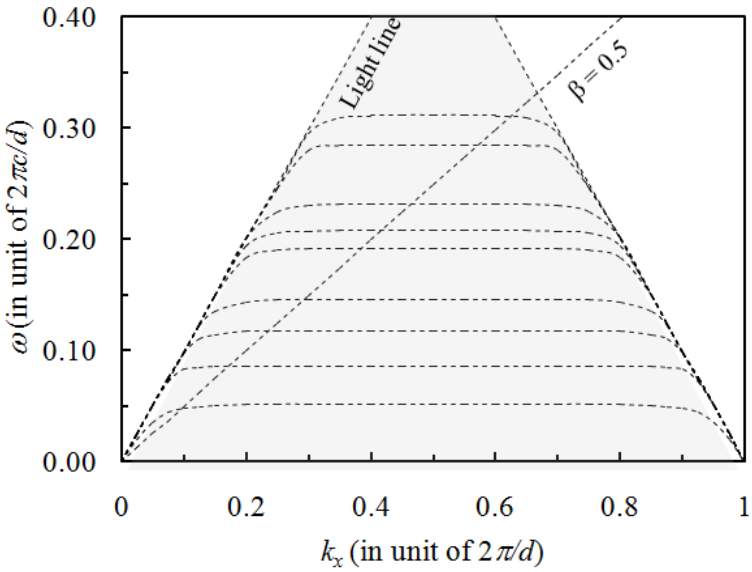

Figure 4.2.6: Guided-mode dispersion characteristics of metallic metamaterial with a typical beam-mode dispersion line $\beta(=v/c)=0.5$, the shaded and white regions indicating the non-radiating and radiating regimes respectively.

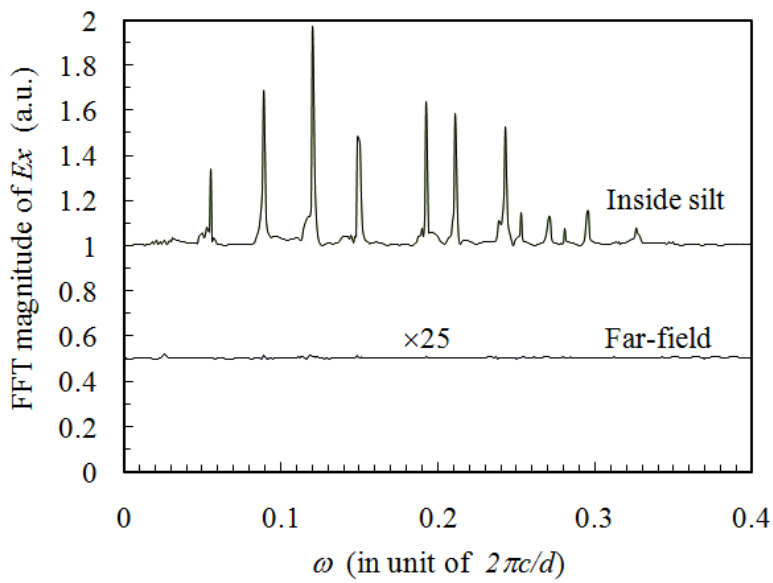

Figure 4.2.7: Inside-slit and far-field (magnified 25 times) FFT spectrum of the E_x field of metallic metamaterial with normalized frequency.

Moreover, to verify the existence of the guided modes, the metamaterial slab thickness, *L/d*, is varied from 1 to 10 and the corresponding excited guided modes frequencies are plotted in figure 4.2.8. As the thickness increases, more resonantly excited states appear due to generation of higher order modes. Furthermore, the absence of resonances above the frequency of 0.32 is due to appearance of Smith–Purcell radiation.

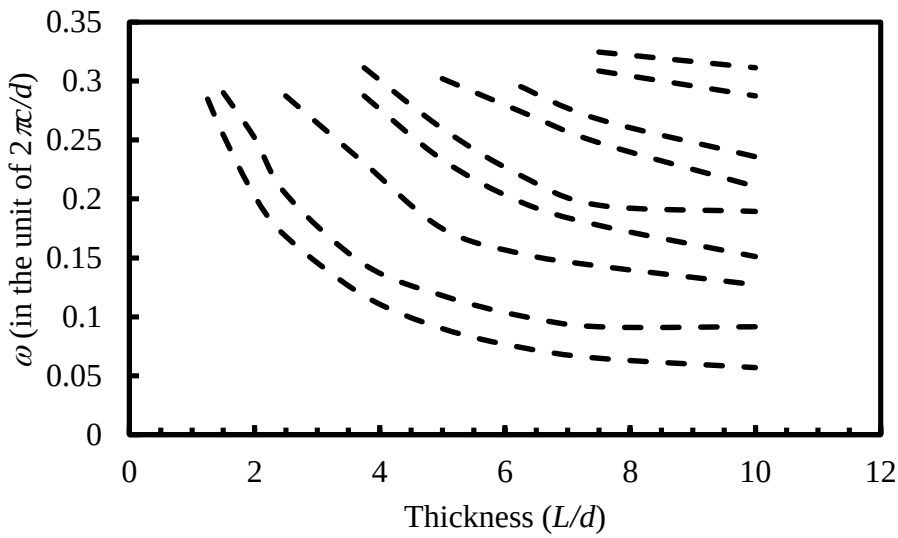

Figure 4.2.8: Effect of slab thickness on excited mode frequency keeping other parameters constant.

4.3 Potential Use of Metamaterial in Wake Field Accelarator

4.3.1 Introduction

A wakefield accelerator is a device which employs large amplitude electric fields generated in the wake of an intense particle beam to accelerate other trailing charged particles to high energy [113]. The supporting medium to generate this wakefield from convection electron can be of that types which can support the propagation of slow waves ($\upsilon_\varphi < c$). The prominent examples of such medium are plasma, dielectric-lined wave guide, or a standard disk-loaded linac structure. In addition, the accelerating beam axis may also be either collinear or parallel to the driving beam. The typical application considered for this type of linear accelerator is a future linear collider. There are two major advantages of wakefield accelerator over the conventional cavity based accelerator. The first advantage is that there is no need of any external RF drive source for wakefield accelerator and second one is in case of wakefield accelerator, a high field gradient can be achieved for acceleration [114-116].

In the conventional dielectric wakefield accelerator, an electron bunch of high charge number (i.e. the ‘‘driving bunch’’) is injected into a dielectric-lined cylindrical waveguide [22],[25,[28] with a velocity greater than the phase velocity of RF in that dielectric medium. The wakefield with longitudanal electric fields is induced in dielectric-lined cylindrical waveguide by driving bunch because of Cerenkov radiation. The wakefield that fills the waveguide behind the driving bunch can be used to accelarate a ‘‘test’’ bunch of low charge number. The test bunch with low charge number will move in synchronism with the wake fields and can be accelarated if it is injected at a suitable interval after the driving bunch[22],[25,[28]. Though the cylindrical dielectric is able to produce large axial wakefiled and it is simple to fabricate, it has several limitations like high transverse wakefield which causes beam break-up instability [117], scaling at high frequency operation [25],[28], dielectric breakdown at high field [47] and generation of large static electric field [117]. The generation of large static electric field results in deflection of subsequent bunches leading to evantual loss of the beam [118].

The use of planar structures for advanced accelerator applications has been discussed [42-43],[118] by several research group. This type of electromagnetic structure may have advantages over the usual waveguide structure, in ease of external power coupling and lowered space-charge forces. In addition to that, more importantly, if the transverse dimension of structure is very large, the transverse wakefields associated with this class of structure are mitigated [42], [119] thus diminishing the beam breakup (BBU) instability [117] which typically limits the beam current in short-wavelength accelerators. However, this type of structure is also sufferers from energy threshold for radiation, dielectric breakdown, thermal issues and generation of static electric field. Therefore, it is desirable to find an alternative structure for wakefield accelarator to overcome these limitations. As metal has better thermal conductivity than that of dielectric and therefore former would be preferable to overcome two above mentioned limitations.

4.3.2 Metallic Metamaterial Wakefield Accelarator

The metallic metamaterial would be better alternative structure for wakefield accelarator because of pure metallic structure with tunable refractive index. This metamaterial supports energy threshold free Cerenkov radiation and it offers orbitarily high refractive index which is not available in nature. Because of these two above properties, this metamaterial supports low voltage operation of accelarator in addition to infinite or very high brekdown limit and zero or very low static field generation on structure. The typical application considered for this type of structure is a future linear wake field accelerator, and therefore particular attention is paid to such issues as higher accelerating longitudinal field gradient and lower transverse field gradient to improve single and multiple bunch stability.

Two types of structures, one with two parallel slabs of dielectric separated by a small vacuum gap (figure 4.3.1) and other with two parallel slabs of metallic metamaterial (figure 4.3.2), are analyzed for both longitudanal and transverse wake fields. The overall dimensions (both longitudanal and transverse) and vacuum gap dimensions are identical for all structures. The refractive index for both dielectric slab and metamaterial slab ($n = d/a$) is set as 2. The outer surfaces of the dielectric slabs are sheathed in a lossless conductor. Then a Gaussian electron bunch with charge 5exp-12C and pulse width $\sigma = 0.5d$ is allowed to pass though the center of the vacuum gap of two structures. Figure 4.3.3(a) and figure 4.3.3(b) show the wake

field generated by ‘driving charge’ in dielectric slab-symmetric and metamaterial slab-symmetric structures.

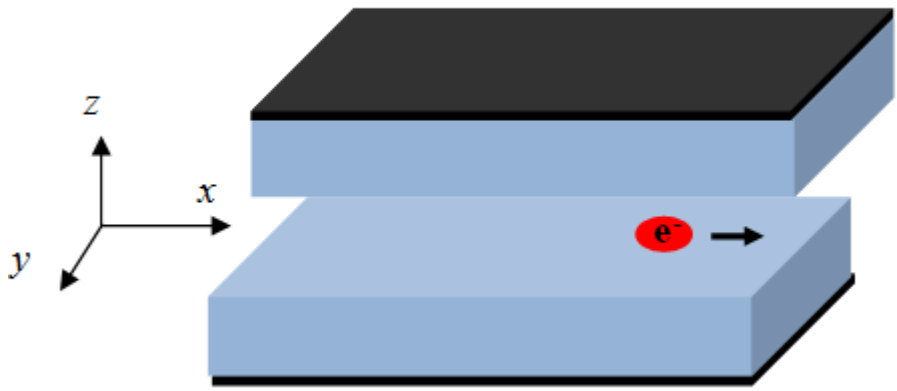

Figure 4.3.1: Schemetic of slab-symmetric dielectric waveguide and electron bunch passes through along the axis (black parts are the metallic coating on dielectric slab).

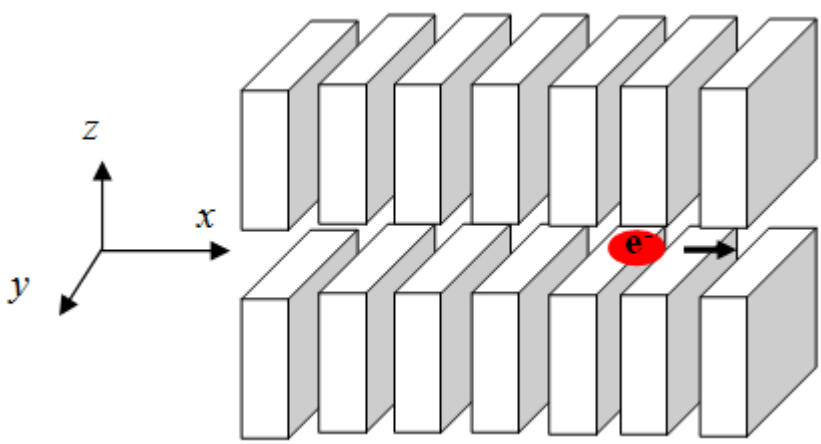

Figure 4.3.2: Schemetic of slab-symmetric metallic metamaterial waveguide and electron bunch when electron bunch passes through the axis of structure.

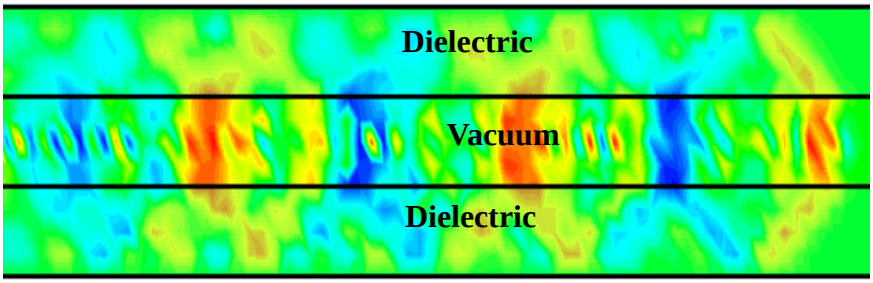

(a)

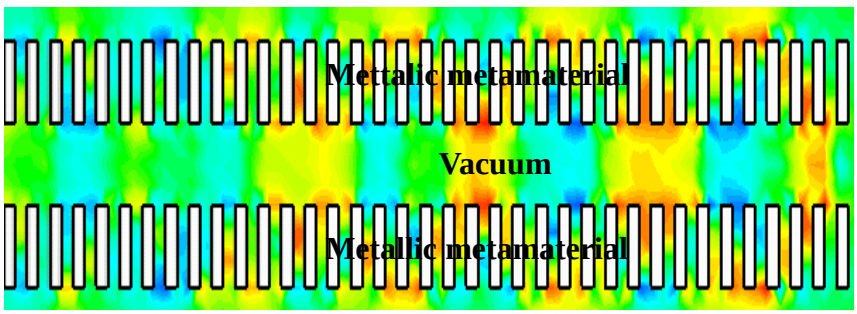

(b)

Figure 4.3.3: Contour of axial wake field (E_x), on x-z plane (y = 0), induced by electron bunch in (a) dielectric slab-symetric and (b) metallic metamaterial slab-symmetric waveguide.

Next, the longitudanal and transverse wake potentials are analyzed for this two types of structures. The combined effect of the wakefields of a driving charge on a trailing test particle, as both particles pass through a structure, is usually of great interest than the details of the wakefields themselves. The integrated fields seen by a test particle, traveling along the same or parallel paths at a constant distance behind driving charges, are the longitudinal (W_x) and transverse (W_y and W_z) wake potentials [120-121]. The longitudinal and transverse momentum kick experienced by a test charge is poportional to the corresponding wake potential ($\Delta P = -(eq/c)W$). Therefore, in case of wakefield accelarator, higher longitudanal wake potential and and lower transverse wake potential are desirable. Figure 4.3.4(a), figure 4.3.4(b) and 4.3.4(c) show the comparison of longitudinal (along x) and transverse wake potential (along y and z) for dielectric slab-symmetric and metamaterial slab-symmetric structure respectively.

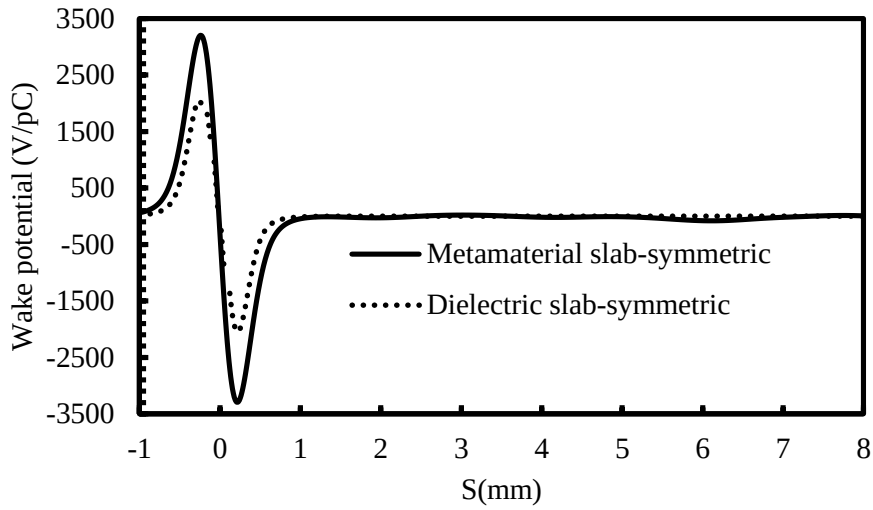
3500
2500
1500
500
-500
-1500
-2500
-3500
Wake potential (V/pC)
-1
0
1
2
3
4
5
6
7
8
S(mm)
Metamaterial slab-symmetric
Dielectric slab-symmetric

(a)

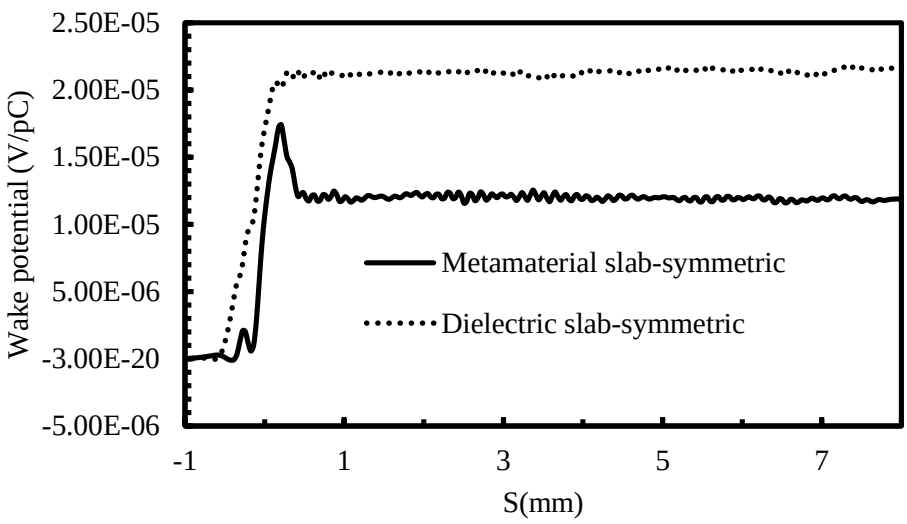
2.50E-05
2.00E-05
1.50E-05
1.00E-05
5.00E-06
-3.00E-20
-5.00E-06
Wake potential (V/pC)
-1
1
3
5
7
S(mm)
Metamaterial slab-symmetric
Dielectric slab-symmetric

(b)

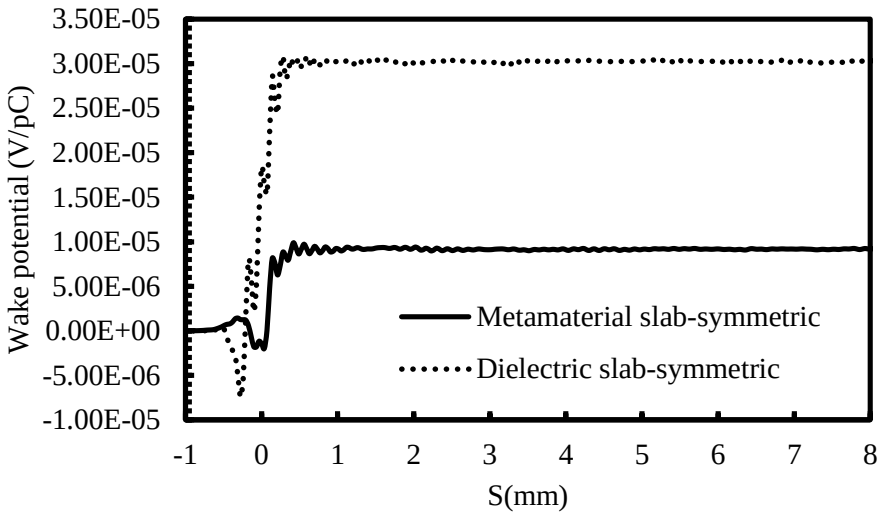

(c)

Figure 4.3.4: Comparison of (a) longitudanal, (b) transverse (along '*y*') wake potentials and (c) transverse (along '*z*') wake potentials, for dielectric slab-symmetric and metamaterial slab-symmetic structures.

The wake potentials are calculated by integrating the electromagnetic force along the respective axes and the wake potentials are the energy variation induced by the wakefields of the lead particle on a unit charge test particle. It is observed from figures 4.3.4(a), 4.3.4(b) and 4.3.4(c), that the longitudanal wake potential is higher in case of metallic metamaterial slab than that of the dielectric slab, and transverse wake potetential is lower in case of metamateial slab than that of the dielectric slab. Due to the three major advantages of metamaterial slab-symmetric structure over its dielectric counter part, better heat dissipation capability, very high breakdown strength and energy threshold free operation, this structure would be better spporting structure for future wakefield accelarator.

CHAPTER 5

Out-Coupling of Cerenkov-like Radiation via Brillouin-Zone Folding

5.1 Introduction

5.2 Brillouin-Zone Folding Mechanism

5.3 Brillouin-Zone Folding of a Metallic Metamaterial

5.4 Out-coupling of Cerenkov-like Radiation via Brillouin-zone Folding

5.5 Metallic Metamaterial as an Interaction Structure of a High-Frequency Electromagnetic Wave Generator

5.1 Introduction

Finite thickness of metallic metamaterial slab enforces the generated CR (discussed in preceding chapter) to excite resonantly in the structure at frequencies where both the guided-mode and the beam-mode phase velocities are synchronous. The out-coupling from metallic metamaterial is limited by two reasons; 1) due to the behavior of metallic metamaterial structure with respect to dispersion characteristics correspond to the guided modes lying in the region bounded by '*c*' line (*c* is the velocity of light), referring to the non-radiating regime. 2) There would not be any power flow in the axial direction along the slab surface due to flatness of the guided-mode dispersion plot, which corresponds to the near-zero group velocity ($\partial\omega/\partial k_x \rightarrow 0$), k_x being the wave-vector (wave momentum) along axial direction at the points of intersection between the guided-mode and the beam-mode dispersion plots. Therefore, edge coupling [28], [25] of generated CR as in case of ordinary dielectric slabs, is not applicable to metallic metamaterial slab due to the near-zero group velocity of radiation in the axial direction. However, the out-coupling of Cerenkov-like radiation from the top and bottom surfaces of the structure in the transverse direction is possible by modifying the structure itself. This modification of structure stems from the well-known concept of the Brillouin-zone folding phenomenon in the superlattice-based photonic crystal, arising out of the reduction of the size of the first Brillouin-zone of the guided mode dispersion diagram, caused by the introduction of the additional periodicity due to the larger size of the unit cell and the reduced symmetry of the crystal [122-126].

Moreover, the intensity of the surface-coupled radiation by this mechanism shows an order-of-magnitude enhancement compared to that of ordinary Smith-Purcell radiation [127-128] in case of reflection grating.

5.2 Brillouin-Zone Folding Mechanism

The concept of a Brillouin-zone, defined as a Wigner-Seitz primitive cell in the reciprocal lattice, was first developed by Léon Brillouin (1889-1969), [129-130]. The first Brillouin-zone is the smallest volume entirely enclosed by planes that are the perpendicular bisectors of the reciprocal lattice vectors drawn from the origin. There are also second, third, etc., Brillouin-zones, corresponding to a sequence of disjoint regions at increasing distances from the origin, but these are used more rarely. As a result, the first Brillouin-zone is often called simply the Brillouin-zone.

In this section construction mechanism of a one-dimensional lattice is discussed. The considered one-dimensional lattice with direct lattice translational vector $\vec{J} = \vec{m}$, where $\vec{m}$ is the only basis vector of the direct lattice, is shown in figure 5.2.1.

Figure 5.2.1: Schematic view of one-dimensional lattice with lattice basis vector $\vec{m}$

Every crystal structure has two lattices associated with it, the crystal lattice and the reciprocal lattice [11]. The reciprocal lattice of a lattice (usually a Bravais lattice) is the lattice in which the Fourier transform of the spatial wave function of the original lattice (or direct lattice) is represented. This space is also known as momentum space or *k*-space, due to the relationship between the Pontryagin duals momentum and position. In case of one-dimensional crystal, if $\vec{m}$ is the only basis vector of the real lattice, and $\vec{A}$ is the only basis vector of the reciprocal lattice, then they are related as [130]:

$$\vec{m} \cdot \vec{A} = 2\pi \tag{5.2.1}$$

The reciprocal lattice for a one-dimensional direct lattice is also a one-dimensional lattice as shown in figure 5.2.2.

The first Brillouin-zone of this one-dimensional lattice (figure 5.2.1) is specified by two normal that bisect $\vec{A}$ on both sides of the origin at the points M and N (figure5.2.2) and it gives a vivid geometrical interpretation of the diffraction condition as giving by following equation

$$2\vec{k} \cdot \vec{A} = A^2 \tag{5.2.2}$$

So,

$$k = \pm\pi/m', \tag{5.2.3}$$

where m' is the lattice constant.

Thus the Brillouin-zone of a one-dimensional linear lattice is specified by the two points $k = \pm\pi/m'$ as shown in figure 5.2.2.

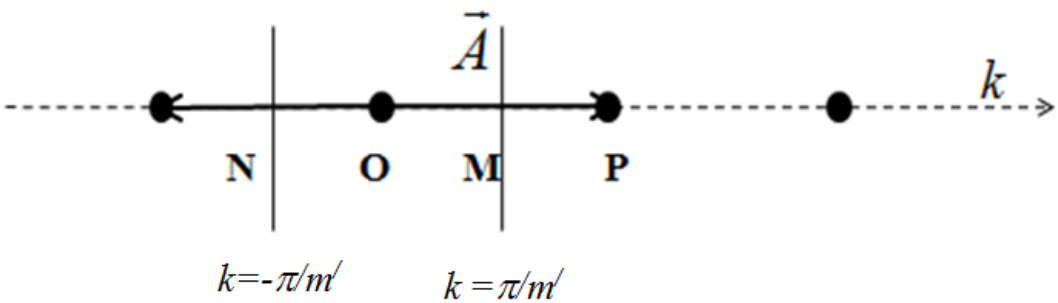

Figure 5.2.2: Schematic view of reciprocal lattice and first Brillouin-zone of a one-dimensional lattice with lattice vector $\vec{m}$. ($\vec{A}$ is the basis vector of reciprocal lattice).

Superlattice is a periodic structure of two (or more) periodicity or layers of two (or more) materials. Kronig-Penney model is the most commonly used method to analyze the band structure of Superlattice based crystal. Here, the band structure of a one-dimensional superlattice based structure has been discussed. A superlattice (figure 5.2.3) based on one-dimensional structure and is formed by superimposing another one-dimensional crystal with basis vector $\vec{b}$ on the one-dimensional crystal with basis vector $\vec{m}$ (figure 5.2.1).

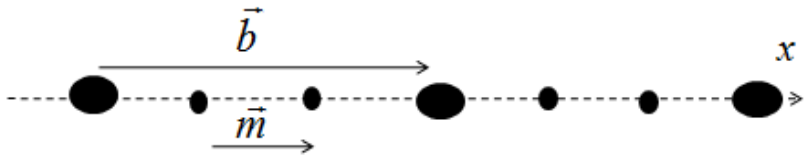

Figure 5.2.3: Schematic view of one-dimensional super-lattice.

Now, the superlattice, consisting of materials with lattice constants *m* and *b*, has a superlattice period *b* (*b*>*m*). Therefore, the first Brillouin-zone edge of such a superlattice is given by $\pm\pi/b$, indicating the larger unit cell results in a smaller Brillouin-zone. Therefore, *k*-vectors which belong to the lattice with lattice constant *m* and lie between $k = -\pi/b$, $-\pi/m'$ and $k = \pi/m'$, $k = \pi/b$ on *k* axis are translated into a domain lying between $k = \pm\pi/b$. In other words, Brillouin-zone of bulk material, $\pm\pi/m$ are folded in to smaller zone with $\pm\pi/b$ in a superlattice. As a result, many mini-bands are formed in super lattice. This is a typical feature of superlattice and is called Brillouin-zone folding effect.

5.3 Brillouin-Zone Folding of Metallic Metamaterial

A class of metallic metamaterials consisting of a one-dimensional array of periodic cut-through sub wavelength slits perforated on a metallic slab (structure-I, figure 4.2.1), is a three-dimensional structure with periodicity in one direction. This metamaterial structure can be regard as similar to a one-dimensional lattice structure with basis lattice vector $\vec{d}$ and lattice constant *d*. Therefore, the first Brillouin-zone boundary of this structure is specified by the two points $k = \pm\pi/d$. Figure 5.3.1(a) shows the front-view (two-dimensional view on *z*-*x* plane) of the metamaterial structure shown in figure 4.2.1. From figure 5.3.1(a) it is clear that this metamaterial structure can be regards as one-dimensional lattice with lattice constant *d* and lattice vector $\vec{d}$**.** Figure 5.3.1(b) and 5.3.1(c) represent the corresponding one-dimensional lattice and reciprocal lattice, respectively, along with first Brillouin-zone. The first Brillouin-zone of this metamaterial structure is bounded by two normal bisectors of reciprocal lattice vector $\vec{B}$, where $\vec{B} \cdot \vec{d} = 2\pi$, at two points M ($k = \pi/d$) and N ($k = -\pi/d$).

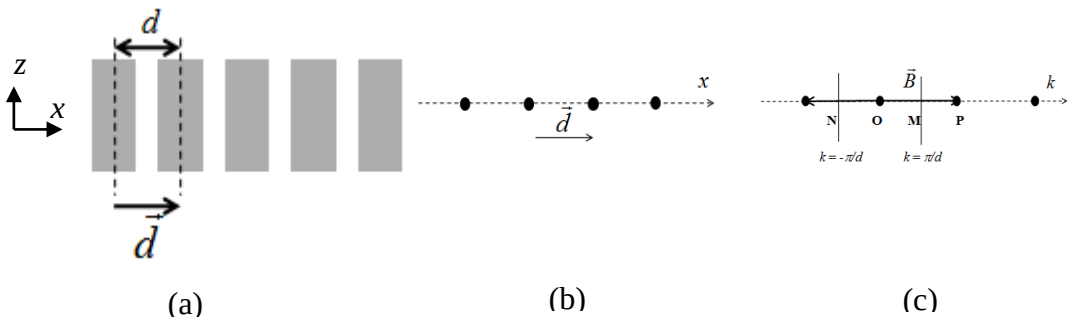

Figure 5.3.1: (a) Two-dimensional view (on *z*-*x* plane) of the metamaterial structure (structure-I), (b) equivalent one-dimensional lattice, and (c) corresponding reciprocal lattice.

Since this metamaterial structure supports a number of modes, the band diagram or dispersion diagram (Energy-momentum or frequency-wavenumber) of this structure contains a number of bands in first Brillouin-zone and can be obtained by re-plotting figure 4.2.6 up to k_x (= π/d) =0.5 and shown in figure 5.3.2.

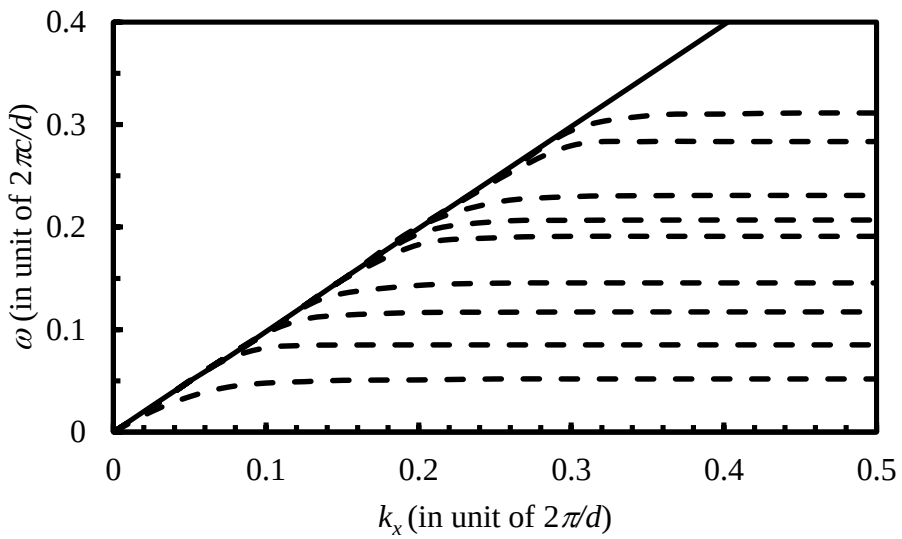

Figure 5.3.2: Dispersion diagram modes supported by the structure-I. Dashed lines indicate the dispersion and solid line indicates the vacuum light line.

Then a similar array of cut through slit with periodicity D (=4d), perforated on a perfect metal film is considered (Structure-II). The front-view (two-dimensional view on z-x plane) of these structures, corresponding to one-dimensional lattice representation and reciprocal lattice along with first Brillouin-zone, are shown in figures 5.3.3(a) to 5.3.3 (c), respectively. The first Brillouin-zone of this structure is bounded by two normal bisectors of reciprocal lattice vector $\vec{C}$, where $\vec{D} \cdot \vec{C} = 2\pi$, at two point T ($k = \pi/D$) and point Q ($k = -\pi/D$).

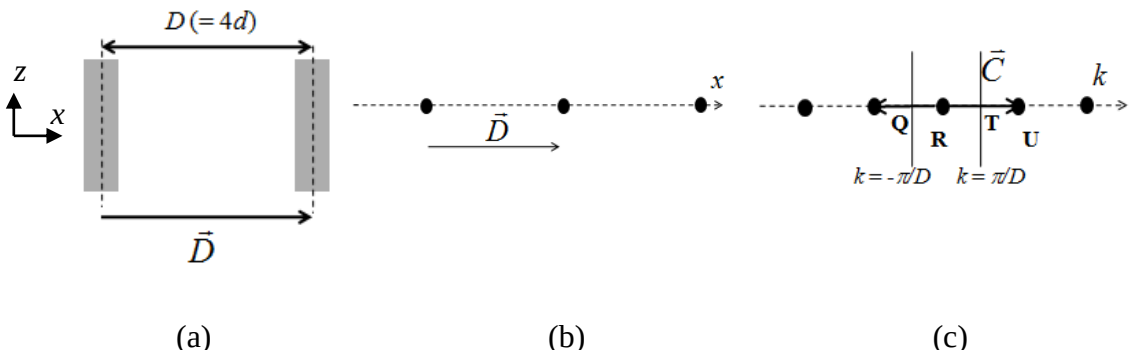

Figure 5.3.3: (a) array of cut through slit with periodicity D (=$4d$) (structure-II), perforated on a perfect metal, (b) equivalent one-dimensional lattice, (c) corresponding reciprocal lattice and first Brillouin-zone.

It is to be noted that above two considered structures-I and structure-II are similar except their periodicity. Periodicity of structure-I is smaller than that of structure-II and therefore, the structure-II has smaller first Brillouin-zone than that of structure-I. However, if the structure-II is superimposed on structure-I, then a bi-periodic structure which will have two periods in axial direction will be formed. This bi-periodic structure is similar to a superlattice-based lattice structure in which unit cell size is increased and symmetry is reduced due to introduction of additional periodicity and, hence, the size of the first Brillouin-zone is reduced [122-125]. The reduction in size of first Brillouin-zone causes the Brillouin-zone folding. Figure 5.3.4 shows the formation of superlattice by superimposing structure-II on structure-I. In this particular case, the period of structure-II is four times larger than that of structure-I, which is therefore likely to result in the folding of the guided modes at $k = \pi/D$. The reciprocal lattice representation of structure-I and that of structure-II are shown in figures 5.3.5(a) and 5.3.5(b),

respectively. The first Brillouin-zone of structure-I is bounded by $k = \pm\pi/d$ (square hatch) and that of structure-II is bounded by $k = \pm\pi/D$ (hatch). Figure5.3.5(c) shows the overlapping of two Brillouin-zone when superlattice is formed. As a consequence of different size of the structure-I Brillouin-zone and structure-II Brillouin-zone, k vectors lie outside the structure-II Brillouin-zone (hatch region) but within the Brillouin-zone of structure-I (square hatch region) are translated into structure-II Brillouin-zone. Thus, these points are folded back into structure-II Brillouin-zone, which is smaller and lower symmetric. The dispersion diagram of modes supported by the structure-I, folded mode due to introduction of additional periodicity, vacuum light line and zone folding symmetry are shown in figure 5.3.6.

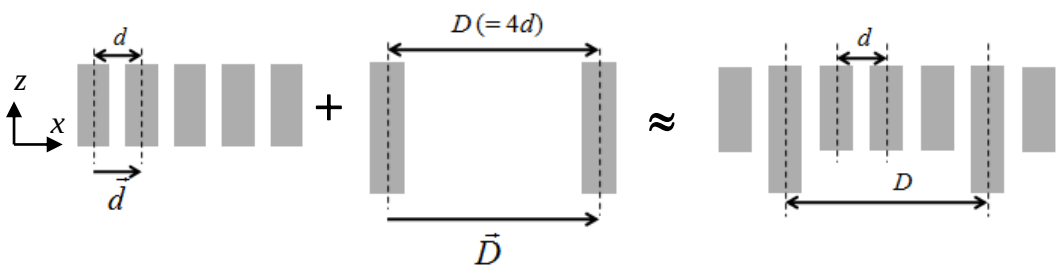

Figure 5.3.4: Detail of superlattice based structure (a) structure-I, (b) structure-II and (c) superlattice formed by superimposing structure-II on structure-I.

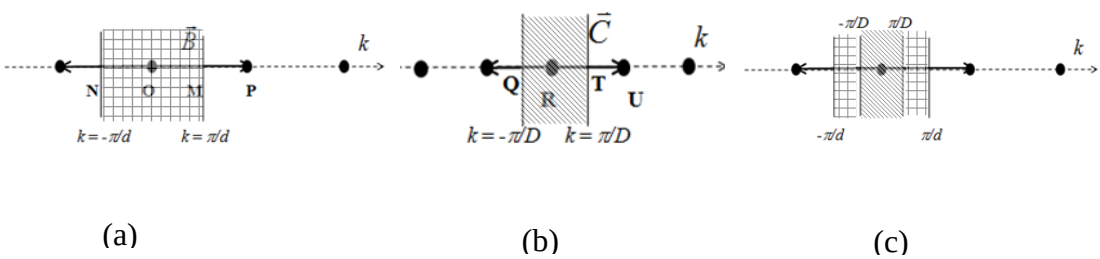

Figure 5.3.5: (a) First Brillouin-zone of structure-I, (b) first Brillouin-zone of structure-II, (c) two overlapping Brillouin-zones of superlattice.

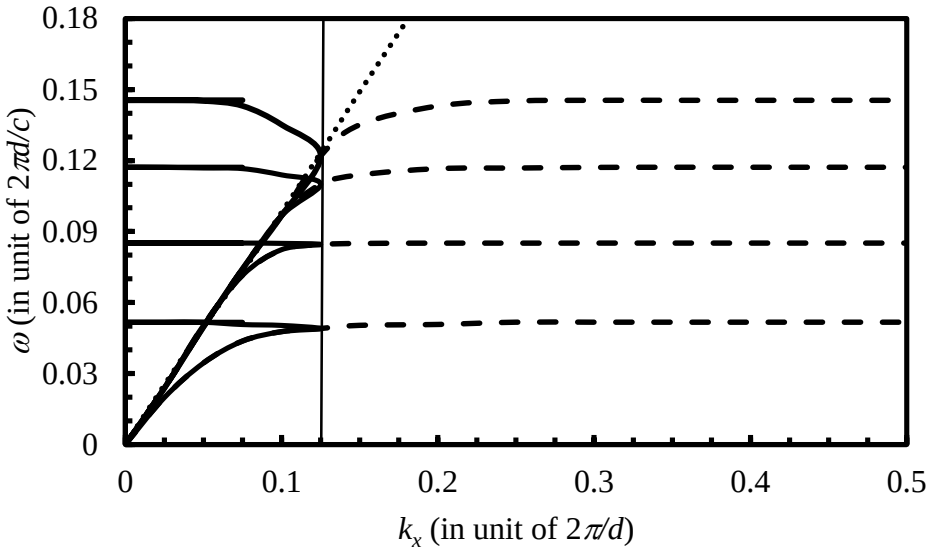

Figure 5.3.6: Dispersion diagram of modes supported by structure-I (dashed lines), folded mode (due to introduction of additional periodicity) (solid thick lines), vacuum light line (dotted line) and zone folding symmetry (vertical solid line).

5.4 Out-coupling of Cerenkov-like Radiation via Brillouin-Zone Folding

The finite thickness of the metamaterial slab enforces the generated Cerenkov-like radiation such that it is resonantly excited in the structure at frequencies where the guided-mode and the beam-mode phase velocities become synchronous (preceding chapter). It has also been discussed in preceding chapter that the limitations of metallic metamaterial structure as shown in figure 5.4.1(a), in coupling out Cerenkov-like radiation from the top and bottom surfaces of the structure in the transverse direction and from the end of structure as well. The limitation in coupling out of Cerenkov-like radiation from the top and bottom surfaces of the structure in the transverse direction will be overcome in the proposed method, shown in figure 5.4.1(b). It may be noted that the figure 5.4.1(a) and 5.4.1(b) depicts the three-dimensional views of both the structures I and II, respectively. The three-dimensional models of structure-I and structure-II are now labeled as structure-A and structure-B. The out-coupling of Cerenkov-like radiation from the top and the bottom surfaces of the structure in the transverse

direction is accomplished by modifying structure-A (figure 5.4.1(a)) as: introducing a change in the metamaterial slab thickness between L and $L + l$ periodically at a regular interval of slits, typically, here the number is four, which consequently introduces an additional periodicity ($D = 4d$) in the axial direction of the structure geometry as shown in figure 5.4.1(b) (structure-B). This suggestion stems from the well-known concept of the Brillouin-zone folding phenomenon in the superlattice-based photonic crystal arising out of the reduction of the size of the first Brillouin-zone of the guided-mode dispersion diagram caused by the introduction of the additional periodicity due to the larger size of the unit cell and the and the reduced symmetry of the crystal [122-125].

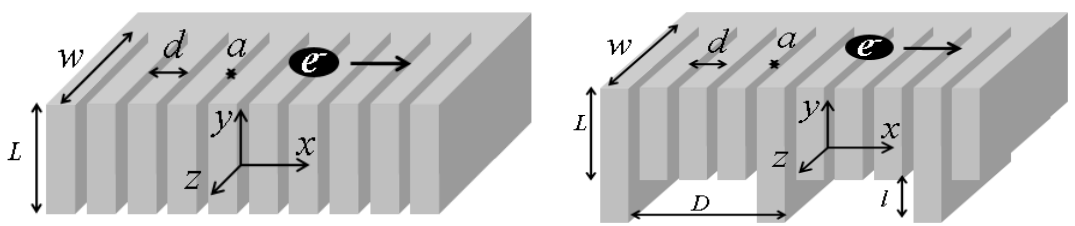

(a) (b)

Figure 5.4.1: (a) Metallic metamaterial structure consisting of a one-dimensional array of periodic cut-through slits perforated on a metallic slab (structure-A) and, (b) the proposed metamaterial structure obtained by periodically modifying the thickness of structure-A so as to provide additional periodicity (structure-B) in proximity to a moving electron bunch.

However, it is likely that some of these modes excited in structure-B would be driven into a reduced Brillouin-zone as compared to structure-A in view of the unit cell size along *x* of structure-B becoming *D/d* times larger than that of structure-A, which is therefore likely to result in the folding of the guided modes at $k_x = \pi/D$ [126]. Figure 5.4.3 shows the folded bands which are obtained by translating the guided bands of structure-A by an appropriate reciprocal lattice vector conforming to the Brillouin-zone folding effect [122-126],[131]. In the present context, the wave number (momentum) of each of the modes, lying on the positive side of the band-folding symmetry ($k_x = \pi/D$) on the momentum (k_x) scale [123],[131], is translated into negative side of the band-folding symmetry, with the guided-mode frequency

remaining unchanged as shown in figure 5.4.3. The amount of this translation is equal to the separation between the point of symmetry $k_x = \pi/D$ and the momentum of the guided mode. Typically, out of the first four guided modes of structure-B, excited by the electron bunch at the angular frequencies $\omega(= 2\pi c/d)$of 0.05, 0.085, 0.12 and 0.145, respectively, the first excited modes at $\omega(= 2\pi c/d) = 0.05$ remains in the unfolded regime. However, the remaining three remain in the folded regime with their respective momentums shifted towards band folding regime from the unfolded regime. Further, out of the three modes in the folded regime, one mode corresponding to ω = 0.085 is in the guided regime ($k_x > \omega/c$), the remaining two modes corresponding to ω = 0.12 and 0.145 are within the light zone ($k_x < \omega/c$), which exhibit far-field peaks in the FFT spectrum at these two frequencies corresponding to the far-field radiation from structure-II. The FFT spectrum (figure 5.4.4) shows, the amplitude peaks of the electric fields (E_x) inside the slit and at far from and transverse to this structure. The amplitude peaks in FFT spectrum of the E_x-field inside the slit indicate the excitation of guided modes and the amplitude peaks in FFT spectrum of the E_x-field at far from and transverse to this structure designate the out-coupling from structure. The phenomenon of the coupling out of radiation can also be appreciated from the E_x-field pattern of structure-B, typically illustrated at ω = 0.12, as shown in figure 5.4.5.

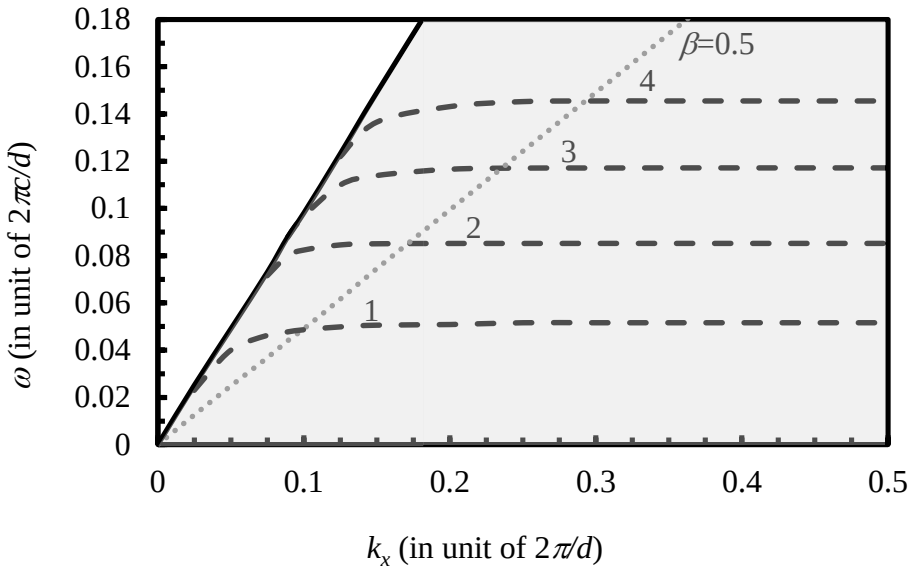

Figure 5.4.2: Guided-mode dispersion characteristics of structure-A, along with a typical beam-mode dispersion line ($\beta = 0.5$), the shaded and non-shaded regions indicating the non-radiating and radiating regimes, respectively. The first four lower dispersion intersecting points are represented by 1, 2, 3 and 4, respectively.

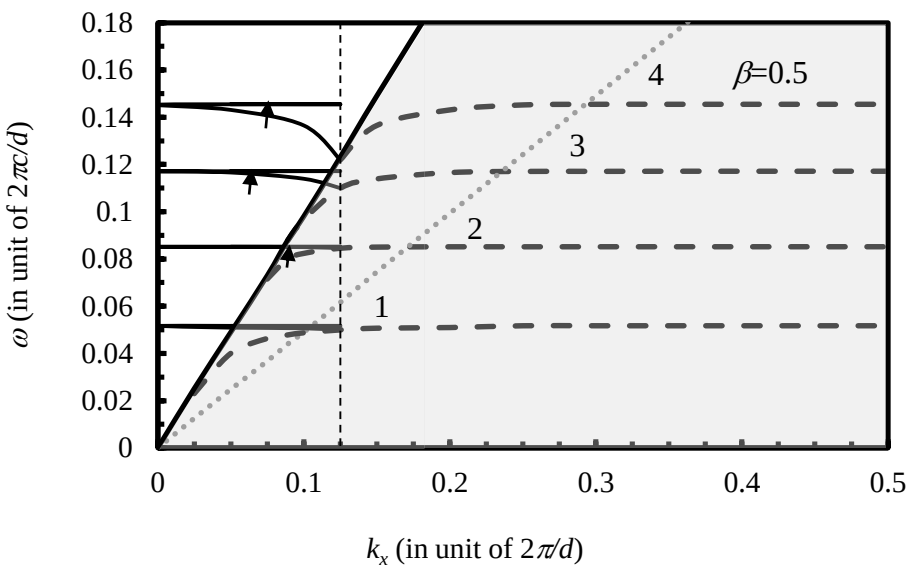

Figure 5.4.3: Guided mode dispersion and folded bands. The folded bands are shown in solid lines, with the vertical dotted line indicating zone-folding symmetry and with the points indicated by the arrows on the folded dispersion curve representing the points at which the momentums corresponding to points 2, 3 and 4, respectively, are shifted due to band folding.

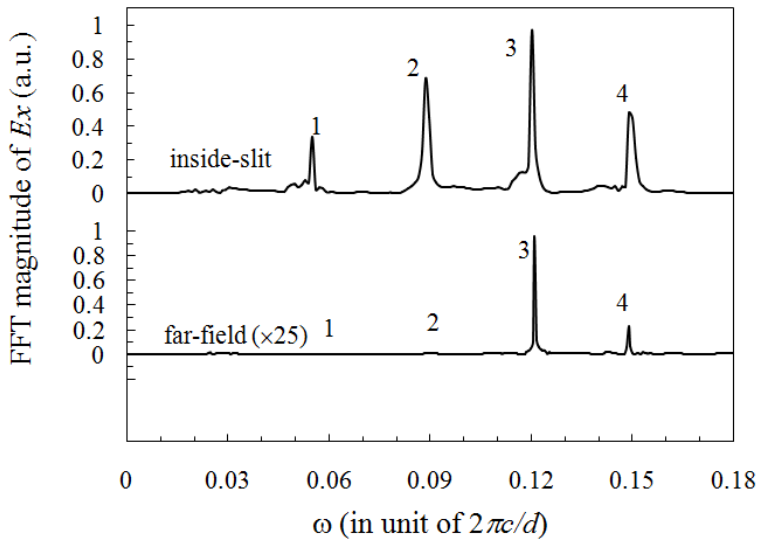

Figure 5.4.4: Inside-slit and far-field (magnified 25 times) FFT spectrum of the E_x of structure-B.

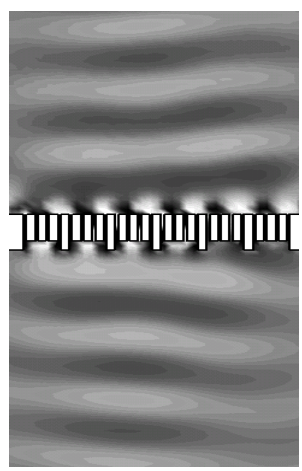

Figure 5.4.5: E_x field pattern at the typical angular frequency ($\omega = 2\pi c/d$) of 0.12 for structure-B showing field radiated from the top and bottom surfaces.

As discuss above, coupling out of Cerenkov-like radiation from the top and bottom surfaces of the structure in the transverse direction is accomplished via Brillouin-zone folding. There are a number of modes with different frequencies are excited in the metamaterial structure due to the finite thickness of the structure. Some modes of metamaterial are folded from non-radiating region to radiation region of dispersion diagram and coupled out from structure in transverse direction when an additional periodicity is added to the structure. Therefore, it is desirable to study the effect of additional period on the coupled out modes. To study this, addition to above structure (figure 5.4.1(b)) two more structures, one with additional period D =3d (figure 5.4.6 (a)) and other with additional period D = 2d (figure 5.4.6(b)) are studied.
In case of structure with additional period D =3d, the band folding occurs at point $k_x = \pi/3d$ i.e. k_x = 0.16 (in unit of $2\pi/d$) on abscissa of the plot shown in figure 5.4.7. It is observed from this figure that three excited modes are folded and out of these three modes one is remain in non-radiating zone of the dispersion diagram. Therefore, only two modes are coupled out from structure and the property of this structure in view of out-coupling is similar to that of structure-B. The FFT spectrum (figure 5.4.4) shows, in general, the amplitude peaks of the electric field (E_x) inside the slit and at far from and transverse to this structure. The amplitude peaks in FFT spectrum of the E_x-field at far from and transverse to this structure designate the out-coupling from structure.

On the other hand, in case of structure with additional period D =2d, the band folding occurs at point $k_x = \pi/2d$ = 0.25 (in unit of $2\pi/d$) on abscissa of the plot shown in figure 5.4.8(a), where only one mode (fourth mode) is folded and three others modes are remain unfolded. However, this folded mode is also remain in the non-radiating region of the dispersion diagram and therefore, no modes will be out-coupled. Figure 5.4.8(b) depicts that the FFT spectrum of the E_x-field inside the slit and at far from and transverse to the structure. There are no discernible peaks in the FFT spectrum of the E_x-field at far from and transverse to the structure indicate that there is no out-coupling from structure.

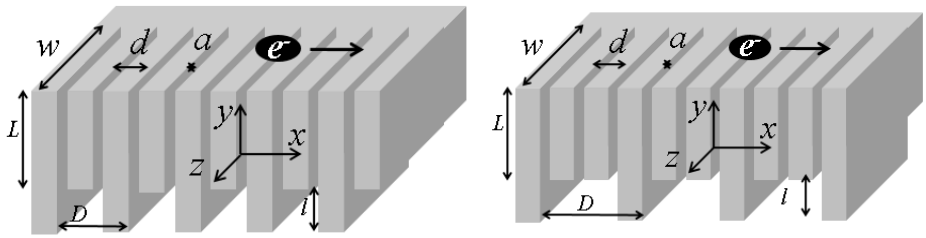

Figure 5.4.6: Metamaterial structure with additional period (a) $D = 3d$ and (b) $D = 2d$.

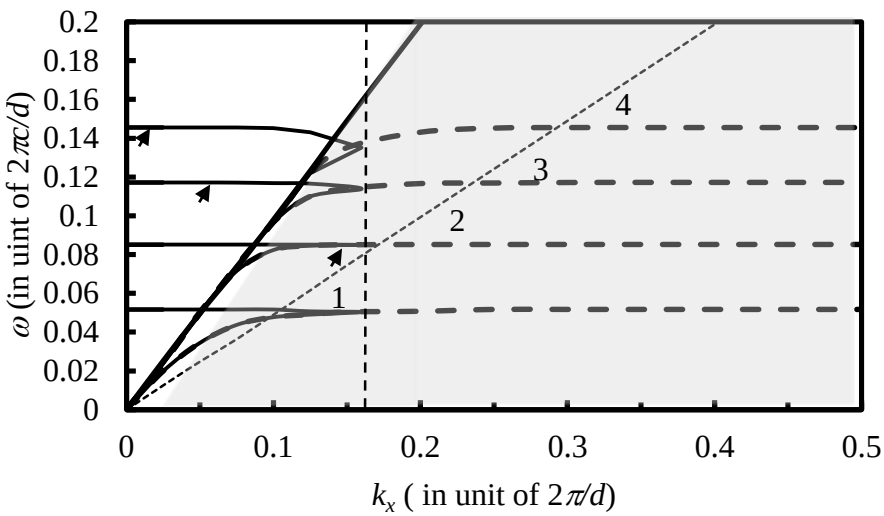

Figure 5.4.7: Guided mode dispersion and folded bands for structure with additional period $D = 3d$. The folded bands are shown in solid lines, with the vertical dotted line indicating zone-folding symmetry and with the points indicated by the arrows on the folded dispersion curve representing the points at which the momentums corresponding to points 2, 3 and 4, respectively, are shifted due to band folding.

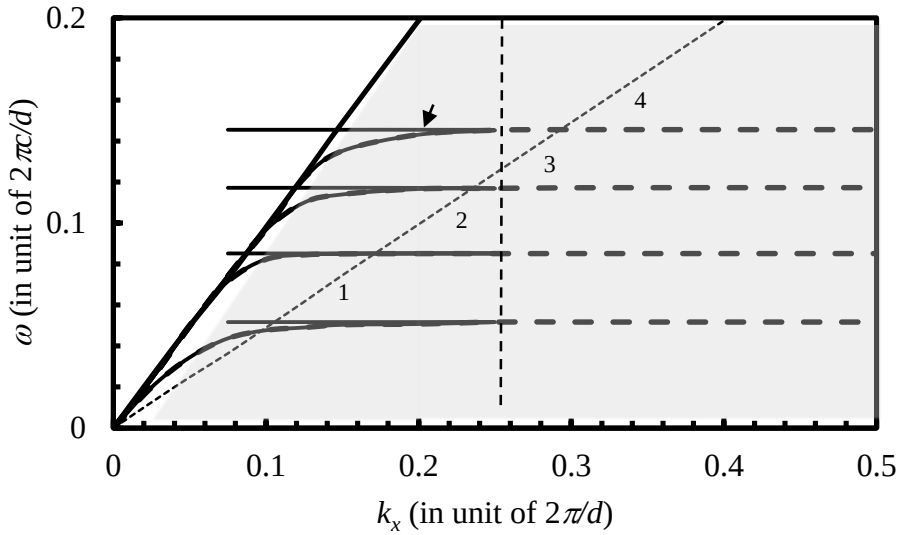

Figure 5.4.8(a): Guided mode dispersion and folded bands for structure with additional period $D = 2d$. The folded bands are shown in solid lines, with the vertical dotted line indicating zone-folding symmetry and with the points indicated by the arrows on the folded dispersion curve representing the point at which the momentums corresponding to point 4, is shifted due to band folding.

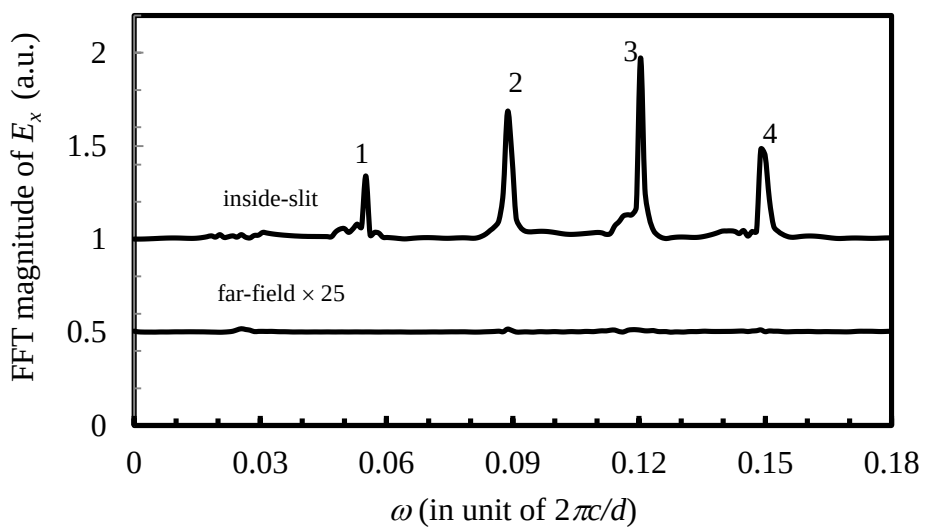

Figure 5.4.8(b): Inside-slit and far-field (magnified 25 times) FFT spectrum of the E_x field of metamaterial structure with additional period $D = 2d$. No discernible peaks in far-field spectrum indicate that there is no out-coupling from structure.

5.5 Metallic Metamaterial as an Interaction Structure of a High-Frequency Electromagnetic Wave Generator

During last two decades attention has been paid for developing intense, tunable sources in the far-infrared, or THz regions, for applications in fields of biology, chemistry, and material science. Linear electron-beam driven vacuum sources such as backward-wave oscillators (BWO), extended interaction oscillators (EIO) and travelling wave tube(TWT), etc. provide a promising way to fulfill the need of THz sources for above applications. However, in such devices, require threshold current density is increased with their operating frequency. In addition to that, as operating frequency increases, the dimension of structure decreases and practical realization of these devices become more difficult due to limitation in fabrication techniques. The performances can be improved by using higher harmonic radiations and or by using simple structure devices consisting of a metal grating and electron beam, which have been widely proposed for very high frequency sources because of their fabrication simplicity. It is well-known that in an open diffraction grating, incoherent spontaneous Smith-Purcell (SP) radiation [127],[132-135] is created as an electron is passing close over the grating. The coherent radiation sources called SP free-electron lasers had been developed based on such phenomenon together with the continuous electron beam [136-137]. However, the radiation intensity from SP radiation based devices is low.

The proposed modified metamaterial structure (structure-B) (figure 5.4.1 (b)) is similar to some extent to the metallic grating and therefore the performance of structure-B in terms of radiation intensity has been compared to that of reflection metal grating. Hence, both the structures in close proximity to a moving electron bunch of typical energy corresponding to normalized axial velocity $\beta(= v/c) = 0.5$ are considered. The radiation intensity, measured in terms of the square of the amplitude of the axial electric field, from structure-B has been compared to that from a reflection metallic grating [138] under identical conditions. Figure 5.5.1(a) depicts the schematic of the reflection metal grating along with the electron bunch. The width (w) of reflection metal grating is identical with the width of structure-B and the axial periodicity (D) is also identical with the additional period (D) of structure-B. The groove depth of reflection metallic grating is optimize to a value of $H = 0.44D$, as indicated in the

figure 5.5.1(b), at an angular frequency $\omega(=2\pi c/d)=0.12$, for the maximum Smith-Purcell radiation intensity in a direction normal to the grating surface. At this frequency, structure-B also shows the far-field peak as shown in figure 5.4.4. Figure 5.5.2 shows the comparison of radiation intensity of structure-B with that of reflection grating. It is clearly seen from figure 5.5.2 that the proposed structure-B is superior to the reflection metallic grating in term of the intensity of the radiation. This enhanced radiation capability of structure-B, in comparison with the reflection grating, can be attributed to the phenomenon of coupling of Cerenkov radiation generated via Brillouin-zone band folding in structure-B, which is absent in the reflection metallic grating where the surface electromagnetic waves supported by a grating are known to be excited by the moving electron bunch, and, which, however, cannot contribute to the far-field radiation [128],[139].

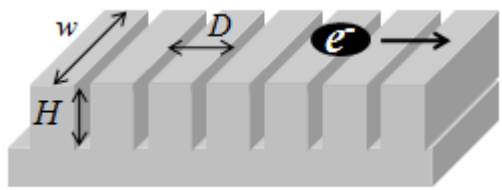

(a)

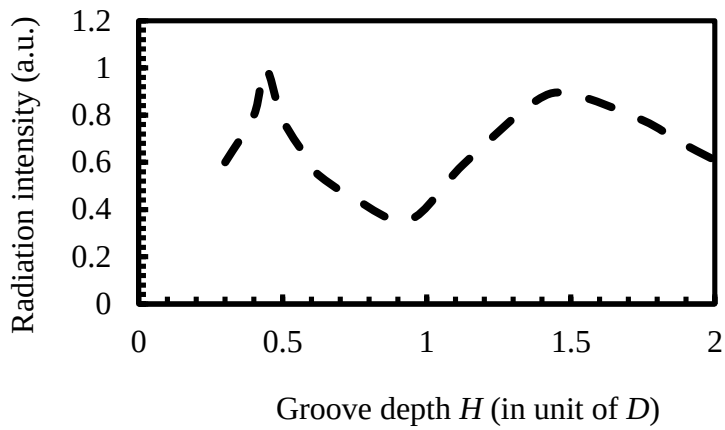

(b)

Figure 5.5.1: (a) Schematic of reflection metal grating along with moving electron bunch and (b) the variation of the radiation intensity of the reflection metal grating with the grating groove depth at an angular frequency $(\omega = 2\pi c/d)$ of 0.12.

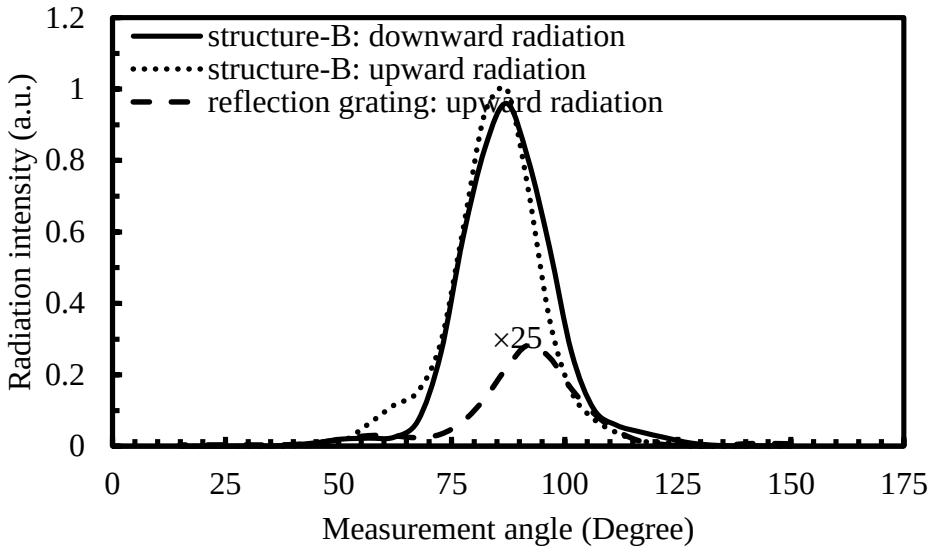

Figure 5.5.2: Angular dependence of the far-field radiation of structure-B compared to that of the reflection grating (magnified 5 times) at an angular frequency ($\omega = 2\pi c/d$) of 0.12, the measurement angle being the angle between the direction of the moving electron bunch and that of the radiation.

CHAPTER 6

Conclusion and Future Work

6.1 Introduction

6.2 Summary of the Thesis

6.3 Scope for Future Work

6.1 Introduction

A positive dielectric response can be achievable from a slab made of a perfect conductor when a one-dimensional array of slits is drilled into the film. It has been shown that in the effective medium limit (wave-length (λ) is much larger than the period of the array (d)), the dielectric response of the system, is dictated by the ratio between period of the array (d) and the width of the slit (a).

The thesis has demonstrated thorough theoretical investigation that such metallic metamaterial supports threshold-free Cerenkov radiation similar to anisotropic dielectric. Moreover, its application for a metallic metamaterial based slab-symmetric wakefield accelerator has also been presented. Finally, an innovative approach to couple out the CR from the metamaterial slab through "Brillouin-zone folding" has been presented.

6.2 Summary of the Thesis

First chapter of the thesis is the introduction briefing the concepts of Cerenkov radiation, their applications and limitations in selecting supporting medium to obtain Cerenkov radiation. At the end of this chapter, the objective of thesis has been described. A brief review of different types (both negative index and positive index) of metamaterial up to optical frequency has presented in Chapter 2. Also in this chapter, selection of metamaterial, namely, metallic metamaterial, for efficient interaction with electron beam and their merits and demerits over other metamaterial have been presented.

The metallic metamaterial structure, reported elsewhere, is a two dimensional structure having infinite extend transverse dimension, which shows positive dielectric response. The refractive index of this structure can be controlled by the structure parameters themselves. However, this kind of structure is very difficult to realize. Therefore, this structure should have a finite dimension in transverse direction. In Chapter 3, it has been shown that the transverse dimension doesn't affect the structure dispersion. In addition, it has also been shown that the introduction of side-wall boundaries in a metallic metamaterial has no effect on frequencies of guided modes, if the width (w) is greater than the twice of the wavelength corresponding to the frequencies of guided modes. These two studies will help one to realize the practical

structure (metallic metamaterial). Moreover, the anisotropic dielectric behavior of this metallic metamaterial has also been confirmed by comparing the reflection spectrum of metallic metamaterial, anisotropic dielectric and isotropic dielectric for two different (TE and TM) polarization of incident electromagnetic waves.

This metallic metamaterial (Chapter 3) has been studied in presence of a convection electron bunch and is presented in Chapter 4. Here, a three-dimensional structure of this metamaterial has been considered. The theoretical studies carried out here, reveal a Cerenkov-like waves which is generated inside the structure when an electron passes near to its surface and the radiation angles ($tan\theta = v_{beam}/c = \beta$) in metallic metamaterial is similar with that for an effective anisotropic medium. In contrast to the isotropic dielectric case, there is no velocity threshold was found in metallic metamaterial. It has also been shown in this chapter that the finite thickness of the metamaterial slab enforces the generated Cerenkov-like radiation to excite resonantly in the structure at frequencies where the guided-mode and the beam-mode phase velocities become synchronous.

Previous studies reveal that the transverse wake potential is diminished in case of dielectric slab-symmetric wakefield accelerator. The transverse wake-potential limits the accelerated electron bunch quality, namely, bunch "brightness" and, therefore, it is desirable to minimize the transverse wake-potential. The performance, in view of longitudinal and transverse wake potential of metamaterial slab-symmetric wakefield accelerator has been presented in Chapter 4. Studies show that the transverse wake potential is even lower than that of an isotropic dielectric slab-symmetric structure. Simultaneously, the longitudinal wake-potential of metamaterial slab-symmetric structure is higher than that of isotropic dielectric slab-symmetric structure. Therefore, it is proposed that the metallic metamaterial slab-symmetric structure would be a better alternative to dielectric slab-symmetric structure due to its higher longitudanal wake-potential and lower transverse wake-potential. In addition, being a metal structure, the metallic metamaterial structure is good for better thermal management and has nearly no static charge accumulation.

Finite thickness of metamaterial slab enforces the generated Cerenkov-like radiation to excite resonantly in the structure at the frequencies where the guided-mode and the beam-mode phase velocities are synchronous (Chapter 4). The edge coupling of radiation, as in an ordinary dielectric, is not applicable to metallic metamaterial due to "almost" zero group

velocity of radiation in axial direction. In addition, the excited guided modes are bounded by vacuum light lines, hence, these modes are not radiated from this metallic metamaterial structure in transverse direction. The out-coupling mechanism, popularly known as Brillouin-Zone Folding (BZF), of generated Cerenkov-like radiation has been discussed in Chapter 5. The BZF for the metallic metamaterial structure is obtained by introducing additional periodicity to the structure. The magnitude of the intensity of the surface-coupled radiation, obtained by this mechanism, enhanced by an order than those obtained from Smith-Purcell radiation. For every frequency source, devices consisting of a metal grating and electron beam have widely been proposed, compared to backward-wave oscillators (BWO), extended interaction oscillators (EIO) and travelling wave tube (TWT), etc., due to their low current density and fabrication simplicity. The modified metamaterial structure is similar to those simple grating structure and also capable of providing higher radiation intensity. Therefore, the proposed metamaterial structure is a suitable choice as an electromagnetic generator at high frequency.

6.3 Scope for Future Work

In this dissertation, detail analysis for dispersion relation under cold condition has been presented, that is, analysis has been carried out in absence of electron beam. The analysis can further be extended rigorously for hot condition, that is, in presence of electron beam. The analysis, in presence of electron beam is quite tedious and rigorous and also has more practical relevance, namely, in traveling-wave tubes, prediction of electromagnetic signal gain and loss in metamaterial structure under study, etc.

Moreover, in this analysis a perfect electric conductor has been considered as the material of the metamaterial. Hence, one may further extend this work to study the effect of electron beam interaction on the effective structure parameters, such as, electrical permittivity, refractive index, etc. when real metal is considered as material for the metamaterial structure. The theoretical results presented in this thesis are not validated experimentally due to certain limitations. Hence, there remains much scope for validation of these analytical results against experimental results

Bibliography

[1] P. A. Cherenkov, Dokl. Akad.Nauk SSSR 2, 451 (1934).

[2] J. V. Jelley, Cherenkov Radiation and its Applications (Pergamon, NewYork,1958).

[3] G. N. Afanasiev, V. G. Kartavenko, and E. N. Magar, "Vavilov–Cherenkov radiation in dispersive medium", *Physia* B269, 95(1999).

[4] I. Carusotto, M. Artoni, G. C. LaRoa, and F. Bassani, "Slow Group Velocity and Cherenkov Radiation", *Phys.Rev.Lett*.87,064801(2001).

[5] M. Artoni, I. Carusotto, G. C. LaRoa, and F. Bassani, "Vavilov-Cherenkov effect in a driven resonant medium", *Phys. Rev. E*67, 046609(2003).

[6] Yu. O. Averkov and V. M. Yakovenko, "Cherenkov radiation by an electron bunch that moves in a vacuum above a left-handed material", *Phys. Rev. B*72, 205110(2005).

[7] Zhaoyun Duan, Bae-Ian Wu, Jie Lu, Jin Au Kong, and Min Chen, "Cherenkov radiation in anisotropic double-negative metamaterials", *Opt. Express.*18479 Vol. 16, No. 22 (2008).

[8] J. Lu, T. Grzegorczyk, Y. Zhang, J. Pacheco Jr., B.-I. Wu, J. Kong, and M. Chen, "Čerenkov radiation in materials with negative permittivity and permeability", *Opt. Express* 11, 723-734 (2003).

[9] B.-I. Wu, J. Lu, J. Kong, and M. Chen, "Left-handed metamaterial design for Cerenkov radiation", *J. Appl.Phys.* 102, 114907 (2007).

[10] S. Antipov, L. Spentzouris, W. Gai, M. Conde, F. Franchini, R. Konecny, W. Liu, J. G. Power, Z. Yusof, and C. Jing, "Observation of wakefield generation in left-handed band of metamaterial-loaded waveguide" , *J. Appl. Phys.* 104, 014901 (2008).

[11] Sheng Xi, Hongsheng Chen, Tao Jiang, Lixin Ran, Jiangtao Huangfu, Bae-Ian Wu, Jin Au Kong, and Min Chen, "Experimental Verification of Reversed Cherenkov Radiation in Left-Handed Metamaterial", *Phys. Rev. Lett.*103,194801 (2009).

[12] S.J. Smith and E.M. Purcell, "Visible Light from Localized Surface Charges Moving across a Grating", *Phys. Rev. 92,* 1069 (1953).

[13] F. J. Garcia de Abajo, "Interaction of Radiation and Fast Electrons with Clusters of Dielectrics: A Multiple Scattering Approach", *Phys. Rev. Lett.*82, 2776 (1999).

[14] K. Ohtaka, S. Yamaguti, "Smith-Purcell radiation from a charge running near the surface of a photonic crystal", *Opt. Quantum Electron*.34, 235 (2002).

[15] K. F. Casey, C. Yeh, Z. A. Kaprielian, "Čerenkov Radiation in Inhomogeneous Periodic Media", *Phys. Rev. B*768 (1965).

[16] B. Lastdrager, A. Tip, J. Verhoeven, "Theory of Čerenkov and transition radiation from layered structures", *Phys. Rev. E*61, 5767 (2000)

[17] C. Luo, M. Ibanescu, S. G. Johnson, and J. D. Joannopoulos, "Cerenkov radiation in photonic crystals", *Science* 299, 368-371 (2003).

[18] F. J. Gariade Abajo, N. Zabala, A. Rivaoba, A.G. Pattantyus-Abraham, M. O. Wolf, and P.M. Ehenique, "Cherenkov Effect as a Probe of Photonic Nanostructures", *Phys. Rev. Lett*.91, 143902(2003).

[19] F. J. Gariade Abajo, A. Rivaoba, N. Zabala, and P. M. Ehenique, "Electron energy loss spectroscopy as a probe of two-dimensional photonic crystal", *Phys. Rev.* B 68, 205105(2003).

[20] A. M. Cook, R. Tikhoplav, S.Y. Tochitsky, G. Travish, O. B. Williams, and J. B. Rosenzweig, "Observation of Narrow-Band Terahertz Coherent Cherenkov Radiation from a Cylindrical Dielectric-Lined Waveguide", *Phys. Rev. Lett*. 103, 095003(2009).

[21] V.L. Ginsburg, Dokl. Akad. *Nauk SSSR* 56, 253 (1947).

[22] W. Gai, P. Schoessow, B. Cole, R. Konecny, J. Norem, J. Rosenzweig, and J. Simpson, "Experimental Demonstration of Wake-Field Effects in Dielectric Structures", *Phys. Rev. Lett.* 61, 2756 (1988).

[23] S. V. Shchelkunov, T. C. Marshall, J. L. Hirshfield, M. A. Babzien, and M. A. LaPointe, "Experimental observation of constructive superposition of wakefields generated by electron bunches in a dielectric-lined waveguide", *Phys. Rev. Spl. Topics – Accel. and Beams* 9, 011301 (2006).

[24] J. G. Power, M. E. Conde, W. Gai, R. Konecny, P. Schoessow, and A. D. Kanareykin, "Measurements of the longitudinal wakefields in a multimode, dielectric wakefield accelerator driven by a train of electron bunches", *Phys. Rev. Spl. Topics – Accel. and Beams* 3, 101302 (2000).

[25] A. M. Cook, R. Tikhoplav, S. Y. Tochitsky, G. Travish, O. B. Williams, and J. B. Rosenzweig, "Observation of Narrow-Band Terahertz Coherent Cherenkov Radiation from a Cylindrical Dielectric-Lined Waveguide", *Phys. Rev. Lett*. 103, 095003 (2009).

[26] J. Walsh, B. Johnson, G. Dattoli, and A. Renieri, "Undulator and Čerenkov Free-Electron Lasers: A Preliminary Comparison", *Phys. Rev. Lett*. 53, 779(1984).

[27] S. Antipov et al, “Experimental Observation of Energy Modulation in Electron Beams Passing through Terahertz Dielectric Wakefield Structures”, *Phy. Rev.Lett.*108, 144801 (2012).

[28] G. Andonian, O. Williams, X. Wei, P. Niknejadi, E. Hemsing, J. B. Rosenzweig, P. Muggli, M. Babzien, M. Fedurin, K. Kusche, R. Malone, and V. Yakimenko, “Resonant excitation of coherent Cerenkov radiation in dielectric lined Waveguides”, *Appl. Phys.Lett.*98, 202901 (2011).

[29] Eusebio Garate, Randall Cherry, Amnon Fisher, “Far infrared Cherenkov free electron laser”, *Nucl. Inst. and Methods in Phys. Res. Sec. A: Accel., Spectm., Detectors and Associated Equipment*, 272, 1–2(1988).

[30] B.J. Eastlund, “Theory of coherent cherenkov radiation production by high-intensity electron beams”, *Fusion*11 15, (1971).

[31] Juzo Ohkuma, Shuichi Okuda, and Kunihiko Tsumori, “Measurement of coherent Cherenkov radiation from an intense beam of a picosecond electron bunch”, *Phys. Rev. Lett.*66, 1967 (1991).

[32] R. Tikhoplav, P. Musumecci, J. Rosenzweig, S. Tochitsky, G. Gatti, “Diagnostics of an electron beam using coherent Cerenkov radiation”, *Proceedings of FEL* 2007, Novosibirsk.

[33] Veselago, V. G. (1968). "The electrodynamics of substances with simultaneously negative values of [permittivity] and [permeability]".*Soviet Physics Uspekhi*10 (4), 509–514(1968).

[34] Chen, Hongsheng, Chen, Min, “Flipping Photons Backward: Reversed Cherenkov Radiation”, *Materials Today* volume: 14 Issue: 1-2 (2011).

[35] S. Antipov, L. Spentzouris, W. Gai, M. Conde, F. Franchini, R. Konecny, W. Liu, J. G. Power, Z. Yusof, and C. Jing, “Observation of wakefield generation in left-handed band of metamaterial-loaded waveguide”, *J. Appl. Phys.*104, 014901 (2008).

[36] Wikipedia: http://en.wikipedia.org/wiki/Terahertz_radiation

[37] S. Antipov, C. Jing, M. Fedurin, W. Gai, A. Kanareykin, K. Kusche, P. Schoessow, V. Yakimenko, and A. Zholents, “Experimental Observation of Energy Modulation in Electron Beams Passing through Terahertz Dielectric Wakefield Structures”, *Phys. Rev. Lett*. 108, 144801 (2012).

[38] Antipov S., Jing C., Kanareykin A., Yakimenko V., Fedurin M., Kusche K., Gai, W., “Experimental demonstration of wakefield effects in a THz planar diamond accelerating structure”, *Appl. Phys. Lett*. 100 132910 (2012).

[39] B. Jiang, C. Jing, P. Schoessow, J. Power, and W. Gai, “Formation of a novel shaped bunch to enhance transformer ratio in collinear wakefield accelerators”, *Phys. Rev. ST Accel. Beams* 15, 011301(2012).

[40] T-B. Zhang, J. L. Hirshfield, T. C. Marshall, and B. Hafizi, “Stimulated dielectric wake-field accelerator”, *Phys. Rev. E* 56, 4(1997).

[41] M. C. Thompson, H. Badakov, A. M. Cook, J. B. Rosenzweig, R. Tikhoplav, G. Travish, I. Blumenfeld, M. J. Hogan, R. Ischebeck, N. Kirby, R. Siemann, D. Walz, P. Muggli, A. Scott, and R. B. Yoder "Breakdown Limits on Gigavolt-per-Meter Electron-Beam-Driven Wakefields in Dielectric Structures", *Phys. Rev. Lett.*100, 214801 (2008).

[42] A. Tremaine and J. Rosenzweig, "Electromagnetic wake fields and beam stability in slab-symmetric dielectric structures", *Phys. Rev. E* 56, 6 (1997).

[43] G. Andonian, D. Stratakis, M. Babzien, S. Barber, M. Fedurin, E. Hemsing, K. Kusche, P. Muggli, B. O'Shea, X. Wei, O. Williams, V. Yakimenko, and J. B. Rosenzweig, "Dielectric Wakefield Acceleration of a Relativistic Electron Beam in a Slab-Symmetric Dielectric Lined Waveguide", *Phys. Rev. Lett*. 108, 244801 (2012).

[44] J. Shin, J. T. Shen, P. B. Catrysse, and S. Fan, "Cut-through metal slit array as an anisotropic metamaterial film", *IEEE J. Sel. Top. Quantum Electron.*12, 1116 (2006).

[45] J. Shin, Peter B. Catrysse, and Shanhui Fan, "Three-Dimensional Metamaterials with an Ultrahigh Effective Refractive Index over a Broad Bandwidth", *Phys. Rev. Lett*.102, 093903 (2009).

[46] J. T. Shen, P. B. Catrysse, and S. Fan, "Mechanism for Designing Metallic Metamaterials with a High Index of Refraction", *Phys. Rev. Lett*.94, 197401 (2005).

[47] Henry O .Everitt, "Applications of photonic band gap structures", *Optics and photonic news*, Nov. (1992).

[48] T. F. Krauss, R. M. De LaRue, S. Brand, "Two-dimensional photonic-band gap structures operating at near-infrared wavelengths", *Nature* 383 (6602): 699–702 (1996).

[49] S. Anantha Ramakrishna, "Physics of negative refractive index materials", *Rep. Prog. Phys* 68 (2005).

[50] J. D. Jackson, Classical Electromagnetics, John Wiley & Sons, New York, 3rd edn, 1999.

[51] Maier Stefan Alexander, Plasmonics: Fundamentals and Applications, Springer, 2007.

[52] J. B. Pendry, A. J. Holden, W. J. Stewart, and I. Youngs, "Extremely low frequency plasmons in metallic mesostructures", *Phys. Rev. Lett*. 76, 4773 (1996).

[53] J. B. Pendry, A. J. Holden, D. J. Robbins, and W. J. Stewart, "Magnetism from conductors and enhanced nonlinear phenomena", *IEEE Trans. On Microwave Therory and Techniques*, Vol. 47, No. 11, Nov. 1999.

[54] D. R. Smith, W. J. Padilla, D. C. Vier, S. C. Nemat-Nasser and S. Schultz, "Composite Medium with Simultaneously Negative Permeability and Permittivity", *Phys. Rev. Lett*. 84, 4184–4187(2000).

[55] R. A. Shelby, D. R. Smith and S. Schultz, "Experimental Verification of a Negative Index of Refraction" *Science*, 292, 77–79(2001).

[56] T. J. Yen, W. J. Padilla, N. Fang, D. C. Vier, D. R. Smith, J. B. Pendry, D. N. Basov and X. Zhang, "Terahertz Magnetic Response from Artificial Materials", *Science*, 2004, 303,1494–1496.

[57] S. Linden, C. Enkrich, M. Wegener, J. Zhou, T. Koschny and C. M. Soukoulis, "Magnetic Response of Metamaterials at 100 Terahertz" *Science*, 2004, 306, 1351–1353.

[58] C. M. Soukoulis, S. Linden and M. Wegener, "Negative Refractive Index at Optical Wavelengths", *Science*, 2007, 315, 47–49.

[59] J. Zhou, T. Koschny, M. Kafesaki, E. N. Economou, J. P. Pendry and C. M. Soukoulis, "Saturation of the Magnetic Response of Split-Ring Resonators at Optical Frequencies", *Phys. Rev. Lett*., 2005, 95, 223902.

[60] S. Zhang, W. J. Fan, N. C. Panoiu, K. J. Malloy, R. M. Osgood and S. R. J. Brueck, "Experimental Demonstration of Near-Infrared Negative-Index Metamaterials", *Phys. Rev. Lett.*, 2005, 95, 137404.

[61] G. Dolling, C. Enkrich, M. Wegener, C. M. Soukoulis and S. Linden, "Simultaneous Negative Phase and Group Velocity of Light in a Metamaterial", *Science*, 2006, 312, 892–894.

[62] M. C. K. Wiltshire, J. B. Pendry, I. R. Young, D. J. Larkman, D. J. Gilderdale and J. V. Hajnal, "Microstructured Magnetic Materials for RF Flux Guides in Magnetic Resonance Imaging", *Science*, 2001, 291, 849–851.

[63] S. M. Xiao, U. K. Chettiar, A. V. Kildishev, V. P. Drachev and V. M. Shalaev,"Yellow-light negative- index metamaterials", *Opt. Lett.*, 2009, 34, 3478–3480.

[64] Yongmin Liu and Xiang Zhang, "Metamaterials: a new frontier of science and technology", Chem. Soc. Rev., ,40, 2494–2507 (2011)

[65] C. Caloz, A. Sanada and T. Itoh, " A novel mixed conventional microstrip and composite right/left-handed backward directional coupler with broadband and tight coupling characteristic*" IEEE Trans. Microwave Theory Tech*., 2004, 52, 980–992.

[66] A. Kurs, A. Karalis, R. Moffatt, J. D. Joannopoulos, P. Fisher and M. Soljacic, "Wireless Power Transfer via Strongly Coupled Magnetic Resonances" , *Science*, 2007, 317, 83–86.

[67] J. B. Pendry, "Negative Refraction Makes a Perfect Lens", *Phys. Rev. Lett*., 2000, 85, 3966–3969.

[68] X. Zhang and Z. W. Liu, "Superlenses to overcome the diffraction limit" *Nat. Mater*., 2008, 7, 435–441.

[69] A. Grbic and G. V. Eleftheriades, "Overcoming the Diffraction Limit with a Planar Left-Handed Transmission-Line Lens",*Phys. Rev. Lett*., 2004, 92, 117403.

[70] Liu, Z., Lee, H., Xiong, Y., Sun, C. & Zhang, X., "Far-field optical hyperlens magnifying sub-diffraction-limited object", *Science*315,1686 (2007).

[71] A. N. Lagarkov and V. N. Kissel, "Near-Perfect Imaging in a Focusing System Based on a Left-Handed-Material Plate", *Phys. Rev. Lett*., 2004, 92, 077401.

[72] N. Fang, H. Lee, C. Sun and X. Zhang, "Sub–Diffraction-Limited Optical Imaging with a Silver Superlens", *Science*, 2005, 308, 534–537

[73] T. Taubner, D. Korobkin, Y. Urzhumov, G. Shvets and R. Hillenbrand, "Near-Field Microscopy Through a SiCSuperlens" *Science*, 2006, 313, 1595.

[74] Pendry, J. B., Schrurig, D. E. & Smith, D. R., "Controlling electromagnetic fields"' *Science*312,1780–1782 (2006).

[75] D. Schurig, J. J. Mock, B. J. Justice, S. A. Cummer, J. B. Pendry, A. F. Starr, D. R. Smith, "Metamaterial electromagnetic cloak at microwave frequencies" *Science* 314,977–980 (2006).

[76] Cai, W. S., Chettiar, U. K., Kildishev, A. V. &Shalaev, V. M., "Optical cloaking with metamaterials", *Nature Photon*.1,224–227 (2007).

[77] R. Liu, C. Ji, J. J. Mock, J. Y. Chin, T. J. Cui, D. R. Smith, "Broadband ground-plane cloak", *Science*323,366–369 (2009).

[78] Valentine J. Li, J. S. Zentgraf, T. Bartal, G. & Zhang X. "An optical cloak made of dielectrics", *Nature Mater*.8, 568–571 (2009).

[79] H. T. Chen, W. J. Padilla, J. M. O. Zide, A. C. Gossard, A. J. Taylor and R. D. Averitt, "Active terahertz metamaterial devices", *Nature*, 2006, 444, 597–600.

[80] A. Degiron, J. J. Mock and D. R. Smith, "Modulating and tuning the response of metamaterials at the unit cell level", *Opt. Express*, 2007, 15, 1115–1127.

[81] H. T. Chen, J. F. O'Hara, A. K. Azad, A. J. Taylor, R. D. Averitt, D. B. Shrekenhamer and W. J. Padilla, "Experimental demonstration of frequency-agile terahertz metamaterials", *Nat. Photonics*, 2008, 2, 295–298.

[82] D. J. Cho, W. Wu, E. Ponizovskaya, P. Chaturvedi, A. M. Bratkovsky, S. Y. Wang, X. Zhang, F. Wang and Y. R. Shen, "Ultrafast modulation of optical metamaterials" *Opt. Express*, 2009, 17, 17652–17657.

[83] Muhan Choi , Seung Hoon Lee, Yushin Kim, Seung Beom Kang, Jonghwa Shin, Min Hwan Kwak, Kwang-Young Kang, Yong-Hee Lee Namkyoo Park & Bumki Min, "A terahertz metamaterial with unnaturally high refractive index", *Nature*, 470, 369-374 (2011).

[84] Sheng Xi, Hongsheng Chen, Tao Jiang, Lixin Ran, Jiangtao Huangfu, Bae-Ian Wu, Jin Au Kong, and Min Chen, "Experimental Verification of Reversed Cherenkov Radiation in Left-Handed Metamaterial", *Phys. Rev. Lett.*103,194801 (2009).

[85] D. F. Sievenpiper, E. Yablonovitch, J. N. Winn, S. Fan, P. R. Villeneuve, and J. D. Joannopoulos, "3D Metallo-Dielectric Photonic Crystals with Strong Capacitive Coupling between Metallic Islands", *Phys. Rev. Lett*. 80, 2829 (1998).

[86] D. Sievenpiper, L. Zhang, R. F. J. Broas, N. G. Alexo´polous, and E. Yablonovitch, "High-Impedance Electromagnetic Surfaces with a Forbidden Frequency Band", *IEEE Trans. Microwave Theory Tech*.47, 2059 (1999).

[87] B. A. Munk, Frequency Selective Surfaces: Theory and Design (John Wiley & Sons, New York, 2000).

[88] S. O'Brien and J. B. Pendry, "Magnetic activity at infrared frequencies in structured metallic photonic crystals", *J. Phys. Condens.Matter*14, 6383 (2002).

[89] F. J. Rachford, D. L. Smith, P. F. Loschialpo, and D. W. Forester, "Calculations and measurements of wire and/or split-ring negative index media", *Phys. Rev. E*66, 036613 (2002)

[90] A. D. Boardman, Electrogmagnetic Surface Modes (John Wiley, New York, 1982).

[91] J. B. Pendry, L. Martı´n-Moreno, and F. J. Garcia-Vidal, "Mimicking surface plasmons with structured surfaces", *Science*305, 847 (2004).

[92] M. S. Kushwaha, "Plasmons and magnetoplasmons in semiconductor heterostructures", *Surf. Sci. Rep*.41, 1 (2001).

[93] D. Felbacq and G. Bouchitte, "Waves Random Media" 7, 245 (1997).

[94] J. B. Pendry, A. J. Holden, D. J. Robbins, and W. J. Stewart, "Low frequency plasmons in thin-wire structures", *J. Phys. Condens. Matter*10, 4785 (1998).

[95] P. A. Belov, C. R. Simovski, and S. A. Tretyakov, "Two-dimensional electromagnetic crystals formed by reactively loaded wires", *Phys. Rev. E*66, 036610 (2002).

[96] R. Marque´s, J. Martel, F. Mesa, and F. Medina, "Left-Handed-Media Simulation and Transmission of EM Waves in Subwavelength Split-Ring-Resonator-Loaded Metallic Waveguides", *Phys. Rev. Lett.89*, 183901 (2002).

[97] B. T. Schwarts and R. Piestun, "Total external reflection from metamaterials with ultralow refractive index", *J. Opt. Soc. Am. B*20, 2448 (2003).

[98] P. B. Catrysse, G. Veronis, H. Shin, J. T. Shen, and S. Fan, **"**Guided modes supported by plasmonic films with a periodic arrangement of subwavelength slits", *Appl. Phys. Lett.*88, 031101 (2006).

[99] V. P. Shestopalov et al., Diffraction Gratings (Naukova Dumka, Kiev, 1986).

[100] J. A. Porto, F. J. Garcı´a-Vidal, and J. B. Pendry, "Transmission Resonances on Metallic Gratings with Very Narrow Slits", *Phys. Rev. Lett*.83, 2845 (1999).

[101] P. Lalanne, J. P. Hugonin, S. Astilean, M. Palamaru, and K. D. Mo¨ller, "One-mode model and Airy-like formulae for one-dimensional metallic gratings",*J. Opt. A. Pure Appl. Opt.* 2,48 (2000).

[102] J. T. Shen and P. M. Platzman, "Properties of a one-dimensional metallophotonic crystal", *Phys. Rev. B* 70, 035101(2004).

[103] Amnon Yariv, Pochi Yeh, Optical Waves in Crystal: Propagation and Control Laser Radiation, Wiley-interscience, 2002.

[104] B.N. Basu, Electromagnetic theory and applications in beam-wave electronics (World scientific, Singapore, 1995).

[105] Paul Joseph Grogan, Development of graphical solution methods and their application to problems in heat power engineering (University of Wisconsin--Madison, 1949).

[106] CST Studio Suite, 2008, http://www.cst.com

[107] Brian R. Hunt, Ronald L. Lipsman, Jonathan M. Rosenberg, Kevin R. Coombes, John E. Osborn, Garrett J. Stuck, A Guide to MATLAB: For Beginners and Experienced Users, Cambridge University Press, Second edition.

[108] Karl F. Renk, Basics of Laser Physics: For Students of Science and Engineering, (Springer).

[109] G. T. di Francia, *Nuovo Cim*.16, 61 (1960).

[110] E. E. Fisch and J. E. Walsh, "Operation of the sapphire Cerenkov laser" *Appl. Phys. Lett*.60, 1298 (1992).

[111] I. J. Owens and J. H. Brownell, "Compact superradiant Cerenkov source", *J. Appl. Phys*. 97, 104915 (2005).

[112] Ekaterina S. Belonogaya, Sergey N. Galyamin, and Andrey V. Tyukhtin, "Properties of Vavilov–Cherenkov radiation in an anisotropic medium with a resonant dispersion of permittivity", *JOSA B*, Vol. 28, Issue 12, (2011).

[113] Rosenzweig,J.B.,http://www.iaea.org/inis/collection/NCLCollectionStore/_Public/28/053/28053428.pdf

[114] Don S. Lemons and Lester Thode, "Linear and Nonlinear Theory of Cherenkov Maser Operation in the Intense Relativistic Beam Regime", *Phys. Rev. Lett*.56, 2684 (1986).

[115] T. D. Pointon and J. S. De Groot, "Particle simulations of plasma and dielectric Čerenkov masers", *Phys. Fluids* 31, 908 (1988).

[116] A. N. Didenko, A. R. Borisov, G. P. Fomenko, Yu G. Shtein, Pis'maZh. Tekh. Fiz.9, 60 (1983) [*Sov. Tech. Phys. Lett*. 9, 26 (1983)].

[117] S.Y. Park and J. L. Hirshfield, "Bunch stability during high-gradient wakefield generation in a dielectric-lined waveguide", *Phys. Plasmas* 8, 2461 (2001).

[118] T. B. Zhang, J. L. Hirshfield, T. C. Marshall, and B. Hafizi, "Stimulated dielectric wake-field accelerator", *Phys. Rev. E*56, 4647 (1997).

[119] M. Kando et al., "On the production of flat electron bunches for laser wake field accelerator", *J. Exp. Theor. Phys*.105, 916 (2007).

[120] P.B. Wilson. Introduction to wakefields and wake potentials. U.S. Particle Accelerator School, Batavia, Illinois, July-August 1987.

[121] B.W. Zotter and S. Kheifets. Impedances and Wakes in High Energy Particle Accelerators. World Scientific, London, 1998.

[122] C. W. Neff, T. Yamashita, and C. J. Summers, "Observation of Brillouin-zone folding in photonic crystal slab waveguides possessing a superlattice pattern", *Appl. Phys. Lett*.**90**, 021102 1-3 (2007).

[123] C. W. Neff, T. Yamashita, and C. J. Summers, "A photonic crystal superlattice based on triangular lattice", *Opt. Express*13, 3166-3173 (2005).

[124] Chihiro Hamaguchi, Basic Semiconductor Physics, Second edition, Springer.

[125] T. B. Boykin, and G. Klimeck, "Practical application of zone-folding concepts in tight-binding calculations", *Phys. Rev. B* 71, 115215 1-6 (2005).

[126] S. Nakashima, and H. Harima, "Raman Investigation of SiC Polytypes", *Phys. Stat. Sol*.162, 39-64(1997).

[127] S. J. Smith, and E.M. Purcell, "Visible Light from Localized Surface Charges Moving across a Grating", *Phys. Rev.* 92, 1069 (1953).

[128] O.A. Tret'yakov, "Theory of Smith-Purcell effect", *Soviet Radio Physics*, 2, 219-223 (1966).

[129] Léon Brillouin Les électronsdans les métauxet leclassement des ondes de de Broglie correspondantes Comptes Rendus Hebdomadaires des Séances de l'Académie des Sciences, 191, 292 (1930). (original article).

[130] C. Kittel**,** Introduction to Solid State Physics**,** John Wiley, New York, 1996.

[131] T. B. Boykin, and G. Klimeck, "Practical application of zone-folding concepts in tight-binding calculations", *Phys. Rev. B*71, 115215 1-6 (2005).

[132] J. T. Donohue, "Simulation of Smith-Purcell radiation using a particle-in-cell code", *Phys. Rev. ST Accel. Beams* 8, 060702 (2005).

[133] J. T. Donohue and J. Gardelle, "Simulation of a Smith-Purcell free-electron laser with sidewalls: Copious emission at the fundamental frequency", *Appl. Phys. Lett*. 99(16), 161112 (2011).

[134] S. Taga, K. Inafune, and E. Sano, "Analysis of Smith-Purcell radiation in optical region", *Opt. Express* 15(24), 16222–16229 (2007).

[135] J. Xu and X. D. Zhang, "Negative electron energy loss and second-harmonic emission of nonlinear nanoparticles", *Opt. Express* 19(23), 22999–23007 (2011).

[136] D. Li, Z. Yang, K. Imasaki, and G. S. Park, “Particle-in-cell simulation of coherent and superradiant Smith-Purcell radiation”, *Phys.Rev.ST Accel. Beams* 9(4), 040701 (2006).

[137] D. Li, K. Imasaki, Z. Yang, and G. S. Park, “Three-dimensional simulation of super-radiation Smith-Purcell radiation”, *Appl. Phys. Lett*. 88(20), 201501 (2006).

[138] C. Palmer, Diffraction Grating Handbook, 6th edition (Newport Corporation), Chap. 12.

[139] H. L. Andrews, C. H. Boulware, C. A. Brau, and J. D. Jarvis, “Gain of a Smith-Purcell free-electron laser” , *Phys. Rev. ST Accel. Beams* 7, 070701 1-7 (2004).

List of Publication

Journal Publications:

1. **Anirban Bera**, Ranjan Kumar Barik, Matlabjon Sattorov, Ohjoon Kwon, Sun-Hong Min, In-Keun Baek, Seontae Kim, Jin-Kyu So, and Gun-Sik Park, "Surface-coupling of Cerenkov radiation from a modified metallic metamaterial slab via Brillouin-band folding", *Optics Express*, Vol. 22, Issue 3, pp. 3039-3044 (2014)
2. Matlabjon Abdurakhimovich Sattorov, **Anirban Bera**, Ashok Sharma, Won-Jong Kang, Oh-Joon Kwon, Sun-Shin Jung, Dae-Ho Kim, Ki Wook Lee, Jong-Hyo Won, Chan Ho Kook, and Gun-Sik Park, "Thermal Analysis of a Strapped Magnetron", *IEEE Trans. On Electron Devevices*,Vol. 58, No. 8, 2011
3. R.K. Barik, **A. Bera**, A.K. Tanwar, I.K. Baek, S.H. Min, O.J. Kwon, W.S. Lee, G.-S. Park, "A novel approach to synthesis of scandia-doped tungsten nano-particles for high-current-density cathode applications," *International Journal of Refractory Metals and Hard Materials*, vol. 38, pp. 60-66, May 2013.
4. R.K. Barik, **A. Bera**, R.S. Raju, A.K. Tanwar, I.K. Baek, S.H. Min, O.J. Kwon, M.A. Sattorov, K.W. Lee, G.-S. Park, "Development of alloy-film coated dispenser cathode for terahertz vacuum electron devices application," *Applied Surface Science*, vol 276, pp 817-822, July 2013.
5. Ohjoon Kwon, Matlabjon Abdurahimovich Sattorov, Sun-Hong Min, In-Keun Baek, Seontae Kim, **Anirban Bera**, Ranjan Kumar Barik, Ranajoy Bhattacharya, Jin-Young Jeong, Jong-Hyo Won, and Gun-Sik Park, "Efficient terahertz oscillation using a half-period staggered grating resonator", *Japanese Journal of Applied Physics* 53, 066201 (2014)

Conference proceedings:

1. O. Kwon, J.-K. So, A. Srivastava, M. Sattorov, R. K. Barik, **A. Bera**, A. K. Tanwar, S.-H. Park, I.-K. Baik, J.-H. Choi, J. Kim, J.-W. Yang, J.-H. Kim, S.-S. Chang, and G.-S. Park. "Micro-fabricated millimeter wave vacuum electronic devices." *in Proc. 35th Int. Conf. IRMMW-THz, Rome, Italy*, Sep. 5-10, 2010.
2. R. K. Barik, A. K. Tanwar, **A. Bera**, O. Kwon, M. A. Sattorov, G.-S. Park, "High current density nano-particle dispenser cathode for THz vacuum electron devices." *in Proc. 2nd Int. THz-Bio Workshop, SNU, Seoul, Korea*, p. 47 (P-1), Jan. 19-20, 2011.
3. R. K. Barik, A. K. Tanwar, **A. Bera**, Ohjoon Kwon, M. A. Sattorov, G.-S. Park. "Investigation of emission mechanism of scandium doped nano particle dispenser cathode for THz vacuum electron devices." in Proc. 36th *Int. Conf. IRMMW-THz, Houston, TX, USA*, Oct. 2-7, 2011.

4. **A. Bera**, O. Kwon, R. K. Barik, M. A. Sattorov, G.-S. Park, "Thermal issues in THz vacuum electron devices." *in Proc. 2nd Int. THz-Bio Workshop, SNU, Seoul, Korea*, p. 48 (P-2),Jan. 19-20, 2011.

5. M. A. Sattorov, **A. Bera**, R. K. Barik, O. Kwon, G.-S. Park, K. A. Lukin, A. S. Tishchenko, "Thermal velocity effects in sheet-beam for THz devices." *in Proc. 2nd Int. THz-Bio Workshop, SNU, Seoul, Korea*, p. 52 (P-5), Jan. 19-20, 2011.

6. O. Kwon, J.-K. So, M. Sattorov, R. K. Barik, **A. Bera**, A. K. Tanwar, S.-H. Park, I.-K. Baek, J.-H. Kim, S.-S. Chang, G.-S. Park, "CW/pulsed sub-THz wave system for biomedical applications." *in Proc. 2nd Int. THz-Bio Workshop, SNU, Seoul, Korea*, p. 59 (P-9),Jan. 19-20, 2011,

7. G.-S. Park, S. H. Min, M. A. Sattorov, O. J. Kwon, R. K. Barik, **A. Bera**. "High power terahertz activities at SNU." *in Proc. 8th International Workshop: Strong microwave and terahertz waves: sources and applications. Nizhniy Novgorod, Russia*, July 9-16, 2011.

8. **A. Bera**, O. Kwon, R. K. Barik, A. Tanwar, M. A. Sattorov, and G.-S. Park "Design of depressed collector for 95 GHz CCBWO." *in Proc. IEEE IVEC, Bangalore*, India, pp. 135-136, Feb. 21-24, 2011,

9. R. K. Barik, A. K. Tanwar, I. K. Baek, K. Eom, **A. Bera**, M. A. Sattorov, S. H. Min, O. Kwon, and G.-S. Park. "Effect of surface roughness of high current density nano-particle cathode for THz vacuum devices application." *in Proc. IEEE IVEC-IVESC, Monterey, USA*, p. 369, Apr. 24-26, 2012.

10. R. K. Barik, A. K. Tanwar, I. K. Baek. K. Eom, **A. Bera**, M. A. Sattorov, S.-H. Min, O. J. Kwon, G.-S. Park, "Development of high current density scandate cathode for terahertz vacuum devices application." *in Proc. 3rd Int. THz-Bio Workshop, SNU, Seoul, Korea*, p. P-2, Feb. 8-9, 2012.

11. R. K. Barik, A. Tanwar, I. K. Baek, K. Eom, **A. Bera**, M. Sattorov, S.-H. Min, O. Kwon, G.-S. Park. "Study of dispenser cathode development for terahertz vacuum devices application." *in Proc. 37th Int. Conf. IRMMW-THz, Wollongong (UOW), Australia*, Sep. 23-28, 2012.

12. **A. Bera**, M. A. Sattorov, O. J. Kwon, R. K. Barik, S.-H. Min, G.-S. Park, "Smith-Purcell radiation from metallic metamaterial grating." *in Proc. 3rd Int. THz-Bio Workshop, SNU, Seoul, Korea*, p. P-1, Feb. 8-9,2012.

13. M. A. Sattorov, E. Khutoryan, K. Lukin, G.-S. Park, **A. Bera**, R. K. Barik, O.-J. Kwon, S.-H. Min, A. Sharma, A. Tanwar, "Experimental analysis on 0.1 THz clinotron." *in Proc. 3rd Int. THz-Bio Workshop, SNU, Seoul, Korea*, p. P-3, Feb. 8-9,2012.

14. M. A. Sattorov, E. Khutoryan, K. Lukin, G.-S. Park, **A. Bera**, R. K. Barik, O.-J. Kwon, S.-H. Min, A. Sharma, A. Tanwar, "Automodulation processes in BWO with inclined electron beam at low focusing magnetic fields." *in Proc. 3rd Int. THz-Bio Workshop, SNU, Seoul, Korea*, p. P-4, Feb. 8-9,2012.

15. O. Kwon, J.-K. So, M. Sattorov, R. K. Barik, **A. Bera**, A. K. Tanwar, I.-K. Baek, S.-H. Min, J.-H. Kim, S.-S. Chang, G.-S. Park, "Microfabricated sub-terahertz vacuum electronic devices." *in Proc. 3rd Int. THz-Bio Workshop, SNU, Seoul, Korea*, p. P-5, Feb. 8-9, 2012.

16. S.-H. Min, O. Kwon, M. Sattorov, I. K. Baek, K.-H. Eom, H. Son, D-H. Choi, S.-H. Bak, S. Kim, **A. Bera**, R. K. Barik, K.-T. Kim, G.-H. Park, W.-Y. Park, J.-Y. Lee, S.-J. Cho, O. S. Kwon, G.-S. Park, "Biological effects by AC ns pulsed electromagnetic fields (EMF) at cm & mm waves exposures and DC ns pulsed electric fields (nsPEF)." *in Proc. 3rd Int. THz-Bio Workshop, SNU, Seoul, Korea*, p. P-25, Feb. 8-9, 2012,.

17. **A. Bera**, R. K. Barik, S.-H. Min, O. Kwon, I. Baek, S. Kim, M. A. Sattorov, and G.-S. Park. "Enhanced SPR in frequency independent dielectric grating*." in Proc. IEEE IVEC-IVESC, Monterey, USA*, p. 157,Apr. 24-26, 2012,

18. M. Sattorov, E. Khutoryan, K. Lukin, G.-S. Park, **A. Bera**, R. K. Barik, O. Kwon, S.-H. Min, A. Sharma, A. Tanwar. "Experimental study on 0.1 THz Clinotron." *in Proc. IEEE IVEC-IVESC, Monterey, USA*, p. 453,Apr. 24-26, 2012.

19. S.-H. Min, O.-J. Kwon, M. A. Sattorov, J.-K. So, I.-K. Baek, S.-T. Kim, K.-H. Eom, **A. Bera**, R. K. Barik, Y.-M. Shin, W.-S. Lee, J.-H. S and G.-S. Park, "Studies on high power THz radiation using nanosecond pulse in oversized relativistic backward wave oscillator." *in Proc. IEEE IVEC-IVESC, Monterey, USA*, p. 4.19, Apr. 24-26, 2012.

20. **A. Bera**, R. K. Barik, O. Kwon, I. K. Baek, S. Kim, S.-H. Min, M. Sattorov, G.-S. Park. "Generation of THz radiation: Metamaterial grating versus lamellar grating." *in Proc. 37th Int. Conf. IRMMW-THz, Wollongong (UOW), Australia*, Sep. 23-28, 2012.

21. R. K.Barik, **A. Bera**, A.K. Tanwar, I.K. Baek, K. Eom, M.A. Sattorov, S.H. Min, O.J. Kwon, G-S. Park, "Sol-gel Synthesis of Sc2O3 Doped W Nano-particle for Cathode Application," in Proc. IEEE IVEC, Paris, May 21-23, 2013.

22. **A. Bera**, R.K Barik, M.A. Sattorov, O.J. Kwon, S.H. Min, G-S. Park, "Cherenkov-Like Radiation from Metallic Metamaterials," *in Proc. IEEE IVEC, Paris*, May 21-23, 2013.

23. S.H.Min, O.Kwon, M.Sattorov, I.K.Baek, S.T.Kim, **A.Bera**, R.KBarik, W.S.Lee, J.H.So, G.S.Park, "Power Estimation of Electromagnetic Coupling Effectiveness by a X-band Backward Wave Oscillator with Mode Conversion," *in Proc. IEEE IVEC, Paris*, May 21-23, 2013.

24. M. A.Sattorov, A. K.Tanwar, **A.Bera**, R. K.Barik, S. H. Min, O.Kwon, G. S, Park, "Development on W-Band Coupled-Cavity Device," *in Proc. IEEE IVEC, Paris*, May 21-23, 2013

국문 초록

체렌코프(Cerenkov) 방사는 입자검출, 입자 수 측정, 입자가속 그리고 테라헤르츠 주파수 대역까지의 전자기파 생성에 광범위하게 이용된다. 대류전자 빔(움직이는 전자뭉치)으로부터 체렌코프 방사를 얻기 위해 절연물질이 전반적으로 사용된다. 하지만 열적문제, 전자빔 문턱 에너지 및 높은 RF 전기장에 의한 정전파괴로 인해 이러한 목적을 위해 사용될 물질의 선택에 제한이 있다. 주기적으로 슬릿이 뚫려있는 금속메타물질은 절연물질의 특성을 지니고 있기 때문에, 체렌코프 방사를 위한 유망한 대체물질이 될 수 있다.

이러한 특성으로 인해 움직이는 전자뭉치가 금속메타물질 주변을 지나갈 때의 반응을 해석하고자 하였다. 본문에 기재된 이론적 연구는 대류전자뭉치가 메타물질표면 근처에 존재할 때 체렌코프 방사와 유사한 방사가 가능하다는 것을 밝히고 있다. 또한 이 금속메타물질에서의 방사특성을 결정하는 방사각도 및 문턱 전자에너지가 이방성(anisotropic, 異方性) 절연물질에서의 것들과 유사함이 발견되었다. 하지만 메타물질 평판의 유한한 두께로 인해 메타물질 내에서 체렌코프 방사가 평판진행방향의 도파모드(guided-mode)와 전자빔모드의 위상속도가 일치되는 주파수에서 공명적으로 발진된다. 금속메타물질의 경우 평판진행방향으로의 군속도가 “거의” 영(0)에 가깝기 때문에 기존 절연물질에서의 모서리 방사결합(coupling) 방법은 사용될 수 없다.

한편 "금속메타물질 대칭평판 웨이크필드(wakefield) 가속기”에 대한 연구가 이루어져 왔는데, 이 연구에 따르면 기존 절연물질 대칭평판구조에서의 종 방향 웨이크포텐셜(longitudinal wave potential)보다 높은 값이 관측되었다. 그리고 횡 방향 웨이크포텐셜(transverse wave potential)은 기존 절연물질 대칭평판구조 보다 낮다는 것 또한 발견되었다. 게다가 구조 전체가 금속으로 이루어져 있기 때문에, 금속메타물질구조는 기존 절연물질보다 높은 열 방출 능력 및 표면에서의 낮은 정전하 축적과 같은 몇 가지 이점을 지니고 있다. 그러므로 본문에서 제안하는 메타물질 대칭평판 구조는 웨이크필드 가속기 응용으로 기존 절연물질 대칭평판 구조 보다 더 나은 선택이 될 수 있다.

더 나아가, 여기서 제안된 메타물질 평판구조에서의 체렌코프 방사 결합을 위해, 기존 모서리에서의 방사결합과는 달리, “브릴루앙영역 접힘(Brillouin-zone folding) 현상”이라는 혁신적인 방법을 통하여 구조 표면에서의 방사결합이 가능하도록 하였다. 본 연구에서는 메타물질구조에 추가적인 주기를 도입함으로써 구조 내에 존재하는 도파모드의 일부가

접히도록 설계되도록 제안하였다. 본 연구에서 제안된 메커니즘(mechanism)으로 이루어지는 메타물질 표면에서의 방사결합의 세기(intensity)가 기존 Smith-Purcell 방사의 세기보다 한 자릿수 이상 향상됨이 발견 되었다. **핵심단어: 체렌코프 방사, 금속메타물질, 브릴루앙영역 접힘 현상, 웨이크필드 가속기**